APPLICATIONS OF QUANTITATIVE PHASE IMAGING FOR PATHOLOGY

BY

SHAMIRA SRIDHARAN

DISSERTATION

Submitted in partial fulfillment of the requirements
for the degree of Doctor of Philosophy in Bioengineering
in the Graduate College of the
University of Illinois at Urbana-Champaign, 2015

Urbana, Illinois

Doctoral Committee:

Associate Professor Gabriel Popescu, Chair
Professor Andre Kajdacsy-Balla
Professor Rohit Bhargava
Professor Stephen Boppart

Abstract

Prostate cancers, which account for 14% of all cancers diagnosed in the United States, and colorectal cancers, which account for 8.2% of all cancers, present a unique set of diagnostic problems [1]. In the case of prostate cancer, overdiagnosis of early-stage disease and poor accuracy at characterizing high-risk disease, especially when diagnosed at the intermediate stage, are major problems. A new prognostic method is thus necessary for improving prostate cancer management. In the case of colorectal cancer, early disease diagnosis is of critical importance for the purpose of reduction in disease-specific death rates. An automated screening tool which identifies cases that warrant further examination by the pathologist would assist in the implementation of a wide-spread screening program.

Quantitative phase imaging (QPI) of unstained tissue provides information on the refractive index distribution, or tissue morphology, with nanometer level sensitivity. Subtle morphological changes in both the epithelial and stromal regions of tissue, which are not visible in stained tissue sections used in current pathological settings, can be measured using QPI. Thus QPI would be a valuable addition to current diagnostic pathology.

The specific aims of this thesis are:

1. Quantitative Gleason grading of prostate cancer: Gleason grading, which is based on glandular differentiation seen on a prostate biopsy, is a widely accepted prognostic tool in prostate cancer. Due to the qualitative nature of Gleason grading, consensus among general pathologists on Gleason scores 5-7 can range from 44.7%-49.2% [2].

This aim of the project is to use QPI to objectively differentiate between prostate cancers of various Gleason grades, thus assisting pathologists with diagnosis.

2. Predict prostate cancer outcomes after prostatectomy: The risk of biochemical recurrence, which is defined as increasing serum PSA levels, is around 25% in men who undergo radical prostatectomy, whereas the risk of prostate cancer specific mortality in the same group is 7-12% [3-5]. Hence, a method capable of forecasting recurrence is highly desirable.

This aim of the project is to use QPI to measure nanometer-level morphological changes in tissue that can be used to identify individuals at high risk for prostate cancer recurrence and to identify specific patient groups that will benefit from QPI over conventional pathology techniques.

3. Quantitative screening of biopsies for colon cancer diagnosis: Colorectal cancer develops from benign adenomatous polyps that advance to carcinoma through a series of genetic mutations over the course of 5-10 years. A colonoscopy can be used to identify and remove polyps, but examination by a pathologist is required to determine whether the polyp was benign or cancerous and if further treatment is necessary. A quantitative tool that can identify dysplastic or cancerous tissue that warrants further examination by the pathologist will help with the implementation of colonoscopy as a widespread screening tool for early cancer detection.

This aim of the project is to use QPI to flag dysplastic and cancerous regions in colorectal biopsies that warrant further examination by pathologists.

References

1. Howlader N, N.A., Krapcho M, Garshell J, Miller D, Altekruse SF, Kosary CL, Yu M, Ruhl J, Tatalovich Z,Mariotto A, Lewis DR, Chen HS, Feuer EJ, Cronin KA. *SEER Cancer Statistics Review, 1975-2011*. 2014 2012 [cited 2014 September, 10].
2. Allsbrook, W.C., Jr., et al., *Interobserver reproducibility of Gleason grading of prostatic carcinoma: general pathologist.* Hum Pathol, 2001. **32**(1): p. 81-8.
3. Eggener, S.E., et al., *Predicting 15-year prostate cancer specific mortality after radical prostatectomy.* The Journal of urology, 2011. **185**(3): p. 869-75.
4. Stephenson, A.J., et al., *Prostate cancer-specific mortality after radical prostatectomy for patients treated in the prostate-specific antigen era.* Journal of clinical oncology : official journal of the American Society of Clinical Oncology, 2009. **27**(26): p. 4300-5.
5. Hull, G.W., et al., *Cancer control with radical prostatectomy alone in 1,000 consecutive patients.* The Journal of urology, 2002. **167**(2 Pt 1): p. 528-34.

Contents

CHAPTER 01: General Introduction

Pathologists make a diagnosis of cancer on suspicious tissue extracted from patients following routine screening exams or surgery. After fixation and tissue processing, which involves dehydration of tissue followed by embedding in paraffin, thin slices of tissue are sectioned using a microtome. The pathologist then examines the tissue under a microscope in order to make a diagnosis. Optically thin slices of tissue do not significantly scatter or absorb light. Due to the transparent nature of tissue, in clinical pathology, contrast is extrinsically generated by adding dyes to make structures visible. Tissue biopsy sections are traditionally stained with hematoxylin and eosin (H&E). Hematoxylin stains nucleus in a deep blue-purple by a reaction that is not completely understood, whereas eosin non-specifically stains proteins pink and makes the cytoplasm and extra-cellular matrix visible [1]. H&E double stain was first introduced in 1876 by Wissowzky and more than a century later, continues to be the most frequently used staining method in diagnostic pathology [2]. When the pathologist suspects the presence of cancer on the H&E stained biopsy, a consecutive biopsy section is stained with specialized stains, immunohistochemical markers (IHC) and/or molecular markers to make a final diagnosis. IHC and molecular pathology, represent major innovations in the field of diagnostic pathology by labeling specific proteins or using molecular information to aid diagnosis. In molecular pathology, the DNA sequence of the patient is profiled to determine which treatment would yield a better response, whereas in immunohistochemistry, downstream proteins expression is studied using antibodies for the protein.

The origins of immunohistochemistry (IHC) can be traced to 1934, when Marrack conjugated a red stain to benzidine tetraedro for detection of typhus and cholera bacteria [3, 4]. Since the

visualization of red stain was difficult in dilute solutions, Albert Coons developed fluorescin conjugated antibodies to visualize Streptococcus pneumoniae in tissue using ultraviolet light in 1941 [5, 6]. But it wasn't until the early 1960s, after the introduction of enzyme labeled antibodies, almost a century after H&E staining was introduced and 30+ years after IHC was first introduced, that the reports of IHC being used in diagnostic pathology laboratories appeared in literature [7-9]. Immunohistochemistry is often termed the "brown revolution" of pathology, due to the brown color of the peroxidase stain. Antigen preservation has been a problem that has often resulted in variability in IHC diagnosis. Formaldehyde fixation has been reported to damage or mask antigen sites to which IHC antibodies bind [10]. Antigen preservation in frozen tissue is reported to be better than in formalin fixed-paraffin embedded (FFPE) tissue and alcohol fixation represents an intermediate option for antigen preservation [11]. But FFPE tissue is the most commonly used histological method used internationally and there have been proposals by specialists to make IHC on FFPE tissue the diagnostic standard [5, 12]. Other problems in immunohistochemistry include the definition of a positive stain, which is subject to variation based on the tissue compartment where a positive stain was seen (center of the tumor Vs the periphery), pattern of the staining (cellular compartment: cytoplasm Vs the nucleus) and staining intensity that can be considered positive [13]. All of these sources of variation contribute to inter-observer variability in interpretation of IHC results. Many computer-assisted IHC interpretation methods are in development today, in an attempt to make interpretation quantitative and thus standardized [14]. However, these methods are still subject to variations in interpretation stemming from illumination source, sensor of the camera, intensity of the stain and signal multiplexing [14].

The most commonly used molecular pathology technique is the fluorescence in-situ hybridization (FISH) probe, which was first developed in the 1980s to detect amplifications in specific DNA sequences. FISH probes for HER2 have been used to guide treatment for breast cancer, but often IHC is preferred due to greater familiarity with IHC [15]. Some FISH probes are sensitive to some fixatives, chemicals and heat; and the fluorescence signals weaken with time, making re-analysis of the same sample difficult [16]. Molecular pathology is a relatively new field, and now more accessible with availability of various DNA sequencing technologies manufactured by Illumina, Roche and Life Technologies. Identification of genetic mutations can be used to predict risk of disease. Additionally, gene expression signatures through platforms like Oncotype DX can be used to guide treatment decisions. These molecular pathology tests can be expensive, there are limited clinical validation studies and limited guidance is available for clinicians regarding which tumors should be sequenced for which mutations and clinical follow-up implications [17].

A common theme that emerges from studying innovations in pathology is that the developments have focused on extrinsic tissue markers and pace of clinical adoption is slow. The slow pace could be due to the applicability of each immunohistochemistry marker or molecular test for a limited number of diseases, thus generating a large number of tests for specific clinical end-points in each disease. Additionally, some IHC techniques require tissue fixation to be performed in a manner that is different from the standard pathology processing standards thus proving to be cumbersome.

Structural information in tissue holds enormous diagnostic potential, as evidenced by the permanence of non-specific stains, such as H&E in pathology practice. Cells and tissue also have intrinsic contrast in the form of refractive index differences between various structures.

Quantitative phase imaging (QPI) is a microscopy technique that reports on nanoscale changes in tissue architecture, while also providing structural information. It uses intrinsic tissue contrast, thus eliminating the need for specialized stains and is insensitive to changes in illumination and camera. Additionally, the same imaging modality can be used to report on multiple tissue archetypes, thus reducing the learning curve. The quantitative nature of this technology also eliminates inter-observer differences prevalent in some pathology specialties.

In this thesis, I show the utility of QPI for solving problems in prostate and colorectal cancer pathology, which represent 22% of all cancers diagnosed by pathologists today [18]. In Chapter 2, I provide a detailed introduction to the nature of interactions between light and tissue, as well as quantitative phase imaging. I also introduce spatial light interference microscopy (SLIM), the QPI technique central to our approach. In Chapter 3, I introduce the issues concerning prostate cancer prognosis. Specifically, inter-observer differences in Gleason grading, a prognostic tool used to guide treatment decisions, has a huge impact on disease outcomes. I demonstrate a method that combines structural information with light scattering differences in tissue microenvironment to improve Gleason grading accuracy. In Chapter 4, I show how light scattering changes in the stroma, or connective tissue adjoining glands has valuable prognostic potential beyond the ability of Gleason grading. In a nested-case control study, where patients are matched according to Gleason grade and pathological tumor stage, I demonstrate the ability of QPI to predict post-surgical biochemical recurrence with higher accuracy than currently used clinical techniques. In Chapter 5, I validate the recurrence prediction tool on a general population of patients and identify which patient groups would benefit from using QPI for prognosis. In Chapter 6, I demonstrate how QPI can help with the implementation of wide-spread colorectal cancer screening programs. By combining structural information with phase

distribution, quantitative diagnoses can be made on colorectal tissue, such that specific tissue regions requiring pathologists' attention can be highlighted. In Chapter 7, I provide a brief outlook on other pathology problems that can potentially be solved using QPI.

1.1 References

1. Fischer, A.H., et al., *Hematoxylin and eosin staining of tissue and cell sections.* CSH Protoc, 2008. **2008**: p. pdb prot4986.
2. A., W., *Ueber das Eosin als reagenz auf Hämoglobin und die Bildung von Blutgefässen und Blutkörperchen bei Säugetier und Hühnerembryonen.* Archiv für mikroskopische Anatomie, 1876. **13**: p. 479-496.
3. de Matos, L.L., et al., *Immunohistochemistry as an Important Tool in Biomarkers Detection and Clinical Practice.* Biomarker Insights, 2010. **5**: p. 9-20.
4. Marrack, J., *Nature of antibodies.* Nature, 1934. **133**: p. 292-293.
5. Matos, L.L., et al., *Immunohistochemistry as an important tool in biomarkers detection and clinical practice.* Biomark Insights, 2010. **5**: p. 9-20.
6. Coons, A.H., H.J. Creech, and R.N. Jones, *Immunological Properties of an Antibody Containing a Fluorescent Group.* Experimental Biology and Medicine, 1941. **47**(2): p. 200-202.
7. Burnham, T.K., T.R. Neblett, and G. Fine, *The Application of the Fluorescent Antibody Technic to the Investigation of Lupus Erythematosus and Various Dermatoses.* Journal of Investigative Dermatology, 1963. **41**(6): p. 451-456.
8. Haines, D.M. and K.H. West, *Immunohistochemistry: Forging the links between immunology and pathology.* Veterinary Immunology and Immunopathology, 2005. **108**(1-2): p. 151-156.
9. Nakane, P.K. and G.B. Pierce, Jr., *Enzyme-labeled antibodies: preparation and application for the localization of antigens.* J Histochem Cytochem, 1966. **14**(12): p. 929-31.
10. Rickert, R.R. and R.M. Maliniak, *Intralaboratory quality assurance of immunohistochemical procedures. Recommended practices for daily application.* Arch Pathol Lab Med, 1989. **113**(6): p. 673-9.
11. Miettinen, M., *Immunohistochemistry of solid tumors. Brief review of selected problems.* APMIS, 1990. **98**(3): p. 191-9.
12. Wick, M.R., *Immunohistochemical approaches to the diagnosis of undifferentiated malignant tumors.* Ann Diagn Pathol, 2008. **12**(1): p. 72-84.
13. Seidal, T., A.J. Balaton, and H. Battifora, *Interpretation and quantification of immunostains.* Am J Surg Pathol, 2001. **25**(9): p. 1204-7.
14. Taylor, C.R. and R.M. Levenson, *Quantification of immunohistochemistry—issues concerning methods, utility and semiquantitative assessment II.* Histopathology, 2006. **49**(4): p. 411-424.
15. Carlson, B.O.B., *HER2 TESTS: How Do We Choose?* Biotechnology healthcare, 2008. **5**(3): p. 23-27.
16. Brown, L.A. and D. Huntsman, *Fluorescent in situ hybridization on tissue microarrays: challenges and solutions.* J Mol Histol, 2007. **38**(2): p. 151-7.
17. Harris, T.J. and F. McCormick, *The molecular pathology of cancer.* Nat Rev Clin Oncol, 2010. **7**(5): p. 251-65.
18. Howlader N, N.A., Krapcho M, Garshell J, Miller D, Altekruse SF, Kosary CL, Yu M, Ruhl J, Tatalovich Z,Mariotto A, Lewis DR, Chen HS, Feuer EJ, Cronin KA. *SEER Cancer Statistics Review, 1975-2011*. 2014 2012 [cited 2014 September, 10].

CHAPTER 02: Introduction to Quantitative Phase Imaging

2.1 Light-Tissue Interaction

When light is propagated through tissue, there is a change in the irradiance, spectrum, polarization, phase, direction and coherence due to which information about tissue can be obtained [1-3]. The light-tissue interaction can be classified as elastic and inelastic. Elastic light scattering occurs when the direction of propagated light changes but the frequency of is conserved. This is different from dynamic light scattering where Doppler shifts caused by dynamic specimen such as live cells cause small changes in light frequency[4]. In diseases such as cancer, the morphological changes in tissue modify light properties such as scattering parameters and this information can be used to diagnose disease.

Compared to X-rays and γ-rays, the electromagnetic radiation in the optical regime is non-ionizing and, thus, noninvasive. With respect to ultrasound waves, light provides higher resolution and contrast. On the other hand, however, optical waves are strongly scattered in biological tissues, which reduces their penetration depth and makes extracting diagnosis information extremely difficult. This strong light-tissue interaction is due to the morphology of the biological matter that exhibits significant features over length scales on the order of the light wavelength. For example, let us look at highly compartmentalized structures such as cells. The three major structures in cell are cell membrane, nucleus and cytoplasm. The cell membrane encompasses the cytoplasm and is made of a phospholipid bilayer composed of proteins and glycoproteins that float on lipids. The cytoplasm encompasses cytosol in which various organelles such as mitochondria, golgi apparatus, endoplasmic reticulum, peroxisomes, lysosomes are suspended. The cell nucleus is separated from the cytoplasm by the nuclear envelope and is the site of DNA replication and RNA translation[5]. The different cellular

structures have different refractive indices due to varying compositions. These morphological features translate into refractive index inhomogeneity and, consequently, scattering. Thus the cell is a scattering medium with large structures such as nucleus scattering light at smaller angles and smaller organelles such as mitochondria scattering light at large angles [6, 7].

The inhomogeneous wave equation, which describes the optical field propagation in the tissue, is generally difficult to solve, except in the asymptotic regimes of very *strong* or very *weak* scattering. The former regime applies whenever bulk tissues are studied, for example, in *in-vivo* settings. In this case light is multiply scattered and, eventually, the wave-vector distribution becomes isotropic. At that point, the coherence area of the field reaches a minimum of the order of the wavelength squared, meaning that the phase of the field can be physically defined locally, over the scale of the wavelength of light. At larger scales, this scattering regime is commonly described not in terms of the *wave equation*, but a *diffusion equation*, which governs the distribution of light energy density in the tissue and ignores coherent phenomena. The tissue optical parameters that govern the diffusion process are the scattering mean free path, l_s, and the anisotropy factor, g, which scales l_s to higher values to account for forward scattering. A number of methods have been proposed to measure these parameters and correlate them to certain disease states (see, e.g., Chap. 2 in [8]). Generally, changes in scattering parameters can be used to report on certain disease onset and development. Furthermore, understanding this diffusion process can have broader implications in medical diagnosis. For example, spectroscopic approaches, such as fluorescence and Raman scattering, provide chemically specific information, but are affected by the presence of a diffusive background. Thus, *a priori* knowledge of the tissue optical parameters allows extracting quantitative information from spectroscopy as well

[9]. In particular, light scattering spectroscopy, with diffusion background correction, was shown to inform of cellular level modification during cancer progression [10].

Today, extracting tissue scattering parameters remains challenging, especially due to the broad biological variability within the same tissue type, among different tissue types, and across patients (Table 2.1. in Ref. [8] provides a glimpse of this variability). Sometimes, Monte Carlo simulations are used iteratively to fit the measurements, with l_s and g as fitting parameters [11]. An alternative approach has been proposed to deal with tissue turbidity: instead of trying to model it, remove it using phase conjugation approaches[12]. More recently, this type of time-reversal method has been used to focus light deep into the tissue and modulate it ultrasonically[13].

The *weak* scattering regime applies to light propagating in thin, transparent objects and is typically modeled via the Rytov or (first) Born approximation. The Rytov approximation is more appropriate for reconstructing smooth objects, i.e., for low-resolution imaging, and the Born approximation works better for imaging finer structures (see, e.g., p. 485 in Ref. [14]). Although this description is employed mainly in describing interaction of light with single cells, exploiting the pathlength gating in optical coherence tomography[15], Ralston et al. have shown that the interaction of light with bulk tissue can be described by the first-order Born approximation as well [16]. In this case, the phase of the scattered field is measured interferometricaly and the tissue structure is reconstructed by solving the inverse problem.

Recently, quantitative phase imaging (QPI), in which optical pathlength shifts induced by cells and tissue are measured quantitatively, has been the subject of intense research efforts [17]. This new dimension in imaging has demonstrated valuable potential for studying cell structure and

dynamics [18]. Interestingly, it has been shown that, under the Born approximation, QPI is equivalent to an ultrasensitive angular scattering measurement [19-22]. Furthermore, measuring the quantitative phase map associated with a thin slice of tissue provides information about the l_s and g parameters of the bulk [20, 22]. In this thesis, I demonstrate that optical path-length maps of thin, unlabeled tissue hold cancer diagnosis and prognosis value.

2.2 Quantitative Phase Imaging (QPI)

Spatially-resolved investigation of biological structures has been made possible by QPI techniques. Digitally recorded interference microscopy with automatic phase-shifting (DRIMAPS) is a quantitative phase imaging technique that has been used for measuring cell growth, dry mass, cell spreading and cell motility [23-25] [26, 27]. Using the transport of intensity (TIE) equation, full-field quantitative phase microscopy methods have been developed [28, 29]. TIE-based methods do not require the two beams used in interferometry experiments and therefore have high stability with respect to phase noise. But these methods are computationally intensive as it involves imaging samples through various focal planes, followed by numerical computation of phase using partial differential equations.

Gabor developed digital holography which combines traditional holography with digital recording [30] [31]. Numerically solving the Fresnel propagation equation, the field distribution at different optical planes can be calculated. This makes reconstruction of in-focus field possible for optically thin objects, and the phase map of the sample can be constructed. Digital holography has been adapted for phase shifting interferometry and quantitative phase imaging [32] [33-35].

Full-field QPI techniques using lasers as illumination source, such as Fourier phase microscopy, diffraction phase microscopy and Hilbert phase microscopy were developed and provide phase stability over broad temporal scales [36-40]. White light based QPI methods such as wDPM and SLIM developed in our lab eliminate the speckles from laser illumination, and therefore increases phase sensitivity [41-43]. SLIM is described in more detail below.

2.3 Spatial Light Interference Microscopy (SLIM)

Zernike developed phase contrast microscopy in the 1930s, which is a *qualitative* method of imaging transparent objects, also termed as phase objects [44-46]. Holography, developed by Gabor, enabled recording both amplitude and phase information of such objects [31]. Spatial Light Interference Microscopy (SLIM), combines both of these principles, and is a white-light quantitative phase imaging method that uses the spatially coherent field from a phase contrast microscope [41, 47-49].

SLIM is developed as an add-on module to an existing phase contrast microscope, as shown in Fig. 2.1. The image field outputted by the microscope is Fourier transformed by the lens system L1, L2, L3 onto the surface of a spatial light modulator (SLM). The SLM shifts the phase of the unscattered light with respect to the scattered light, sequentially, in increments of $\pi/2$ (see Ref. [50]). Lens L4 recreates the image of the sample at the CCD, which records an image for each phase modulation. The four *intensity* images are combined to uniquely render the quantitative *phase* map of the image field, as shown in Fig. 2.1 (inset). The transverse resolution of SLIM images is limited only by the numerical aperture of the objective and the spatial path length sensitivity is 0.3nm.

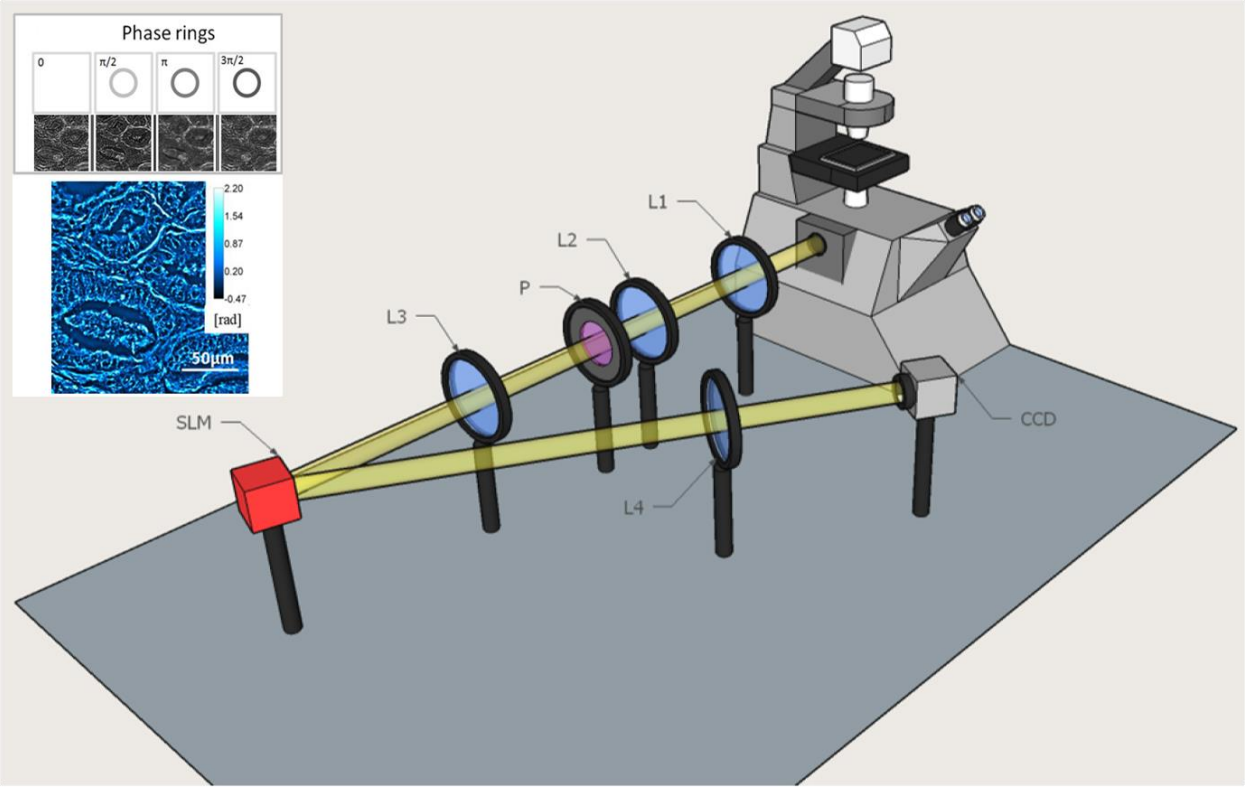

Figure 2.1: The imaging system. The SLIM set-up is an add-on module to a commercial phase contrast microscope. The first set of lenses (L1 and L2) magnify the image to maintain the resolution of the microscope. The Fourier transform of the image plane is projected by lens L3 onto the spatial light modulator (SLM) where the phase pattern is shifted in phase 4 times, in increments of $\pi/2$. The lens L4 Fourier transforms the pattern on the SLM and the final image is recorded onto the CCD and stored on the computer. **(Inset)** Four phase shifted images of prostate tissue recorded using a 40X/0.75NA objective with the final quantitative phase image shown on the right. Color bars indicate phase values in radians.

Since the development of the original SLIM system (SLIM 1.0) in the QLI laboratory, a commercial version known as the CellVista Q100 system was developed. While the original SLIM system was used in the development of the Gleason grading scheme, the nested-case control study for development of a cancer predictor and colon cancer screening tool, the commercial system in combination with lab-developed software was used for validation of the recurrence predictor and colon cancer screening on large tissue regions. Details regarding sample acquisition and specific imaging modalities are included in the Materials and Methods section of each chapter.

2.4 References

1. Bohren, C.F. and D.R. Huffman, *Absorption and scattering of light by small particles*. 1983, New York: Wiley. xiv, 530 p.
2. Hulst, H.C.v.d., *Light scattering by small particles*. 1981, New York: Dover Publications. 470 p.
3. Ishimaru, A., *Electromagnetic wave propagation, radiation, and scattering*. 1991, Englewood Cliffs, N.J.: Prentice Hall. xviii, 637 p.
4. Berne, B.J. and R. Pecora, *Dynamic light scattering with applications to chemistry, biology and Physics*. 1976, New York: Wiley.
5. Alberts, B., *Essential cell biology : an introduction to the molecular biology of the cell*. 2 ed. 2004, New York: Garland Pub. 1 v. (various pagings).
6. Dunn, A. and R. Richards-Kortum, *Three-dimensional computation of light scattering from cells.* Ieee Journal of Selected Topics in Quantum Electronics, 1996. **2**(4): p. 898-905.
7. Mourant, J.R., et al., *Mechanisms of light scattering from biological cells relevant to noninvasive optical-tissue diagnostics.* Applied Optics, 1998. **37**(16): p. 3586-3593.
8. Tuchin, V.V. and Society of Photo-optical Instrumentation Engineers., *Tissue optics : light scattering methods and instruments for medical diagnosis*. 2nd ed. 2007, Bellingham, Wash.: SPIE/International Society for Optical Engineering. xl, 840 p.
9. RichardsKortum, R. and E. SevickMuraca, *Quantitative optical spectroscopy for tissue diagnosis.* Annual Review of Physical Chemistry, 1996. **47**: p. 555-606.
10. Gurjar, R.S., et al., *Imaging human epithelial properties with polarized light-scattering spectroscopy.* Nat Med, 2001. **7**(11): p. 1245-8.
11. Wang, L.H., S.L. Jacques, and L.Q. Zheng, *Mcml - Monte-Carlo Modeling of Light Transport in Multilayered Tissues.* Computer Methods and Programs in Biomedicine, 1995. **47**(2): p. 131-146.
12. Yaqoob, Z., et al., *Optical phase conjugation for turbidity suppression in biological samples.* Nature Photonics, 2008. **2**(2): p. 110-115.
13. Xu, X.A., H.L. Liu, and L.V. Wang, *Time-reversed ultrasonically encoded optical focusing into scattering media.* Nature Photonics, 2011. **5**(3): p. 154-157.
14. Chew, W.C., *Waves and fields in inhomogeneous media*. IEEE Press series on electromagnetic waves. 1995, New York: IEEE Press. xx, 608 p.
15. Huang, D., et al., *Optical Coherence Tomography.* Science, 1991. **254**(5035): p. 1178-1181.
16. Ralston, T.S., et al., *Interferometric synthetic aperture microscopy.* Nature Physics, 2007. **3**(2): p. 129-134.
17. Popescu, G., *Quantitative phase imaging of cells and tissues*. McGraw-Hill biophotonics. 2011, New York: McGraw-Hill. 385.
18. Mir, M., et al., *Chapter 3 - Quantitative Phase Imaging*, in *Progress in Optics*, W. Emil, Editor. 2012, Elsevier. p. 133-217.
19. Ding, H.F., et al., *Fourier Transform Light Scattering of Inhomogeneous and Dynamic Structures.* Physical Review Letters, 2008. **101**(23): p. 238102.
20. Wang, Z., H. Ding, and G. Popescu, *Scattering-phase theorem.* Optics Letters, 2011. **36**: p. 1215.
21. Lim, J., et al., *Born approximation model for light scattering by red blood cells.* Biomedical Optics Express, 2011. **2**(10): p. 2784-2791.

22. Ding, H., et al., *Measuring the scattering parameters of tissues from quantitative phase imaging of thin slices.* Optics Letters, 2011. **36**: p. 2281.
23. Dunn, G.A., D. Zicha, and P.E. Fraylich, *Rapid, microtubule-dependent fluctuations of the cell margin.* J. Cell Sci., 1997. **110**: p. 3091-3098.
24. Zicha, D. and G.A. Dunn, *An Image-Processing System For Cell Behavior Studies In Subconfluent Cultures.* J. Microscopy, 1995. **179**: p. 11-21.
25. Dunn, G.A. and D. Zicha, *Using DRIMAPS system of transmission interference microscopy to study cell behavior*, in *Cell biology: a laboratory handbook* J.E. Celis, Editor. 1998, Academic press: San Diego.
26. Zicha, D., et al., *TGF beta 1 induces a cell-cycle-dependent increase in motility of epithelial cells.* J. Cell Sci., 1999. **112**(4): p. 447-454.
27. Dunn, G.A. and D. Zicha, *Dynamics Of Fibroblast Spreading.* J. Cell Sci., 1995. **108**: p. 1239-1249.
28. Gureyev, T.E., A. Roberts, and K.A. Nugent, *Phase Retrieval With The Transport-Of-Intensity Equation - Matrix Solution With Use Of Zernike Polynomials.* J. Opt. Soc. Am. A-Opt. Image Sci. Vis., 1995. **12**(9): p. 1932-1941.
29. Gureyev, T.E., A. Roberts, and K.A. Nugent, *Partially Coherent Fields, The Transport-Of-Intensity Equation, And Phase Uniqueness.* J. Opt. Soc. Am. A-Opt. Image Sci. Vis., 1995. **12**(9): p. 1942-1946.
30. Goodman, J.W. and R.W. Lawrence, *Digital image formation from electronically detected holograms.* Appl. Phys. Lett., 1967. **11**: p. 77.
31. Gabor, D., *A new microscopic principle.* Nature, 1948. **161**: p. 777.
32. Yamaguchi, I. and T. Zhang, *Phase-shifting digital holography.* Opt. Lett., 1997. **22**(16): p. 1268-1270.
33. Mann, C.J., et al., *High-resolution quantitative phase-contrast microscopy by digital holography.* Opt. Express, 2005. **13**(22): p. 8693-8698.
34. Carl, D., et al., *Parameter-optimized digital holographic microscope for high-resolution living-cell analysis.* Appl. Opt., 2004. **43**(36): p. 6536-6544.
35. Marquet, P., et al., *Digital holographic microscopy: a noninvasive contrast imaging technique allowing quantitative visualization of living cells with subwavelength axial accuracy.* Opt. Lett., 2005. **30**(5): p. 468-470.
36. Lue, N., et al., *Quantitative phase imaging of live cells using fast Fourier phase microscopy.* Appl. Opt., 2007. **46**: p. 1836.
37. Ikeda, T., et al., *Hilbert phase microscopy for investigating fast dynamics in transparent systems.* Optics Letters, 2005. **30**(10): p. 1165-1167.
38. Popescu, G., et al., *Erythrocyte structure and dynamics quantified by Hilbert phase microscopy.* J. Biomed. Opt. Lett., 2005. **10**(6): p. 060503.
39. Park, Y.K., et al., *Diffraction phase and fluorescence microscopy.* Optics Express, 2006. **14**(18): p. 8263-8268.
40. Popescu, G., et al., *Diffraction phase microscopy for quantifying cell structure and dynamics.* Optics Letters, 2006. **31**(6): p. 775-777.
41. Wang, Z., et al., *Spatial light interference microscopy (SLIM).* Optics Express, 2011. **19**(2): p. 1016.
42. Bhaduri, B., et al., *Diffraction phase microscopy with white light.* Optics Letters, 2012. **37**(6): p. 1094-1096.

43. Edwards, C., et al., *Epi-illumination diffraction phase microscopy with white light.* Optics Letters, 2014. **39**(21): p. 6162-6165.
44. Zernike, F., *Phase contrast, a new method for the microscopic observation of transparent objects, Part 1.* Physica, 1942. **9**: p. 686-698.
45. Zernike, F., *Phase contrast, a new method for the microscopic observation of transparent objects, Part 2.* Physica, 1942. **9**: p. 974-986.
46. Zernike, F., *How I discovered phase contrast.* Science 1955. **121**: p. 345.
47. Mir, M., et al., *Measuring Cell Cycle-Dependent Mass Growth* Proc. Nat. Acad. Sci., 2011. **108**(32): p. 13124.
48. Wang, R., et al., *One-dimensional deterministic transport in neurons measured by dispersion-relation phase spectroscopy.* J. Phys.: Cond. Matter, 2011. **23**: p. 374107.
49. Wang, Z., et al., *Label-free intracellular transport measured by Spatial Light Interference Microscopy.* J. Biomed. Opt., 2011. **16**: p. 026019.
50. Wang, Z., et al., *Tissue refractive index as marker of disease.* J Biomed Opt, 2011. **16**(11): p. 116017.

CHAPTER 03: Quantitative Gleason Grading of Prostate Cancer

3.1 Abstract

1 in 7 men receive a diagnosis of prostate cancer in their lifetime. The aggressiveness of the treatment plan adopted by the patient is strongly influenced by Gleason grade. Gleason grade is determined by the pathologist based on the level of glandular formation and complexity seen in the patient's biopsy. However, studies have shown that the disagreement rate between pathologists on Gleason grades 3 and 4 is high and this affects treatment options. We used quantitative phase imaging to develop an objective method for Gleason grading. Using the glandular solidity, which is the ratio of the area of the gland to a convex hull fit around it, and anisotropy of light scattered from the stroma immediately adjoining the gland, we were able to quantitatively separate Gleason grades 3 and 4 with 81% accuracy in 43 cases marked as difficult by pathologists.

3.2 Motivation

98.9% of men diagnosed with prostate cancer between the years 2004 – 2010 survived 5 years or longer [1]. When the data is further categorized based on disease stage at diagnosis, 80.7% of the cancers were diagnosed at the local stage, during which the 5 year survival rate is 100% [1]. However, the 5-year survival rate for individuals with distant metastasis of prostate cancer is 28%. Hence diagnosis of prostate cancer at an early stage, when it has a higher chance for cure, is critical for patient survival. However, various studies have shown that not all prostate cancers diagnosed at an early stage require intervention [2, 3]. A particularly compelling argument towards this end was provided from a study by Porter et. al. that showed that 1.2 million new cases of prostate cancer would be diagnosed if all men between the ages of 62-75 years old underwent prostate biopsies, irrespective of their PSA levels [4]. Various nomograms and risk assessment tools have been developed to identify men with prostate cancer who have a higher risk of disease progression and mortality. The most commonly used tools include D'Amico risk stratification, CAPRA score, Kattan nomogram and Partin tables [5-8]. A patient's Gleason grade is an important consideration in each of these tools.

A patient's Gleason grade is determined by the pathologist based on the level of glandular differentiation seen in the H&E stained biopsy. A primary and secondary Gleason grade (1-5) is assigned based on the amount of biopsy area containing a particular pattern. The Gleason grades are added up to assign a Gleason score (1-10). The Gleason grade is considered to be an indicator of possible tumor size, metastasis and outcome [9-12]. A Gleason score of 6 or less is a common criteria used to adopt active surveillance as a prostate cancer management strategy [13]. Thus it's critical to ensure that the Gleason grade is correctly determined. The qualitative nature of Gleason grading can lead to a high degree of disagreements among various pathologists'

diagnoses. A study by Allsbrook et. al. showed that the level of under-grading of Gleason score 7 prostate cancer was 47% and that for Gleason score 8-10 prostate cancers was 25% among general pathologists [14]. When the same study was repeated on urologic pathologists, the agreement rate was 70% or higher in the Gleason score ranges of 2-4, 5-6, 7, 8-10 among the 38 consensus cases but there were 10 non-consensus cases [15]. Clearly, a quantitative technique that can objectively predict Gleason grades with a high degree of accuracy would assist pathologists in performing Gleason grading. This would also have important implications on prostate cancer treatment.

Quantitative phase imaging (QPI) of unstained tissue provides information on the refractive index distribution, or tissue morphology, with nanometer level sensitivity. Subtle morphological changes in both the epithelial and stromal regions of tissue, which are not visible in stained tissue sections used in current pathological settings, can be measured using QPI. Thus QPI would be a valuable addition to current diagnostic pathology. In this paper, we show the ability of QPI to help pathologists quantitatively and therefore, objectively differentiate between Gleason grade 3 and 4 prostate cancers.

3.3 Gleason Grading

The Gleason grade is the most widely used grading scheme in prostate cancer. The system was developed by Dr. Donald Gleason in the 1960s and is based on glandular differentiation seen in hematoxylin and eosin (H&E) stained slides [9, 16]. Pathologists determine Gleason grade based on glandular presence and differentiation in stroma [9, 16]. The Gleason score has been proven to be an indicator of tumor size, metastasis, treatment and outcome [9-12].

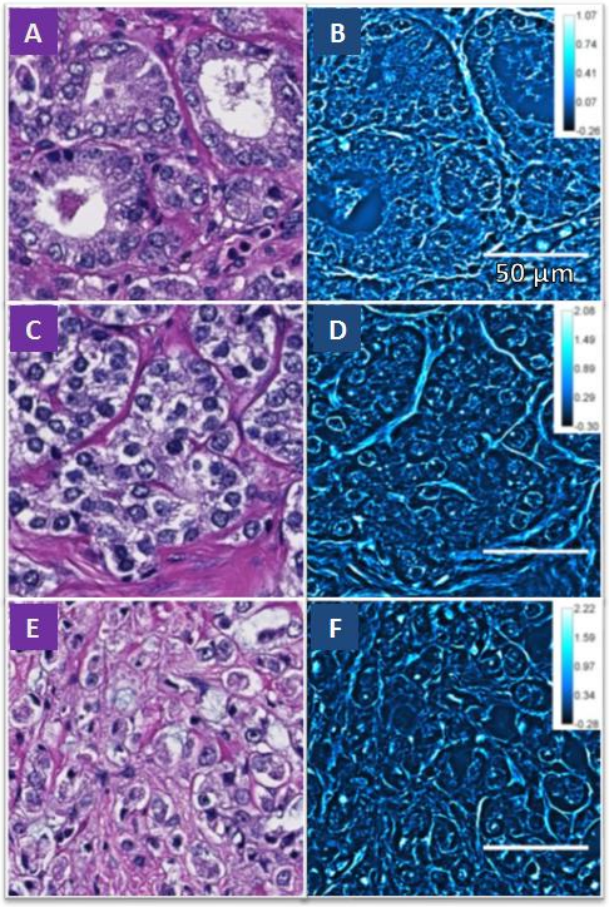

Figure 3.1: A side-by-side comparison of H&E and SLIM images of the same tissue microarray cores show that SLIM images reveal a lot more information about the tissue due to the intrinsic contrast in tissue. Single strands of stroma stand out in SLIM images as opposed to the uniform pink distribution seen in H&E images. In the zoomed in version of the image seen in figures **A & B**, the stroma separating glands pops out clearly in SLIM images enabling the classification of the glands as grade 3. Side-by-side comparison of Gleason grade 4 tissue microarray cores shown in **C & D** once again shows the ability of SLIM to detect stroma allowing for better visualization of fusing glands and stromal invasion allowing for accurate Gleason grading. Also, smaller structures within nuclei are more prominent. In the Gleason grade 5 images shown in **E & F**, the loss of glandularity and presence of epithelial cells in stroma are clearly visible in the SLIM images

The variation in grades on a scale from 1-5, in order of increasing severity, is based on glandular differentiation and glandular presence in stroma [9, 16-18]. The primary grade is the pattern present in maximum biopsy area and the secondary grade is the second most prominent pattern. The two grades are added to provide a Gleason score of 1-10.

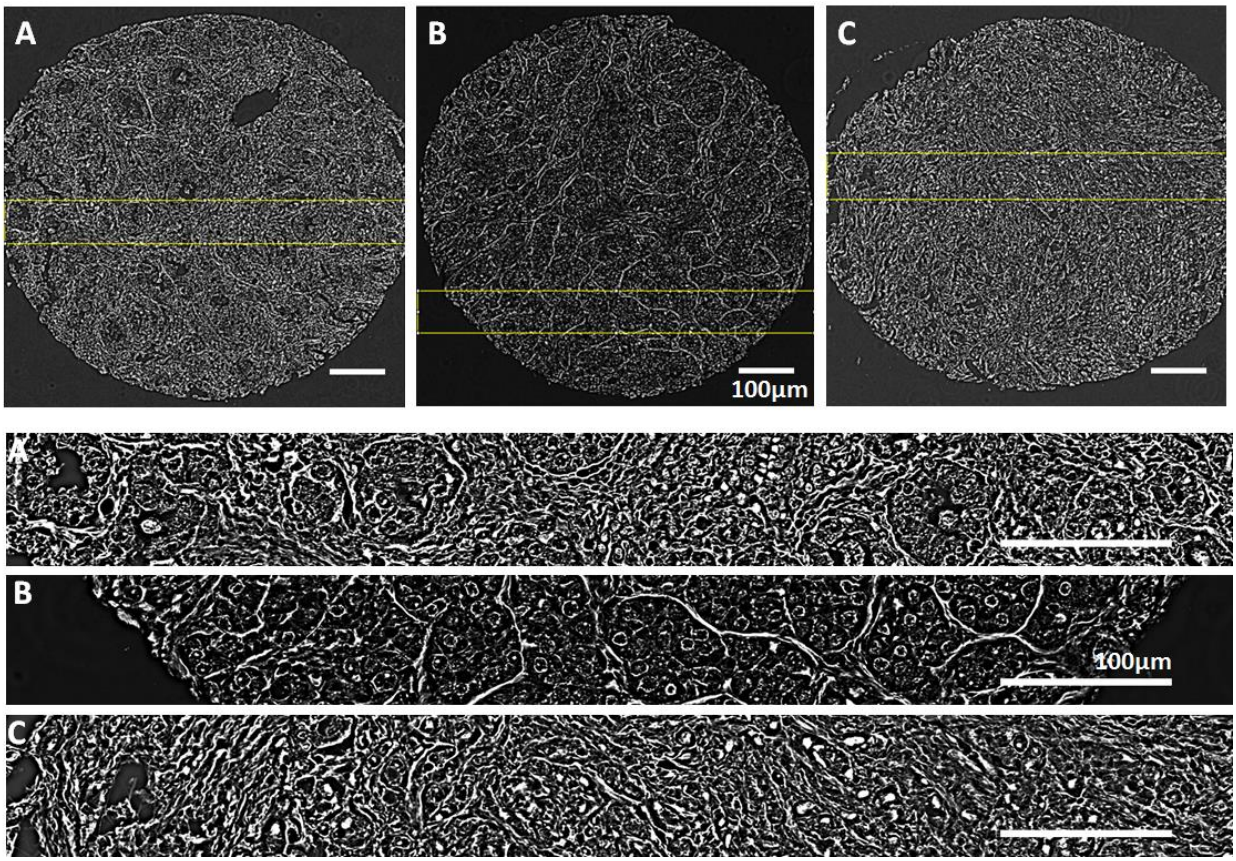

Figure 3.2: Zoomed in SLIM images of various Gleason grades. (A) Gleason grade 3 pattern with medium sized individual glands separated by stroma. **(B)** Gleason grade 4 pattern with small merging glands showing loss of stromal separation. **(C)** Gleason grade 5 pattern with no visible glands and individual cells interspersed in the stroma.

In current clinical practice, grades 1 and 2 are rarely diagnosed. Gleason grade 3 glands are medium to small size, singular with infiltrating edges as seen in Figs 3.1-A,B which shows a side-by-side comparison of H&E and SLIM images. In a zoomed-in version of Gleason grade 3 in figure 3.2-A, stroma between adjacent glands is clearly visible, thus, aiding the determination of the grade [9]. Gleason grade 4 consists of small glands that are fusing into one another (Figs 3.1-C, D; Fig 3.2-B) [9]. Gleason grade 5 represents the most severe cancer where glandular architecture is lost and epithelial cells are distributed individually or in sheet like patterns in the stroma (Figs 3.1-E, F) [16].

In the zoomed-in version in Fig 3.2-C, no glands are visible and epithelial cells can be seen between stromal fibers.

3.4 Quantitative Separation of Gleason Grade 3 and 4

43 cases from the TMA 2 data set with consensus diagnosis from 3 pathologists were analyzed. 22 cores with only Gleason grade 3 glands from patients with a final diagnosis of Gleason 3+3 cancer and 21 cores with only Gleason 4 glands and final diagnosis of Gleason 4+4 cancer were imaged using SLIM. Solidity, which the ratio of the area of the gland to that of a convex hull fit around the gland, was measured for all glands in the cores. Additionally, anisotropy, which is the average cosine of the scattering angle, was measured for the layer of stroma surrounding all the glands. Our study showed that Gleason 3 glands had a higher degree of solidity and higher values of anisotropy in the stroma immediately adjoining the gland (Fig. 3.3). Using glandular solidity and stromal anisotropy alone, 81% of the Gleason grade 4 cores and 82% of the Gleason grade 3 cores were correctly classified. We believe the higher glandular solidity values can be explained by the reduced invasive edges and lower degree of glandular fusion seen in Gleason 3 glands. Additionally, the lower value of anisotropy seen around Gleason grade 4 glands means the stromal layer has a higher level of disorder in advanced stages of disease.

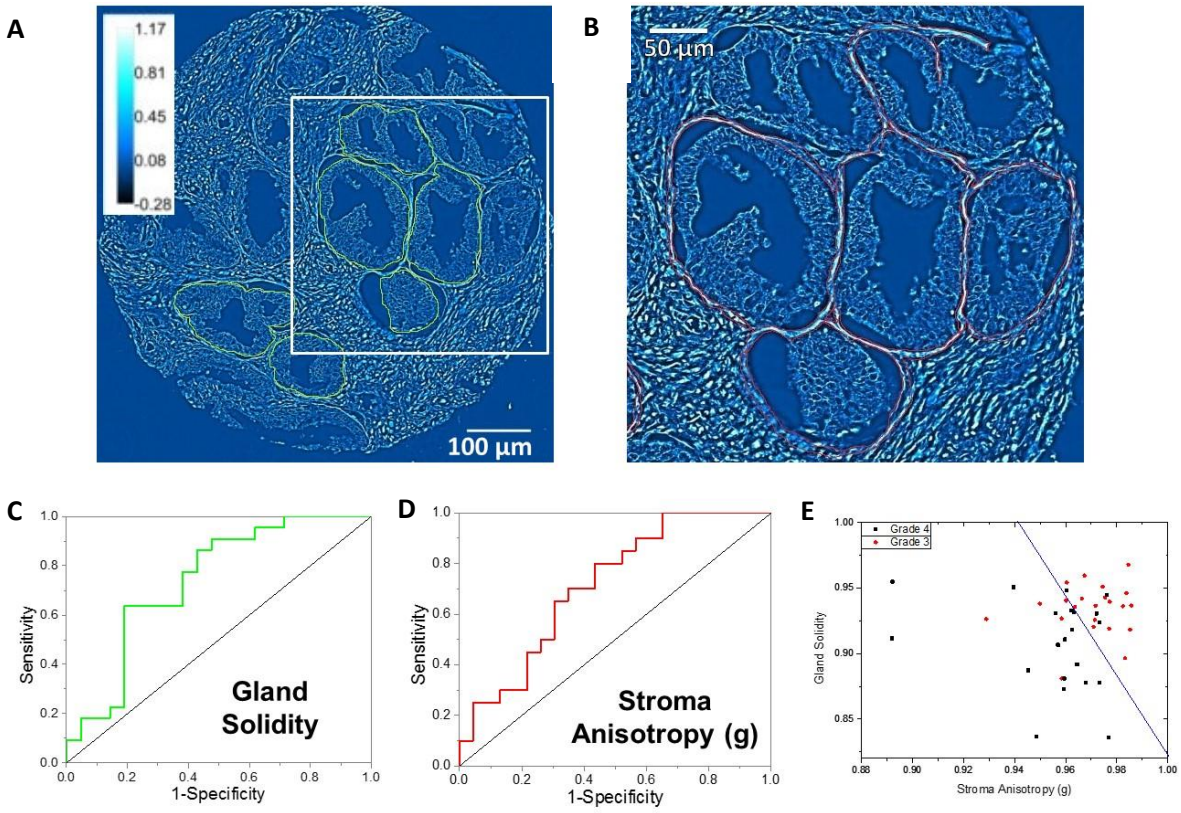

Figure 3.3: Quantitative Gleason Grading in prostate cancer tissue: SLIM images show clear distinction between glands and stroma. This helps us isolate glands as well as single strands of stroma immediately adjoining glands. **(A)** Gleason grade 4 tissue microarray core where glands are starting to lose stromal separation and are merging into each other. Using ImageJ and a tablet we manually marked glands and measured the solidity. Solidity is defined as the ratio of the area of the gland to the area of a convex hull fitted to the gland. This parameter varies from 0 to 1; with 1 being a perfect polygon. **(B)** In a zoomed in region from (A), we isolate the single layer of stroma immediately adjoining the glands. We calculate optical anisotropy which is directly proportional to the square of the ratio of the phase gradient to the phase variance in that region. Optical anisotropy is an indicator of forward scattering of light in the tissue region, also a label-free indicator of morphological changes in tissue at the nano-scale level. **(C)** Solidity is useful in separation of Gleason grade 3 and 4 glands (AUC 0.74). By using a cut-off value of 0.9188 we can classify grade 3 glands with an accuracy of 86% and grade 4 glands at 57% accuracy. **(D)** Optical anisotropy in stroma is useful in separating Grade 4 glands with an accuracy of 80% and Gleason grade 3 glands with 56% accuracy (AUC 0.72). **(E)** By combining the optical anisotropy in stroma and the solidity of glands, we can separate Gleason grade 3 and 4 glands with an overall accuracy of 81.39%; with Grade 3 glands classified with 81% accuracy and Grade 4 glands classified at 82% accuracy. Grade 3 glands have a higher solidity index in the glands and higher anisotropy value in the stroma immediately adjoining glands.

3.5 Discussion

Glandular solidity is an indicator of glandular shape, and decrease in solidity is a reflection of invasive edges. This strongly correlates with morphological indicators currently used by pathologists for qualitative Gleason grading performed on H&E stained images. By combining glandular shape descriptors with stromal morphology measurements, QPI was able to distinguish between the Gleason grade 3 and 4 prostate cancers with an accuracy of 81.39%.

The stromal changes reported in the layer adjoining cancerous glands are not currently used in pathology for Gleason grading of prostate cancer. The stroma is a complex environment consisting of the extracellular matrix, fibroblasts, smooth muscle cells, growth factors, regulatory receptors, blood vessels, nerve fibers and immune cells [19]. In the prostate, the primary stromal components are fibroblasts and smooth muscle cells [20]. The various components of the stroma provide adhesion, growth factor secretion and regulation, structural framework and support, cell attachment and migration and permeability [21, 22]. In response to carcinoma in the epithelium, the repair mechanism in stroma is activated [23]. The stromal changes seen in cancer using immunohistochemistry or molecular studies mimic the changes seen in wound healing mechanisms such as increased growth factor secretion, angiogenesis, matrix remodeling, elevated immune response and increased protease activity [24-28]. These changes also include a switch to the activated myofibroblast phenotype from fibroblast characterized by increased secretion of vimentin and smooth muscle to myofibroblast with reduced levels of α-smooth muscle actin and calponin [23, 26, 27, 29, 30]. In immunohistochemistry studies performed by other groups, hyaluronan (HA) level was observed to be high in the stroma of prostate biopsies of higher Gleason grades but HA receptor CD 44 level is inversely related to Gleason grade [31].

High platelet-dervived growth factor (PDGFR-β) expression and low expression of whey acidic protein family member WFDC1/PS20 has also been seen in stroma adjoining high Gleason grade glands [32, 33]. In another study, an increased level of stromal cells with fibroblast and myo-fibroblast phenotype and reduced levels of smooth muscle actin cells were observed in proliferative cancerous tissue of prostate [34]. In-vitro studies have shown the ability of prostate fibroblasts to transform into myo-fibroblast cells [35, 36].

The importance of stromal regulation of prostatic epithelium has been demonstrated in in-vitro studies in the past. Prostate epithelium cultured on reconstituted extra-cellular matrix showed increased levels of prostate specific antigen and prostatic acid phosphatase as opposed to increased cell growth and reduced PSA, PAP levels seen in cells grown on plastic plates [37]. In our study, we saw changes in the single layer of stroma adjoining glandular epithelium. This might be indicative of stroma-epithelial cross-talk previously seen in literature.

While the label-free nature of SLIM prevents us from knowing the exact molecular or morphological change that leads to the increased diversity we see in the anisotropy measurement, all the changes documented with immunohistochemistry would contribute to increased disorganization in the stroma which we measure as optical anisotropy, a highly sensitive indicator of morphological changes. One advantage of SLIM is that we can measure the final effect of all the molecular changes which cannot be done in immunohistochemistry due to its inherent reactive nature.

SLIM shows the potential to guide treatment decisions for prostate cancer at the diagnostic stage by improving the current accuracy of Gleason grading seen in pathology. In the next chapters, I

show how anisotropy reports on prostate cancer prognosis with more sensitivity than Gleason grading.

3.6 Materials and Methods

3.6.1 TMA Cohort for the Gleason Grading Study

The tissue microarray (TMA) set used for the Gleason grading study was obtained from the National Cancer Institute Cooperative Prostate Cancer Tissue Resource (NCI-CPCTR). The tissue was collected at four academic institutions: George Washington University, New York University, University of Pittsburg, and Medical College of Wisconsin. Procedures, policies and protocols for TMA construction and slide preparation are available at the CPCTR website [38, 39]. The Gleason TMA set includes prostatectomy tissue from 250 patients and includes controls from 18 benign hyperplasia cases. It also includes information on the patient's final Gleason grade diagnosis. The tissue was arrayed into 4 blocks and two 4μm sections were cut. One was deparaffinized and stained with H&E for pathology control. The adjacent section was deparaffinized and coverslipped without staining for SLIM imaging. The studies have been performed in the United States in accordance with the procedure approved by the Institutional Review Board at University of Illinois at Urbana-Champaign (IRB Protocol Number: 13900).

3.6.2 SLIM Imaging System

Spatial Light Interference Microscopy (SLIM) is a quantitative phase imaging system that was developed as an add-on module to a commercial phase contrast microscope and is described in detail in Ref. [40]. Briefly, the back focal plane of the phase contrast objective is projected onto a liquid crystal phase modulator (LCPM). At the LCPM, three $\pi/2$ phase shifts, additional to the one already present in the phase contrast image, are introduced and recorded by the CCD. The four intensity images corresponding to each phase shift are recorded, and a final phase image is computed from the information. The final phase image computed corresponds to:

$$\phi(x,y) = \frac{2\pi}{\lambda} \int_0^{h(x,y)} (n(x,y,z) - n_0)\, dz$$

Where $\phi(x,y)$ is the phase at a given point, λ is the center wavelength of the white light source (552.3nm), $n(x,y,z)$ is the refractive index at a given point and n_0 is the refractive index of the surrounding medium. The refractive index difference is integrated over the entire thickness of the sample to measure the phase. SLIM has a transverse resolution of 0.4 microns and a spatial path length sensitivity of 0.3nm.

The SLIM system was modified to raster scan through large fields of view and stitch the frames together. This provides the high throughput necessary for whole slide imaging. The samples used in this study were imaged using the 40X/0.75NA objective of the SLIM system.

3.6.3 Optical Anisotropy

Optical anisotropy is defined as the average cosine of the scattering angle associated with a single scattering event. Since QPI records both the amplitude and the phase of the light passing through the sample, it has the ability to measure light scattering parameters. Using the scattering phase theorem, the optical anisotropy of light passing through the tissue can be measured as [41]

$$g = 1 - \frac{1}{2k_0^2} \frac{\langle |\nabla[\varphi(r)]|^2 \rangle_r}{\langle \Delta\varphi^2(r) \rangle_r^2}$$

Where k0 is the wave number of the light source, $\nabla[\varphi(r)]$ is the phase gradient and $\Delta\varphi^2(r)$ is the variance of the phase. The phase gradient and phase variance are averaged over a tissue region of interest, r. In our study, the region of interest was a single layer of stroma immediately adjoining the glands, as shown in Fig. 3.4.

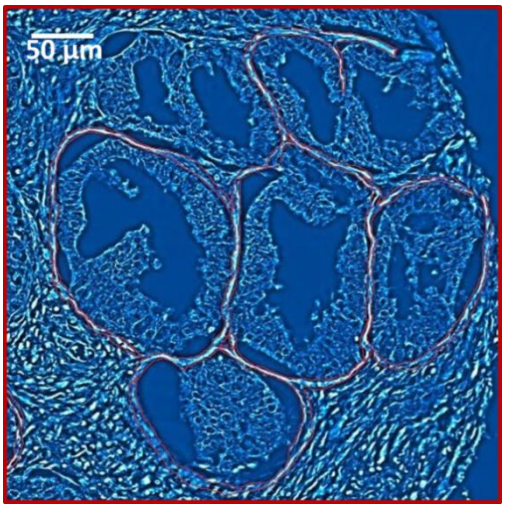

Figure 3.4: Stromal Region Selection. A single layer of stroma immediately adjoining these glands is highlighted in red in the above image. We calculate optical anisotropy in this layer of stroma using the scattering phase theorem.

3.6.4 Solidity

Glandular solidity is defined the ratio of the area of the gland to that of the area of a convex hull fit around the gland (Fig. 3.5). This parameter is an indicator of the uniformity of the edges of the selected tissue region. In order to measure glandular solidity, the glands of interest were selected using the ROI feature on ImageJ. ImageJ was then used to measure the area of the gland, fit a convex hull around the gland, measurement of the area of the convex hull and finally, the solidity.

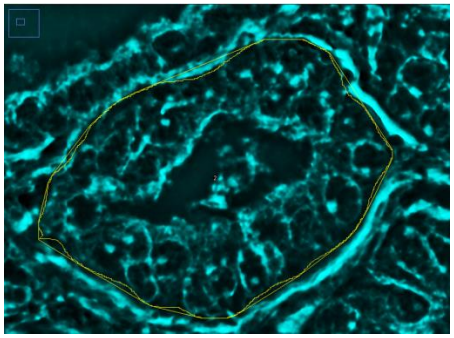

Figure 3.5: Glandular Solidity. Solidity is defined as the ratio of the area of the gland to the area of the convex hull or polygonal fit around the gland. In the above image, the inner boundary is the ROI of the gland, and the outer boundary shows the convex hull around the gland.

3.7 References

1. Howlader N, N.A., Krapcho M, Garshell J, Miller D, Altekruse SF, Kosary CL, Yu M, Ruhl J, Tatalovich Z,Mariotto A, Lewis DR, Chen HS, Feuer EJ, Cronin KA. *SEER Cancer Statistics Review, 1975-2011*. 2014 2012 [cited 2014 September, 10].
2. Bill-Axelson, A., et al., *Radical Prostatectomy or Watchful Waiting in Early Prostate Cancer.* New England Journal of Medicine, 2014. 370(10): p. 932-942.
3. Wilt, T.J., et al., *Radical Prostatectomy versus Observation for Localized Prostate Cancer.* New England Journal of Medicine, 2012. 367(3): p. 203-213.
4. Porter, M.P., J.L. Stanford, and P.H. Lange, *The distribution of serum prostate-specific antigen levels among American men: Implications for prostate cancer prevalence and screening.* Prostate, 2006. 66(10): p. 1044-1051.
5. Partin, A.W., et al., *Contemporary update of prostate cancer staging nomograms (Partin tables) for the new millennium.* Journal of Urology, 2002. 168(1): p. 374-375.
6. Kattan, M.W., et al., *A preoperative nomogram for disease recurrence following radical prostatectomy for prostate cancer.* Journal of the National Cancer Institute, 1998. 90(10): p. 766-771.
7. D'Amico, A.V., et al., *Biochemical outcome after radical prostatectomy, external beam radiation therapy or interstitial radiation therapy for clinically localized prostate cancer.* Renal, Bladder, Prostate and Testicular Cancer: An Update, 2001: p. 147-157.
8. Cooperberg, M.R., et al., *The University of California, San Francisco cancer of the prostate risk assessment score: A straightforward and reliable preoperative predictor of disease recurrence after radical prostatectomy.* Journal of Urology, 2005. 173(6): p. 1938-1942.
9. Humphrey, P.A., *Gleason grading and prognostic factors in carcinoma of the prostate.* Mod Pathol, 2004. 17(3): p. 292-306.
10. Epstein, J.I., et al., *Prediction of progression following radical prostatectomy. A multivariate analysis of 721 men with long-term follow-up.* Am J Surg Pathol, 1996. 20(3): p. 286-92.
11. Partin, A.W., et al., *Combination of prostate-specific antigen, clinical stage, and Gleason score to predict pathological stage of localized prostate cancer. A multi-institutional update.* JAMA, 1997. 277(18): p. 1445-51.
12. Egevad, L., et al., *Prognostic value of the Gleason score in prostate cancer.* BJU Int, 2002. 89(6): p. 538-42.
13. Dall'Era, M.A., et al., *Active surveillance for early-stage prostate cancer.* Cancer, 2008. 112(8): p. 1650-1659.
14. Allsbrook, W.C., Jr., et al., *Interobserver reproducibility of Gleason grading of prostatic carcinoma: general pathologist.* Hum Pathol, 2001. 32(1): p. 81-8.
15. Allsbrook, W.C., Jr., et al., *Interobserver reproducibility of Gleason grading of prostatic carcinoma: urologic pathologists.* Hum Pathol, 2001. 32(1): p. 74-80.
16. Gleason, D.F., *Classification of prostatic carcinomas.* Cancer Chemother Rep, 1966. 50(3): p. 125-8.
17. Gleason, D.F. and G.T. Mellinger, *Prediction of prognosis for prostatic adenocarcinoma by combined histological grading and clinical staging. 1974.* J Urol, 2002. 167(2 Pt 2): p. 953-8; discussion 959.
18. Gleason, D.F. and G.T. Mellinger, *Prediction of prognosis for prostatic adenocarcinoma by combined histological grading and clinical staging.* J Urol, 1974. 111(1): p. 58-64.

19. Farnsworth, W.E., *Prostate stroma: physiology.* The Prostate, 1999. 38(1): p. 60-72.
20. Tuxhorn, J.A., et al., *Reactive stroma in human prostate cancer: induction of myofibroblast phenotype and extracellular matrix remodeling.* Clinical cancer research : an official journal of the American Association for Cancer Research, 2002. 8(9): p. 2912-23.
21. *Guidebook to the extracellular matrix and adhesion proteins Edited by T Kreis and R Vale. pp 176. Oxford University Press. 1993. £40 or £18.50 (pbk) ISBN 0-19-859934-X or -859933-1s.* Biochemical Education, 1993. 21(4): p. 209-210.
22. Taipale, J. and J. KeskiOja, *Growth factors in the extracellular matrix.* Faseb Journal, 1997. 11(1): p. 51-59.
23. Tuxhorn, J.A., G.E. Ayala, and D.R. Rowley, *Reactive stroma in prostate cancer progression.* The Journal of urology, 2001. 166(6): p. 2472-83.
24. Noel, A. and J.M. Foidart, *The role of stroma in breast carcinoma growth in vivo.* Journal of mammary gland biology and neoplasia, 1998. 3(2): p. 215-25.
25. Gregoire, M. and B. Lieubeau, *The role of fibroblasts in tumor behavior.* Cancer metastasis reviews, 1995. 14(4): p. 339-50.
26. Ayala, G., et al., *Reactive stroma as a predictor of biochemical-free recurrence in prostate cancer.* Clinical cancer research : an official journal of the American Association for Cancer Research, 2003. 9(13): p. 4792-801.
27. Ronnov-Jessen, L., O.W. Petersen, and M.J. Bissell, *Cellular changes involved in conversion of normal to malignant breast: importance of the stromal reaction.* Physiol Rev, 1996. 76(1): p. 69-125.
28. Rowley, D.R., *What might a stromal response mean to prostate cancer progression?* Cancer metastasis reviews, 1998. 17(4): p. 411-9.
29. Schmitt-Graff, A., A. Desmouliere, and G. Gabbiani, *Heterogeneity of myofibroblast phenotypic features: an example of fibroblastic cell plasticity.* Virchows Archiv : an international journal of pathology, 1994. 425(1): p. 3-24.
30. Seemayer, T.A., et al., *Myofibroblasts in the stroma of invasive and metastatic carcinoma: a possible host response to neoplasia.* The American journal of surgical pathology, 1979. 3(6): p. 525-33.
31. Lipponen, P., et al., *High stromal hyaluronan level is associated with poor differentiation and metastasis in prostate cancer.* Eur J Cancer, 2001. 37(7): p. 849-56.
32. Hagglof, C., et al., *Stromal PDGFRbeta expression in prostate tumors and non-malignant prostate tissue predicts prostate cancer survival.* PLoS One. 5(5).
33. McAlhany, S.J., et al., *Decreased stromal expression and increased epithelial expression of WFDC1/ps20 in prostate cancer is associated with reduced recurrence-free survival.* Prostate, 2004. 61(2): p. 182-91.
34. Hayward, S.W., G.R. Cunha, and R. Dahiya, *Normal development and carcinogenesis of the prostate. A unifying hypothesis.* Annals of the New York Academy of Sciences, 1996. 784: p. 50-62.
35. Peehl, D.M. and R.G. Sellers, *Induction of smooth muscle cell phenotype in cultured human prostatic stromal cells.* Experimental cell research, 1997. 232(2): p. 208-15.
36. Gerdes, M.J., et al., *Regulation of rat prostate stromal cell myodifferentiation by androgen and TGF-beta1.* The Prostate, 2004. 58(3): p. 299-307.

37. Fong, C.J., et al., *Reconstituted Basement-Membrane Promotes Morphological and Functional-Differentiation of Primary Human Prostatic Epithelial-Cells.* Prostate, 1991. 19(3): p. 221-235.
38. Berman, J.J., et al., *The tissue microarray data exchange specification: implementation by the Cooperative Prostate Cancer Tissue Resource.* BMC Bioinformatics, 2004. 5: p. 19.
39. Kajdacsy-Balla, A., et al., *Practical aspects of planning, building, and interpreting tissue microarrays: the Cooperative Prostate Cancer Tissue Resource experience.* J Mol Histol, 2007. 38(2): p. 113-21.
40. Wang, Z., et al., *Spatial light interference microscopy (SLIM).* Optics Express, 2011. 19(2): p. 1016.
41. Wang, Z., H. Ding, and G. Popescu, *Scattering-phase theorem.* Optics Letters, 2011. 36: p. 1215.

CHAPTER 04: Post-Prostatectomy Prediction of Prostate Cancer Recurrence – Nested Case Control Study

4.1 Abstract

The risk of biochemical recurrence of prostate cancer among individuals who undergo radical prostatectomy for treatment is around 25%. Current clinical methods often fail at successfully predicting recurrence among patients at intermediate risk for recurrence. We used a label-free method, spatial light interference microscopy, to perform localized measurements of light scattering in prostatectomy tissue microarrays. We show, for the first time to our knowledge, that anisotropy of light scattering in the stroma immediately adjoining cancerous glands can be used to identify patients at higher risk for recurrence. The data show that lower value of anisotropy corresponds to a higher risk for recurrence, meaning that the stroma adjoining the glands of recurrent patients is more fractionated than in non-recurrent patients. Our method outperformed the widely accepted clinical tool CAPRA-S in the cases we interrogated irrespective of Gleason grade, prostate-specific antigen (PSA) levels and pathological tumor-node-metastasis (pTNM) stage. These results suggest that QPI shows promise in assisting pathologists to improve prediction of prostate cancer recurrence.

4.2 Motivation

The Surveillance, Epidemiology, and End Results (SEER) program by the National Cancer Institute (NCI) estimates that while 233,000 men will be diagnosed with prostate cancer in 2014 in USA alone accounting for 14.0% of all cancer cases, the number of men who will die of the disease is 29,480 accounting for 5.0% of all cancer deaths [1]. Because most prostate cancers are not lethal, active surveillance is a desirable treatment option for patients presenting with localized prostate cancer, low prostate specific antigen (PSA) levels, and low risk according to the D'Amico risk category (see Supplemental Information for a brief review of this metric) [2]. However, radical prostatectomy reduces the risk of bone metastasis and mortality among patients in the intermediate and high risk categories [2]. Studies have shown that the risk of biochemical recurrence, which is defined as increasing serum PSA levels, is around 25% in men who undergo radical prostatectomy, whereas the risk of prostate cancer specific mortality in the same group is 7-12% [3-5].

Clearly, a method capable of forecasting recurrence is highly desirable. The commonly used tools to predict biochemical prostate cancer recurrence after prostatectomy, Kattan nomogram and Cancer of the Prostate Risk Assessment (CAPRA-S score), have c-index values ranging from 0.76-0.81 (see Supplemental Information for a review of this metric) [6, 7]. Here we studied pairs of subjects with similar CAPRA-S scores but different outcomes; one member of the pair had biochemical recurrence while the other one did not. In our study, we targeted the groups where existing methods have a discriminatory ability of 0.5. In essence, we used difficult cases where these methods fail to identify patients at high risk of recurrence after prostatectomy. We used quantitative phase imaging (QPI) to measure scattering anisotropy in the stroma adjoining glands in prostatectomy tissue microarrays. We were able to differentiate between

recurrent and non-recurrent groups with an area under the receiver-operating characteristic curve (AUC) of 0.72 in 181 difficult cases (3-4 cores per case) regardless of age of the patient, pathologic staging and Gleason grade scores. Our technique exploits *light scattering* signatures in the stroma as a predictive marker.

Light *scattering* rather than *absorption* is the physical phenomenon that renders our bodies opaque to visible radiation. Elastic light scattering, i.e., modification of the direction of propagation without change in wavelength, is induced by the inhomogeneity of tissue at multiple spatial scales. Measuring certain properties of the scattered field (e.g., angular distribution, optical spectrum) informs on the morphology of healthy and diseased tissues. Thus, solving a scattering *inverse problem* holds valuable diagnosis potential. Scattering differences measured using optical coherence tomography have been used as a diagnostic measure for *in-vivo* cancer diagnosis in bladder, esophagus, skin, uterus, stomach and breast [8-14]. These studies concluded that scattering was stronger in cancerous regions when compared to normal tissue. Studies on colorectal and pancreatic cancer using enhanced backscattering spectroscopy and partial wave spectroscopy have shown the potential of scattering parameters in studying the field effect of cancer [15, 16]. However, scattering signatures in the stroma and the epithelium cannot be assessed separately using these methods due to low spatial resolution.

While carcinoma itself is uncontrolled proliferation of epithelial cells, it also leads to many changes in the stromal microenvironment with positive feedback into epithelial growth promotion. The importance of stroma has been documented in mouse models, where the implanted cancer is more aggressive when the xenograft has both cancerous epithelium and fibroblasts [17]. The study of stroma as a separate entity is relatively new in optical diagnosis.

Second harmonic generation (SHG) studies on ovarian and breast stroma showed that malignant tumors exhibit greater organization in the collagen fibrils with a more uniform orientation [18, 19]. Further SHG studies in breast showed that the linear orientation of collagen in a direction perpendicular to the cancerous glands, also known as the TACS-3 signature, is associated with poor prognosis in breast cancer [20]. In malignant ovarian tissue, it was shown that, due to this perpendicular alignment, the stromal region adjoining the gland in a parallel orientation show a fractionated appearance [19]. Importantly, light scattering by shorter filaments results in a more isotropic angular distribution. However, structural information obtained using SHG might be incomplete since the signal can only be generated by non-centrosymmetric structures. Additionally, SHG signal amplitude is largely qualitative, as it depends not only on tissue structure, but also the phase matching condition, which cannot be controlled.

Spatial light interference microscope (SLIM) is a QPI technique, central to our approach (see Figure 4.1A and Refs. [21, 22]). SLIM uses a commercial phase contrast microscope and white light illumination, resulting in nanometer scale sensitivity to optical pathlength shifts [23]. In essence, SLIM combines phase contrast microscopy with holography. The instrument was programmed to scan microscope slides containing 320-360 individual cores, as illustrated in Fig. 4.2.

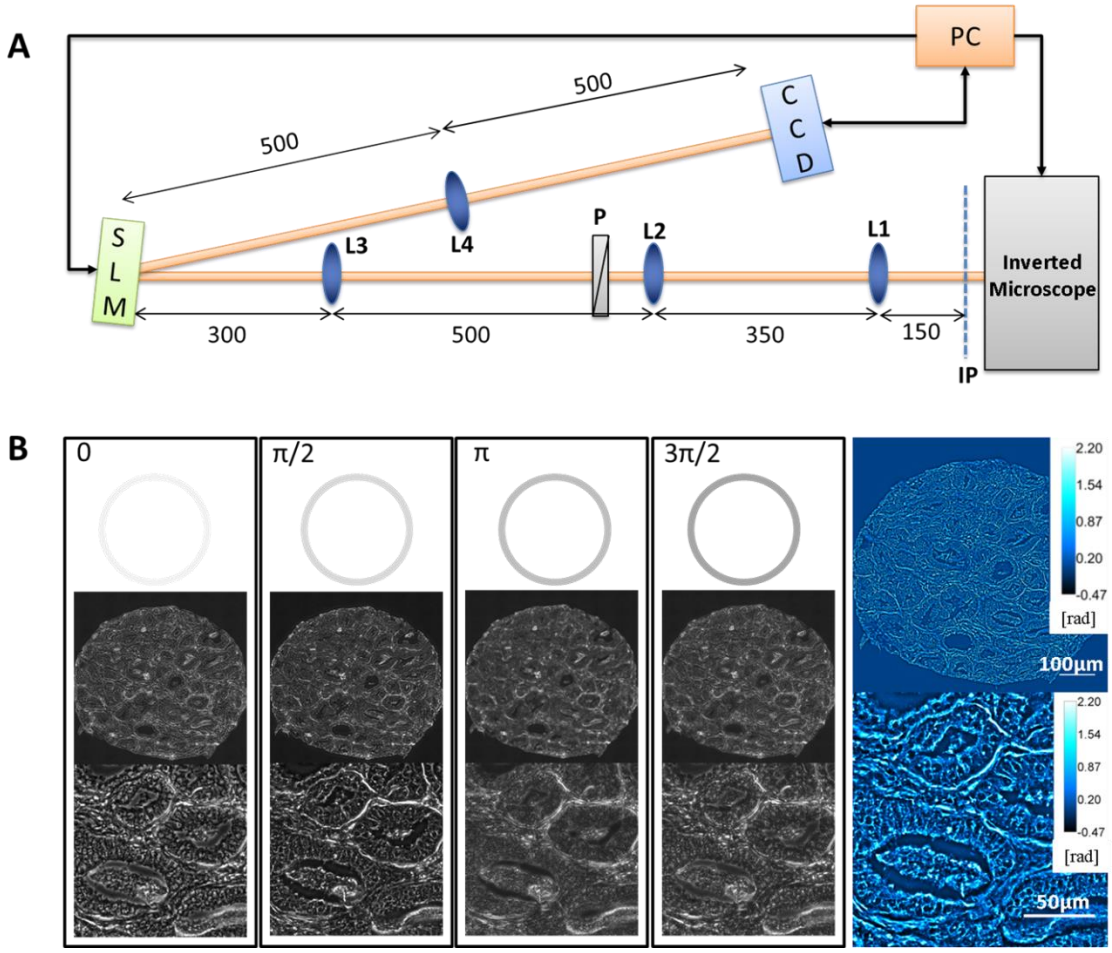

Figure 4.1: The imaging system. (A) The SLIM set-up is an add-on module to a commercial phase contrast microscope. The first set of lenses (L1 and L2) magnify the image to maintain the resolution of the microscope. The Fourier transform of the image plane is projected by lens L3 onto the spatial light modulator (SLM) where the phase pattern is shifted in phase 4 times, in increments of π/2. The lens L4 Fourier transforms the pattern on the SLM and the final image is recorded onto the CCD and stored on the computer. **(B)** Four phase shifted images recorded using a 40X/0.75NA objective with the final quantitative phase image shown on the right. Color bars indicate phase values in radians.

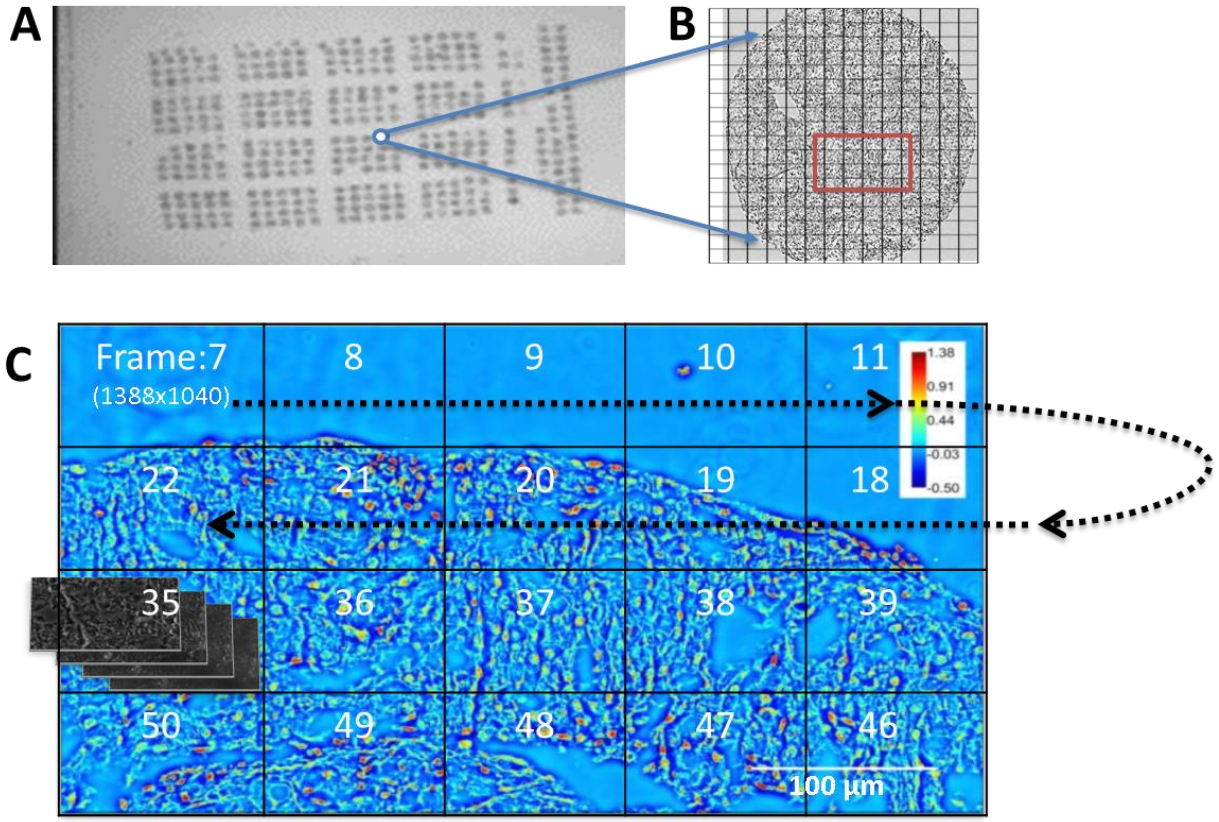

Figure 4.2: Mosaic SLIM imaging of an unstained tissue microarray. A) Unstained tissue microarray slide. B) The mosaic is set up around the core of interest. C) The recording at each tile proceeds as shown by the arrow. For each 1388x1040 pixel SLIM tile, four intensity images are recorded. The phase images are then stitched together using an ImageJ plugin built in our lab.

The resulting SLIM image contains rich information about tissue morphology, with the glandular epithelium and stroma structures clearly resolved (Fig. 4.3). This allows us to interrogate scattering changes specific to prostate stroma. In the past, SLIM has shown potential for prostate cancer diagnosis [21]. A question of great importance in prostate cancer is the prediction of a patient's prognosis. In this paper, we used an unstained prostate tissue microarray containing

prostatectomy samples of patients with and without biochemical recurrence of cancer, and studied changes in scattering signatures to identify patients at higher risk for recurrence.

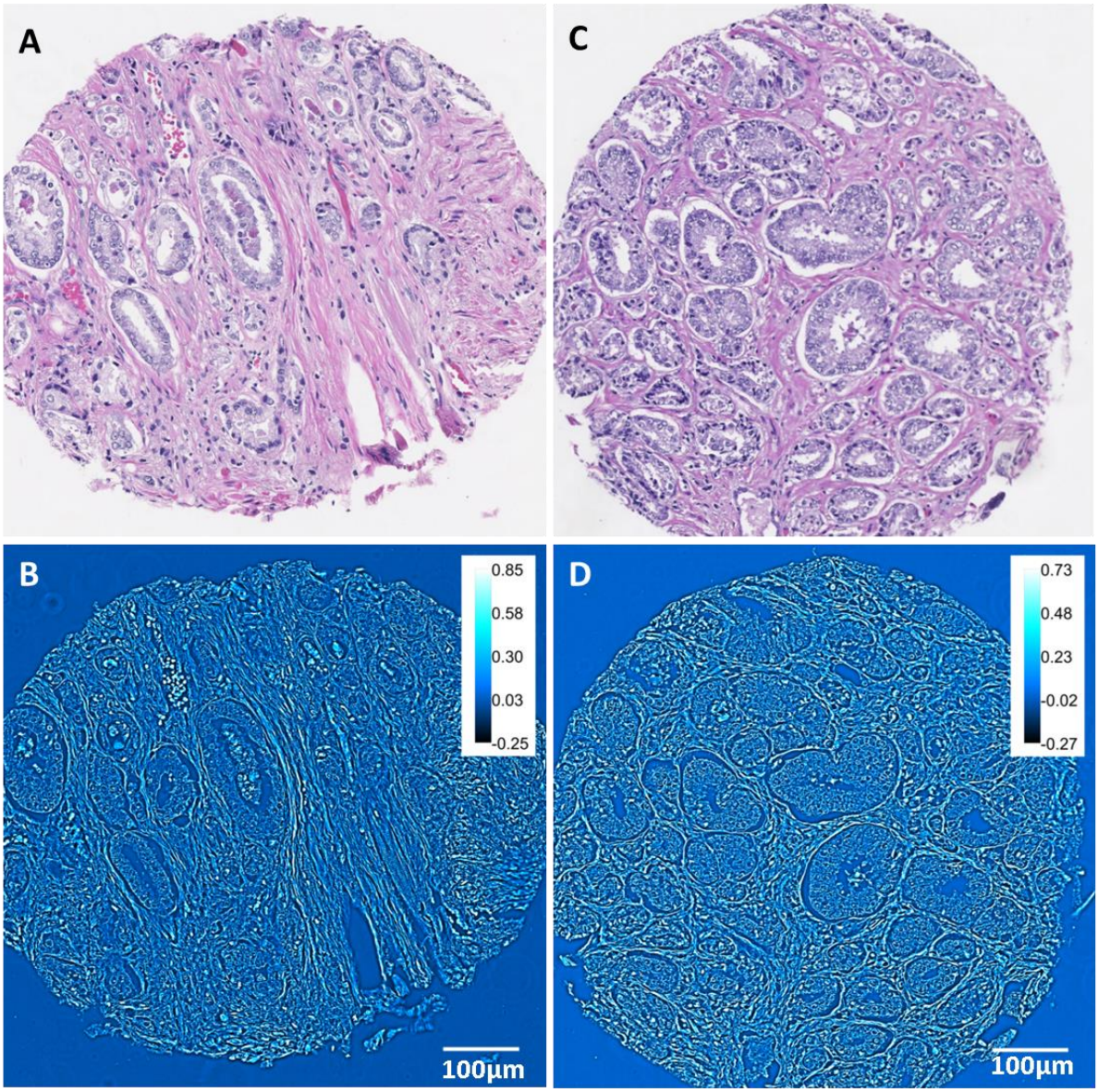

Figure 4.3: Comparison of H&E and SLIM images. A-B) H&E and SLIM images corresponding to a patient who had biochemical recurrence of prostate cancer after undergoing radical prostatectomy. **C-D)** H&E and SLIM images corresponding to the matched twin who did not have cancer recurrence. Both patients had Gleason score 7 (3+4) prostate cancer of pT2b stage without seminal vesicle invasion, no extra-prostatic extensions and surgical margins were free of cancer. The H&E images themselves do not provide any information about recurrence.

4.3 Anisotropy as a recurrence predictor

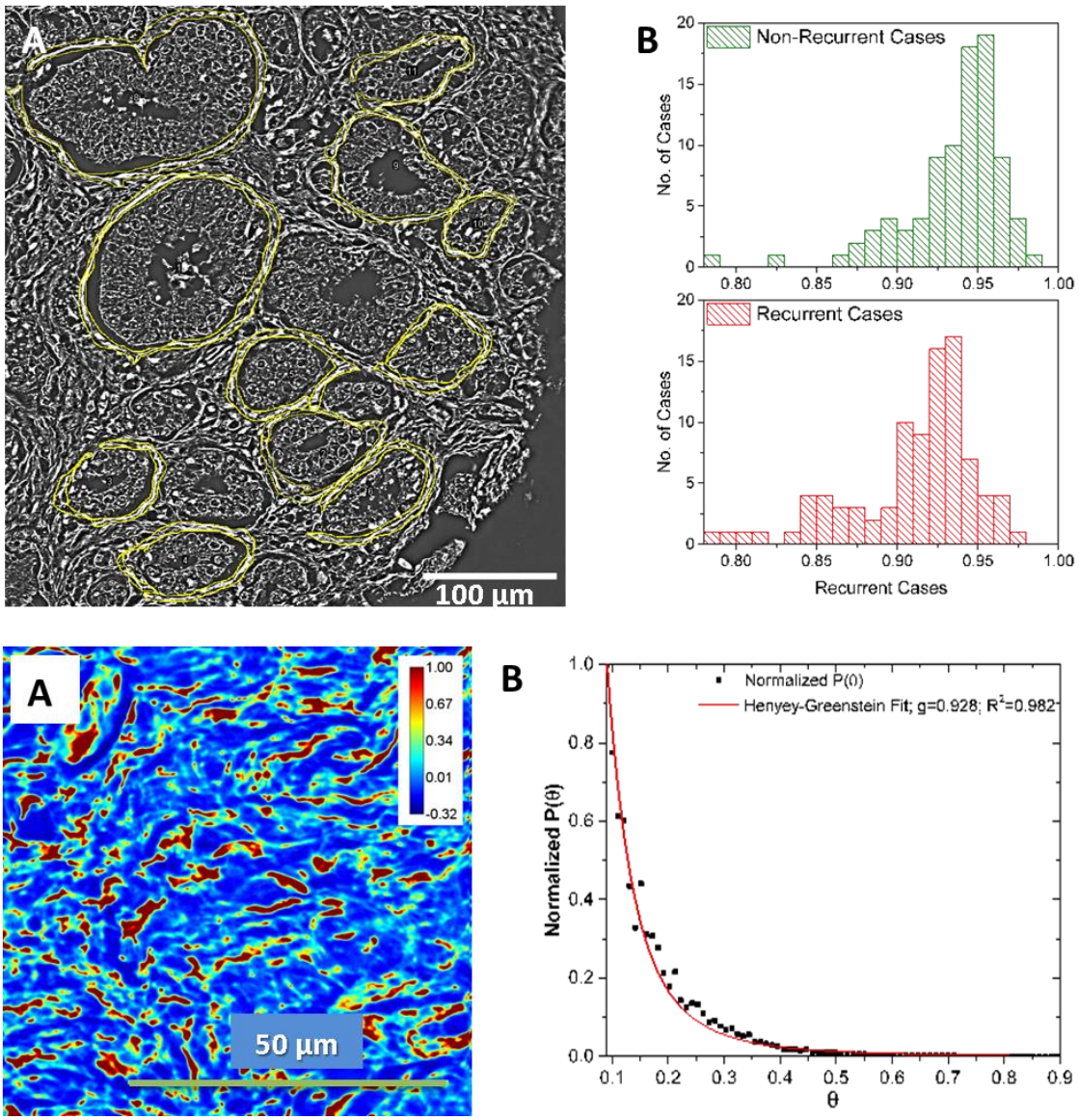

Figure 4.4: Optical Anisotropy Calculation. A) Optical anisotropy (g) was calculated in the single layer of stroma immediately adjoining multiple glands in each core. **B)** The histograms show the distribution of anisotropy values among the 89 non-recurrent and 92 recurrent cases. The bin-size on the histogram was set at 0.01. **C)** SLIM image of a stromal tissue region in the prostate imaged using the 40X/0.75NA objective. Optical anisotropy value calculated using the scattering phase theorem in this tissue region was g=0.932. **D)** Anisotropy calculation using Henyey-Greenstein phase function fit of the scattering angular distribution yields g=0.928.

Analysis of anisotropy in the stroma immediately adjoining the glands from 181 individuals who underwent prostatectomy (89 with recurrence after prostatectomy pair-matched with 89 without

recurrence; and 3 additional un-matched recurrent cases) are summarized in Fig. 4.4. The anisotropy values are displayed as a histogram with a bin width set at 0.01. The anisotropy value in the stromal layer immediately adjoining the glands was lower among patients with recurrence (0.911±0.039) than in patients who did not have recurrence of cancer after prostatectomy (0.935±0.031). This difference in anisotropy values is statistically significant (t-test, $p=7.66 \times 10^{-6}$). The accuracy of anisotropy measurement in the stroma was characterized using the Henyey-Greenstein fit, as shown in Fig. 4.4-C,D. The accuracy estimation is described in more detail in materials and methods.

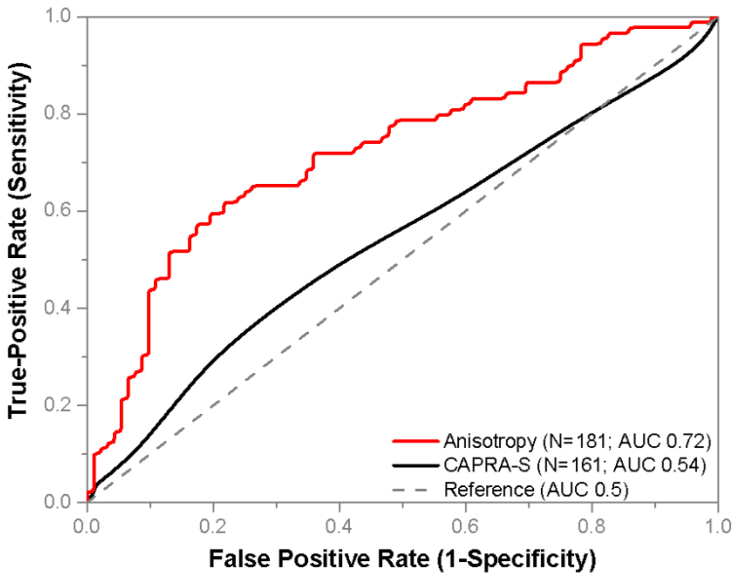

Figure 4.5: Results for Prostate Cancer Recurrence using Anisotropy of Scattering. Single layers of stroma immediately adjoining 12-16 glands were isolated in SLIM images from each of the 92 recurrent and 89 non-recurrent patients who underwent prostatectomy. The patients in the two groups were matched based on age at prostatectomy, Gleason grade and clinical stage. The optical anisotropy parameter was calculated for each region, as described in Materials and Methods. This parameter separates cases of recurrence from non-recurrent twins with an AUC of 0.72, as shown. Lower values of this index correspond to a greater probability of biochemical recurrence. By using a cut-off value of g=0.938, we can predict recurrence with a sensitivity of 77% and specificity of 62%. CAPRA-S scores corresponding to 161 patients, 83 recurrent and 78 non-recurrent, showed poor discrimination (AUC 0.54). Twenty cases were excluded in CAPRA-S analysis due to one or more missing parameters for CAPRA-S calculation.

Anisotropy (g) can be used to distinguish between recurrent and non-recurrent cases with an AUC of 0.72 as shown in Fig. 4.5. When the prediction threshold was set at g = 0.938, as determined from the ROC curve, recurrence could be predicted with a sensitivity of 77% and specificity of 62%. The threshold value, g=0.938, is not between the mean values of the two distribution due to the skewness in the g- distribution among the recurrent and non-recurrent groups. The threshold is in the region between the median value of the recurrent (0.921) and non-recurrent (0.945) groups. The CAPRA-S score (see Supplemental Information), which is commonly used as recurrence prediction tool in clinical practice, was calculated for 161 patients (83 recurrent, 78 non-recurrent) from the same set. Twenty subjects were not included in CAPRA-S analysis due to missing values for pre-surgical PSA level, extra-capsular extensions, and/or lymph node status. In those 161 patients, CAPRA-S distinguished between the two groups with an AUC of 0.54. This low performance of CAPRA-S is not surprising because some of the parameters used for CAPRA-S calculation, namely, Gleason score and lymph node status were pair-matched by design.

4.4 Effect of PSA on anisotropy as a recurrence predictor

Pre-surgical prostate specific antigen (PSA) level is one of the parameters used in CAPRA-S calculation and ranges from 0-3 out of the total possible CAPRA-S score of 0-12. This means the PSA level can have a significant impact on a patient's CAPRA-S score. The cases in our tissue microarray (TMA) cohort were not matched based on PSA levels and PSA showed poor correlation with anisotropy (Pearson r = -0.12). In order to study the effect of PSA on the

predictive ability of CAPRA-S score and anisotropy, we compared the performance of the two tools at the PSA ranges used in the CAPRA-S calculations as shown in Fig. 4.6.

At the PSA range of 0-6 ng/ml, the CAPRA-S parameter failed (AUC 0.4) on the 57 cases (31 recurrent, 26 non-recurrent), whereas anisotropy showed better performance (AUC 0.7). In the intermediate PSA range of 6.01-10 ng/ml and 10.01-20 ng/ml, both CAPRA-S and anisotropy were able to discriminate between recurrent and non-recurrent cases, but anisotropy showed significantly better performance. Anisotropy showed best performance in the PSA range of 10.01-20 ng/ml with an AUC of 0.88 in 36 cases (23 recurrent, 13 non-recurrent).

In the 18 cases where PSA levels were greater than 20 ng/ml, both CAPRA-S and anisotropy showed poor performance. Our data shows a decrease in anisotropy value in the stroma adjoining glands among all individuals with pre-surgical PSA levels greater than 20 ng/ml, irrespective of recurrence status. This decrease in anisotropy among non-recurrent individuals contributes to the low discrimination of our method. We believe that high PSA levels influence the morphology of stroma such that it causes increasing fractionation and non-uniform swelling of stromal fibers (illustrated in Fig 4.9 in the materials and methods section). Our observations are consistent with previous studies that have implicated PSA in regulating prostate stromal cell growth by modulating interactions with growth factors and cytokines [24, 25]. The reason CAPRA-S failed on cases with high PSA levels is that levels of PSA>20ng/ml corresponds to 3 CAPRA-S points out of the maximum 12. Hence it over-estimates the CAPRA-S score among individuals without recurrence but high pre-surgical PSA levels. Note that, CAPRA-S is expected to fail among non-recurrent patients with high PSA levels, as the patient pairs are matched in all other relevant parameters. In all PSA ranges, anisotropy performed better than

CAPRA-S and a higher value of anisotropy corresponded to a lower probability of biochemical recurrence of prostate cancer.

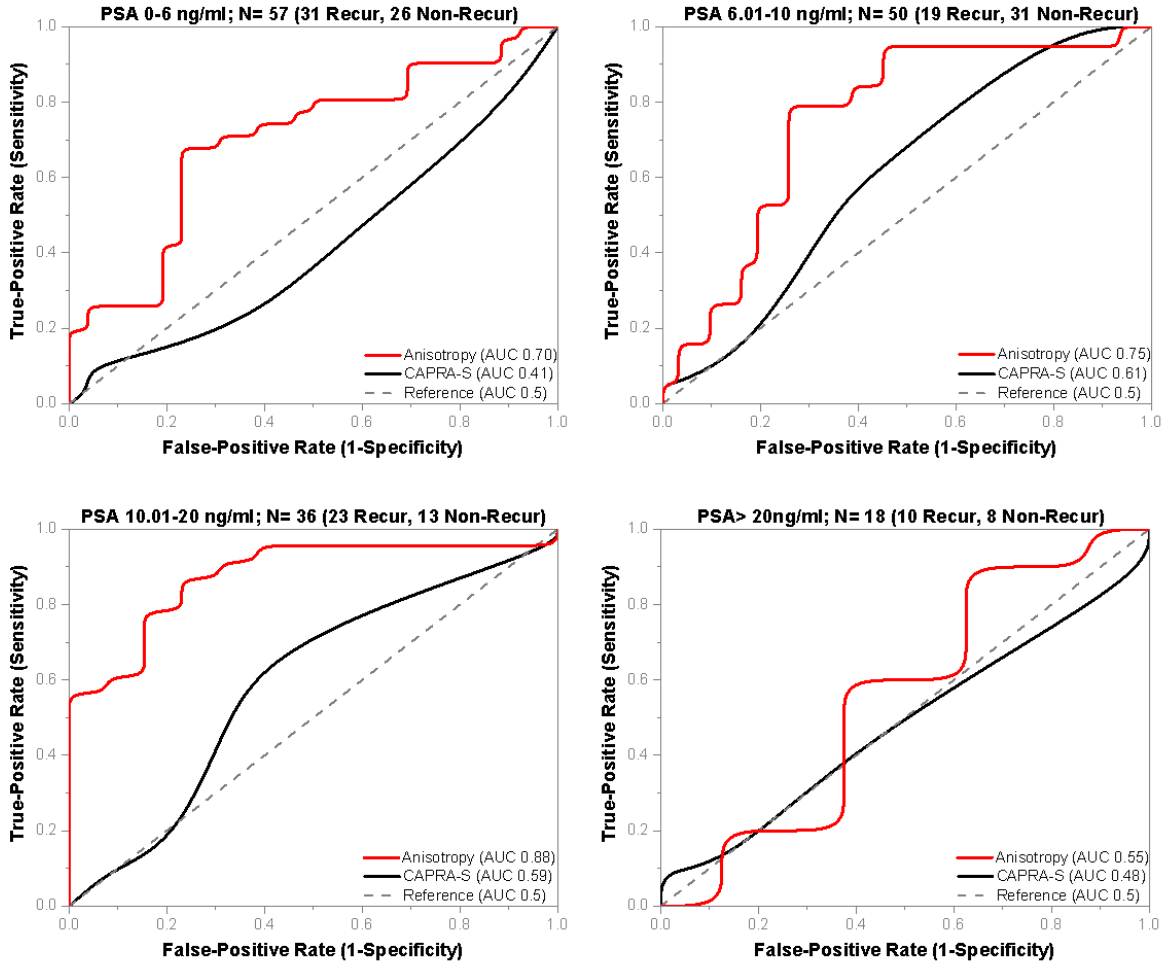

Figure 4.6: Influence of PSA on Anisotropy Values. Optical anisotropy (g), has poor correlation with pre-surgical PSA levels which prompted the prostate cancer diagnosis (Pearson r=-0.12). The performance of anisotropy and CAPRA-S is compared across various PSA ranges. A) At PSA 0-6 ng/ml, anisotropy (AUC 0.7) outperforms CAPRA-S (AUC 0.41), which failed on the 57 cases. B) At PSA 6.01-10ng/ml, CAPRA-S has the best results (AUC 0.61), but anisotropy (AUC 0.75) still shows better discrimination. C) At PSA 10.01-20 ng/ml, anisotropy (0.88) has the best performance among all the PSA ranges and performs better than CAPRA-S (0.59). D) At PSA>20ng/ml, both anisotropy (AUC 0.55) and CAPRA-S (AUC 0.48) show poor discrimination.

4.5 Discussion

It is rather interesting that recurrence is associated with lower g-values. In other words, more serious clinical states are correlated with tissue scattering that appears more isotropic. These findings suggest that the stroma around the recurrent glands is fragmented to smaller subunits than in their non-recurrent counterpart or that there is a loss of collagen fiber alignment in cases of worse outcome. Normal prostate stroma is composed of collagen fibers, smooth muscle cells and fibroblasts, unlike breast and ovarian stroma, which are not smooth muscle-rich [26]. This might also explain why collagen orientation results are markedly different in breast, ovarian and prostate cancers.

We believe that the changes in anisotropy of scattering detected by QPI are consistent with current understanding of prostate cancer biology. In order for cancer to metastasize, malignant epithelial cells breach the basement membrane and invade the stroma. This appears to explain why the changes we detected in stroma are directly adjoining the glands. Stromal invasion also triggers a wound healing process during which various growth factors are secreted and fibroblasts switch to myofibroblastic phenotype for wound closure [27-29]. The inability to successfully close the wound, which was associated with decreased α-smooth muscle actin and desmin expression has been correlated with shorter recurrence time [28]. Fibroblasts and myofibroblasts also continue secreting extra-cellular matrix components (ECM) and proteases for degradation of existing ECM. High levels of stromal protein cleavage factors matrix metalloproteinase (MMP) 2,9 and lower levels of tissue inhibitors of metalloproteinase (TIMP) 1,2 were associated with higher Gleason scores (8-10), higher probability of metastases and lower probability of cure [30, 31]. Molecular studies have shown the importance of the stroma in cancer aggressiveness. However, studying all molecular expression changes together would

involve multiple rounds of immunohistochemistry and other tests which are difficult to quantify or reproduce. On the other hand, QPI characterizes changes in the light scattering caused by morphological changes in the stroma, which are the final result of all the molecular changes associated with cancer progression. The increasingly fragmented appearance of stroma and the increased disorganization in cases with poor prognosis is measured as a decrease in optical anisotropy. Anisotropy shows significant promise in forecasting the recurrence of prostate cancer in individuals who undergo prostatectomy. By combining the label-free nature and nanoscale sensitivity of SLIM, we measure changes in optical scattering that are not measurable using conventional pathology techniques. The samples used in this paper represent cases in which the current widely accepted prognostic tool CAPRA-S fails at predicting the recurrence of prostate cancer. Further studies will determine whether anisotropy can be used to identify high-risk patients in other cohorts and from prostate biopsies, and thus distinguish patients who might benefit from active surveillance instead of prostatectomy.

4.6 Materials and Methods

4.6.1 Prostate tissue specimens. We used the National Cancer Institute Cooperative Prostate Cancer Tissue Resource (NCI-CPCTR) tissue microarray (TMA5), which provides both tissue and clinical data associated with patients who underwent radical prostatectomy for treatment of prostate cancer. The tissue was collected at four academic institutions: George Washington University, New York University, University of Pittsburg, and Medical College of Wisconsin. Procedures, policies and protocols for TMA construction and slide preparation are available at the CPCTR website [32, 33]. The studies have been performed in the United States in accordance with the procedure approved by the Institutional Review Board at University of Illinois at Urbana-Champaign (IRB Protocol Number: 13900).

4.6.2 TMA cohort. The outcomes TMA set (TMA5) includes pathologic material from 200 paired recurrence and non-recurrence prostate cancer cases (400 altogether). Measurement of prostate-specific antigen (PSA) levels in serum is the most commonly used diagnostic and tumor recurrence marker in prostate cancer. Increasing serum PSA concentrations is considered evidence of clinical recurrence after prostatectomy or radiation treatment. The CPCTR created a Perl-based algorithm to calculate post-treatment PSA outcomes results based on the initial PSA and multiple PSA values obtained after treatment. For the script, PSA recurrence was defined as a single PSA value of greater than 0.4 ng/ml, or a PSA value greater than 0.2 ng/ml with additional subsequent increasing values. Details of the algorithm can be found in this reference [34].

Each patient with biochemical recurrence of prostate cancer was matched by race, Gleason sum score (primary and secondary Gleason grades were also accounted), pTNM stage, and age at radical prostatectomy with a patient who did not show recurrence. All cases had no known metastasis, ≥5 years follow-up, a PSA nadir and at least 5 PSA tests after surgery. Cases were arrayed over five blocks with a single focus of tumor from each patient represented in quadruplicate 0.6 mm cores. Case-control pairs were allocated in the same block. The complete set of five blocks has 1,600 prostate tissue cores. For this study, two 4µm thick TMA tissue sections were cut from each block at the University of Illinois at Chicago. The thickness was set at 4µm in accordance with standard practice in pathology. One set was stained with Hematoxylin and Eosin (H&E) for pathology verification and also as a control. An adjacent set was submitted unstained to the Quantitative Light Imaging Laboratory, Urbana, Illinois, for SLIM imaging. This set of slides was subsequently de-paraffinized, cover slipped and imaged using the spatial

light interference microscope (SLIM). The demographics of the patients whose tissue was interrogated using SLIM is shown in Fig. 4.7.

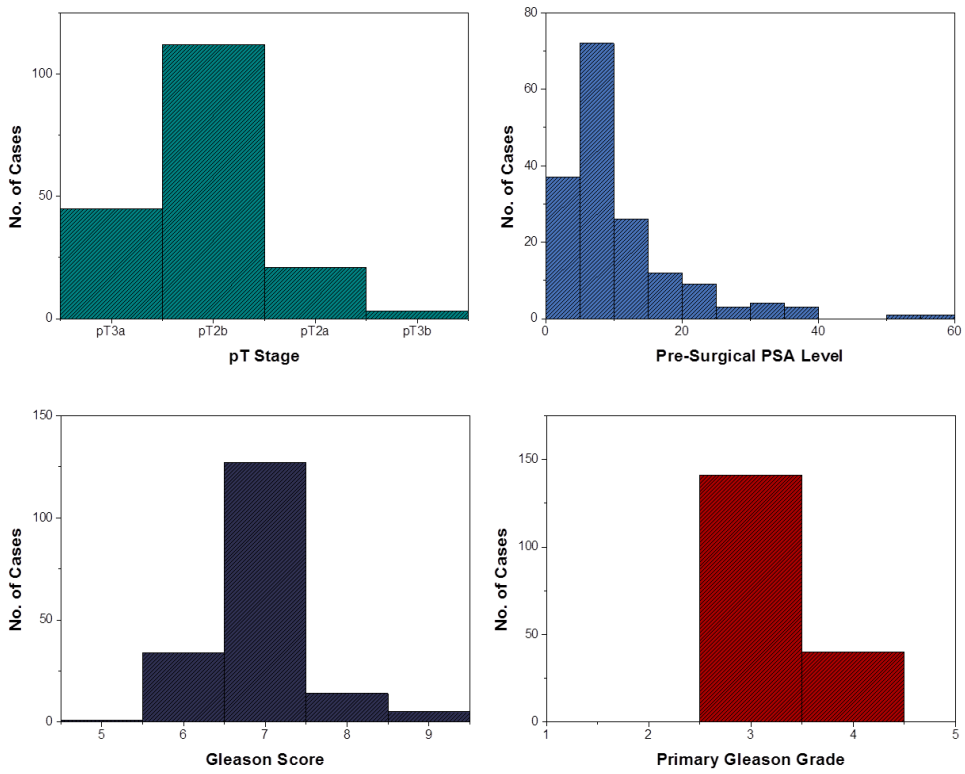

Figure 4.7: Patient Demographics. The histograms show the demographics associated with 181 prostatectomy cases used for our study based on various parameters such as the pT stage, pre-surgical PSA levels, Gleason score and primary Gleason grade.

4.6.3 Spatial Light Interference Microscopy (SLIM). SLIM is developed as an add-on module to an existing phase contrast microscope, as shown in Fig. 1A. The image field outputted by the microscope is Fourier transformed by the lens system L1, L2, L3 onto the surface of a spatial light modulator (SLM). The SLM shifts the phase of the unscattered light with respect to the scattered light, sequentially, in increments of $\pi/2$ (see Ref. [21]). Lens L4 recreates the image of the sample at the CCD, which records an image for each phase modulation. The four *intensity*

images are combined to uniquely render the quantitative *phase* map of the image field, as shown in Fig. 4.1B. The transverse resolution of SLIM images is 0.4 μm, limited by the numerical aperture of the objective and the spatial path length sensitivity is 0.3nm.

In order to image pathology slides, the SLIM imaging system was modified to mosaic together large fields of view necessary for diagnosis. The SLM switching, image acquisition, and stage scanning was synchronized via the computer and software developed in house. Before scanning, individual focus points were set at each frame of the mosaic to ensure the entire tissue is in focus. Post-processing code was written in MATLAB and ImageJ to stitch all the tiles of the mosaic together in order to obtain the final quantitative phase image of the tissue. The TMA slides were imaged via a 40X/0.75NA objective as illustrated in Fig. 4.2. The size of single field of view in the 40X SLIM system is approximately 99x74μm, corresponding to 1388x1040 pixels on the camera. The diameter of each tissue core was approximately 0.6 mm, so each core was imaged as a 10x10 mosaic which was cropped to 10,000x10,000 pixels for analysis. An example of the side-by-side comparison between SLIM images and H&E stained images is shown in Fig. 3. Note that the morphological details contained in the H&E image, e.g., glandular structure, cell nuclei and stromal fiber alignment are recovered in the SLIM image.

Stromal regions directly adjoining randomly selected 12-16 malignant glands per patient were selected for analysis. A Wacom tablet and the region of interest (ROI) feature on ImageJ were used to manually select the stromal ROIs as shown in Fig. 4A. The size of the ROI is subject to variation based on the size of the glands. Additionally, the width of stromal fibers can vary due to swelling. Individual stromal fibers and separation between adjacent fibers are clearly visible in SLIM images enabling accurate segmentation of the stromal fiber adjacent to the gland. For

each stromal region, we calculated the *optical anisotropy*, g, which is a measure of directionality of light scattered by tissue, as detailed below.

4.6.4 Optical Anisotropy Calculation. The anisotropy factor is the average cosine of the scattering angle, $g = \langle \cos(\theta) \rangle$. The *scattering-phase theorem [35] states that* the anisotropy factor can be computed from quantitative phase images as

$$g = 1 - \frac{1}{2k_0^2} \frac{\langle |\nabla[\varphi(r)]|^2 \rangle_r}{\langle \Delta\varphi^2(r) \rangle_r^2}, \qquad [1]$$

where $k_0 = 2\pi/\lambda_0$ is the wavenumber, λ_0=552nm is the center wavelength of white light used in our imaging, r is the stromal region over which optical anisotropy is calculated, $\langle \nabla[\varphi(r)] \rangle_r$ is the mean phase gradient intensity, and $\langle \Delta\varphi^2(r) \rangle_r$ is the phase variance. Eq. 1 is derived using the regular thin object approximation for QPI, which gives the expected phase shift proportional with thickness. However, g is a property of the tissue bulk, not of the particular slice. Therefore, as long as the out-of-focus light is negligible, i.e., the phase measurement integrates over the entire tissue thickness, g is independent of thickness.

Once the quantitative phase image of the core was available, a map of the gradient was computed using ImageJ. In our study, we calculated g in the stromal layer immediately adjoining the glands, as illustrated in Fig. 4.4-A. This stromal region was the region of interest, 'r', in equation (1). The mean phase gradient intensity and phase variance were computed in the stromal region of interest and finally the value of g was obtained.

Figure 4.8 illustrates the low- and high-values of g: more isotropic scattering corresponds to lower values of g. Our results indicate that bad outcomes are correlated to lower g-values.

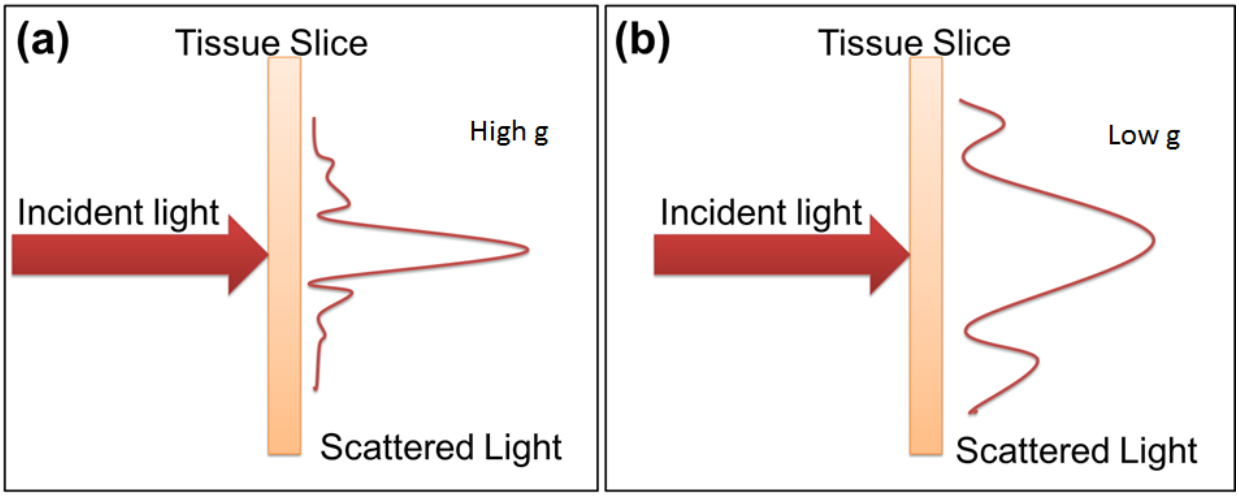

Figure 4.8: Optical Anisotropy. Optical anisotropy (g) is defined as the average cosine of the scattering angle in a single scattering event. Optical anisotropy is directly proportional to the square of the magnitude of phase gradient averaged over a tissue region and inversely proportional to the phase variance in the same region. **(a)** A tissue slice with high anisotropy is primarily forward scattering. **(b)** Tissue slide with low anisotropy scatters uniformly in all directions.

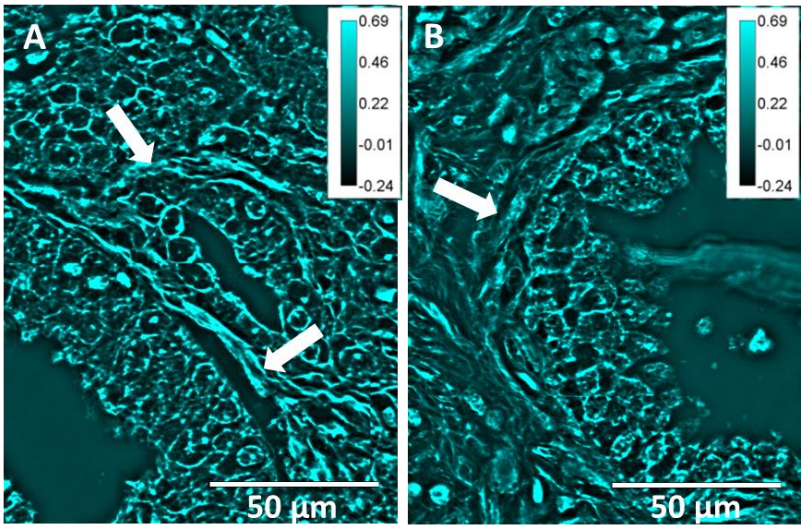

Figure 4.9: Effect of PSA on tissue morphology A) Prostatectomy tissue of patient with pre-surgical PSA level 30.1 ng/ml who did not have recurrence of prostate cancer. Stromal fiber thickness is uniform but has fractionated morphology. **B)** Prostatectomy tissue of unmatched patient with recurrence of prostate cancer who had pre-surgical PSA level 32 ng/ml. Stromal fiber thickness is non-uniform and has a more pronounced fragmented morphology. Arrows point to such fragmented filaments.

The morphology of stroma adjoining glands among patients with high PSA levels (PSA>20ng/ml), is fractionated and shows non-uniform swelling. This causes anisotropy to fail at identifying non-recurrent individuals with high pre-surgical PSA levels as illustrated in Figure 4.9.

We calculated the accuracy in the measurement of anisotropy retrieved from the scattering phase theorem by comparing it with g-values obtained from fitting the scattering angular distribution with the Henyey-Greenstein phase function. The Henyey-Greenstein distribution is [36]:

$$P(\theta) \propto \frac{1-g^2}{[1+g^2-2g\cos(\theta)]^{\frac{3}{2}}}.$$

The g-value obtained with the Henyey-Greenstein fit over the tissue region shown in Fig. 4C is g=0.928, with fit accuracy R^2=0.982 (Fig. 4D). The g-value over the same region calculated using the scattering phase theorem, is g=0.932.

For the purposes of prognosis and diagnosis, *precision* in the measurement of g is more critical than *accuracy*. In order to estimate the errors in our g calculations, we considered an area of background, with no tissue, and quantified the effect of the background phase noise upon the resulting g-values. Let us consider

$$g = 1 - \frac{1}{2k_0^2}\frac{f_1}{f_2},$$

where $f_1 = \langle|\nabla\phi(r)|^2\rangle_r$ is the average phase gradient intensity squared over a given tissue region and $f_2 = \langle\Delta\phi^2|r|\rangle_r^2$ is the phase variance squared over the tissue region.
The error in our measurement is given by

$$\Delta g = \left| \frac{1}{2k_0^2} \frac{f_1 \Delta f_2 - f_2 \Delta f_1}{f_2^2} \right|$$

where Δf_1 and Δf_2 are the standard deviations due to phase noise in f_1 and f_2, respectively. In order to evaluate Δf_1 and Δf_2, we selected a region of the SLIM image with no tissue, i.e., background, and computed the standard deviations of f_1 and f_2 due to noise. As a result, we obtained $\Delta g = 3.8e - 4$, which describes the error in our measurements due to spatial phase noise. This low value is the direct result of the absence of speckles in SLIM imaging due to the white light illumination.

4.6.5 CAPRA-S Score. The Cancer of the Prostate Risk Assessment (CAPRA-S) score is a commonly used post-radical prostatectomy prostate cancer recurrence risk assessment tool, which is described in detail elsewhere [7]. It assigns differential weightage to PSA levels before surgery, pathological Gleason score, extra-capsular extension, surgical margin status, seminal vesicle invasion and lymph node invasion. The weightages are added up to provide a score that determines the risk of biochemical recurrence of prostate cancer.

4.6.6 Receiver Operating Characteristic (ROC). The ROC curve plots the sensitivity (true positive rate) against 1-specificity (false positive rate). In order to plot an ROC curve using binary data, incremental cut-off or threshold values are set at which the true positive and false positive rates are determined and plotted. The area under the ROC curve (AUC) (this is equivalent to c-index in a binary outcome, however, c-index is calculated differently) represents the accuracy of the classification. An AUC of 1 corresponds to a perfect classification method whereas an AUC of 0.5 corresponds to random guess, like a coin toss.

4.6.7 D'Amico Risk Classification. The D'Amico risk classification is based on the combination of clinical parameters such as prostate specific antigen (PSA) levels measured in blood, Gleason score on the biopsy and prostate tumor size (T) as measured in either a digital rectal exam or trans-rectal ultrasound. There are three categories [37]:

1. D'Amico low risk category: Blood PSA level ≤ 10 ng/ml, Gleason score ≤ 6, T1-T2a. (T1: Tumor was an incidental finding that is not palpable; T2a: Tumor is in less than one half of one side of the prostate)

2. D'Amico intermediate risk classification: Blood PSA level of 10-20 ng/ml, Gleason score 7, T2b.

(T2b: Tumor is confined to one side of the prostate, but more than one half of one lobe)

3. D'Amico high risk classification: Blood PSA level > 20 ng/ml, Gleason score ≥ 8, T2c-T3a.

(T2c: Tumor is in both sides of the prostate; T3a: Tumor shows extra-capsular extension.

4.7 References

1. Howlader N, N.A., Krapcho M, Garshell J, Miller D, Altekruse SF, Kosary CL, Yu M, Ruhl J, Tatalovich Z,Mariotto A, Lewis DR, Chen HS, Feuer EJ, Cronin KA. *SEER Cancer Statistics Review, 1975-2011*. 2014 2012 [cited 2014 September, 10].
2. Wilt, T.J., et al., *Radical Prostatectomy versus Observation for Localized Prostate Cancer.* New England Journal of Medicine, 2012. **367**(3): p. 203-213.
3. Eggener, S.E., et al., *Predicting 15-year prostate cancer specific mortality after radical prostatectomy.* The Journal of urology, 2011. **185**(3): p. 869-75.
4. Stephenson, A.J., et al., *Prostate cancer-specific mortality after radical prostatectomy for patients treated in the prostate-specific antigen era.* Journal of clinical oncology : official journal of the American Society of Clinical Oncology, 2009. **27**(26): p. 4300-5.
5. Hull, G.W., et al., *Cancer control with radical prostatectomy alone in 1,000 consecutive patients.* The Journal of urology, 2002. **167**(2 Pt 1): p. 528-34.
6. Stephenson, A.J., et al., *Postoperative nomogram predicting the 10-year probability of prostate cancer recurrence after radical prostatectomy.* Journal of clinical oncology : official journal of the American Society of Clinical Oncology, 2005. **23**(28): p. 7005-12.
7. Cooperberg, M.R., J.F. Hilton, and P.R. Carroll, *The CAPRA-S score: A straightforward tool for improved prediction of outcomes after radical prostatectomy.* Cancer, 2011. **117**(22): p. 5039-46.
8. Sergeev, A., et al., *In vivo endoscopic OCT imaging of precancerand cancer states of human mucosa.* Opt. Express, 1997. **1**(13): p. 432-440.
9. Bouma, B.E., et al., *High-resolution imaging of the human esophagus and stomach in vivo using optical coherence tomography.* Gastrointestinal Endoscopy, 2000. **51**(4): p. 467-474.
10. Sivak Jr, M.V., et al., *High-resolution endoscopic imaging of the GI tract using optical coherence tomography.* Gastrointestinal Endoscopy, 2000. **51**(4): p. 474-479.
11. Escobar, P.F., et al., *Diagnostic efficacy of optical coherence tomography in the management of preinvasive and invasive cancer of uterine cervix and vulva.* International Journal of Gynecological Cancer, 2004. **14**(3): p. 470-474.
12. Pan, Y.T., et al., *Enhancing early bladder cancer detection with fluorescence-guided endoscopic optical coherent tomography.* Opt. Lett., 2003. **28**(24): p. 2485-2487.
13. Mogensen, M., et al., *OCT imaging of skin cancer and other dermatological diseases.* Journal of Biophotonics, 2009. **2**(6-7): p. 442-451.
14. Nguyen, F.T., et al., *Intraoperative evaluation of breast tumor margins with optical coherence tomography.* Cancer Research, 2009. **69**(22): p. 8790-8796.
15. Radosevich, A.J., et al., *Ultrastructural alterations in field carcinogenesis measured by enhanced backscattering spectroscopy.* J Biomed Opt, 2013. **18**(9): p. 097002.
16. Subramanian, H., et al., *Partial-wave microscopic spectroscopy detects subwavelength refractive index fluctuations: an application to cancer diagnosis.* Opt Lett, 2009. **34**(4): p. 518-20.
17. Chung, L.K., *Fibroblasts are critical determinants in prostatic cancer growth and dissemination.* Cancer and Metastasis Reviews, 1991. **10**(3): p. 263-274.
18. Ambekar, R., et al., *Quantifying collagen structure in breast biopsies using second-harmonic generation imaging.* Biomed Opt Express, 2012. **3**(9): p. 2021-35.
19. Nadiarnykh, O., et al., *Alterations of the extracellular matrix in ovarian cancer studied by Second Harmonic Generation imaging microscopy.* BMC Cancer, 2010. **10**: p. 94.

20. Conklin, M.W., et al., *Aligned collagen is a prognostic signature for survival in human breast carcinoma.* Am J Pathol, 2011. **178**(3): p. 1221-32.
21. Wang, Z., et al., *Tissue refractive index as marker of disease.* J Biomed Opt, 2011. **16**(11): p. 116017.
22. Kim, T., et al., *White-light diffraction tomography of unlabeled live cells.* Nat Photon, 2014. **8**.
23. Popescu, G., *Quantitative phase imaging of cells and tissues*. McGraw-Hill biophotonics. 2011, New York: McGraw-Hill. 385.
24. Sutkowski, D.M., et al., *Growth regulation of prostatic stromal cells by prostate-specific antigen.* J Natl Cancer Inst, 1999. **91**(19): p. 1663-9.
25. Williams, S.A., et al., *Does PSA play a role as a promoting agent during the initiation and/or progression of prostate cancer?* The Prostate, 2007. **67**(3): p. 312-329.
26. Rowley, D., *What Might A Stromal Response Mean to Prostate Cancer Progression?* Cancer and Metastasis Reviews, 1998. **17**(4): p. 411-419.
27. Tuxhorn, J.A., G.E. Ayala, and D.R. Rowley, *REACTIVE STROMA IN PROSTATE CANCER PROGRESSION.* The Journal of Urology, 2001. **166**(6): p. 2472-2483.
28. Ayala, G., et al., *Reactive Stroma as a Predictor of Biochemical-Free Recurrence in Prostate Cancer.* Clinical Cancer Research, 2003. **9**(13): p. 4792-4801.
29. Tuxhorn, J.A., et al., *Reactive Stroma in Human Prostate Cancer: Induction of Myofibroblast Phenotype and Extracellular Matrix Remodeling.* Clinical Cancer Research, 2002. **8**(9): p. 2912-2923.
30. Jung, K., et al., *Quantification of matrix metalloproteinases and tissue inhibitors of metalloproteinase in prostatic tissue: analytical aspects.* Prostate, 1998. **34**(2): p. 130-6.
31. Wood, M., et al., *In situ hybridization studies of metalloproteinases 2 and 9 and TIMP-1 and TIMP-2 expression in human prostate cancer.* Clin Exp Metastasis, 1997. **15**(3): p. 246-58.
32. Berman, J.J., et al., *The tissue microarray data exchange specification: implementation by the Cooperative Prostate Cancer Tissue Resource.* BMC Bioinformatics, 2004. **5**: p. 19.
33. Kajdacsy-Balla, A., et al., *Practical aspects of planning, building, and interpreting tissue microarrays: the Cooperative Prostate Cancer Tissue Resource experience.* J Mol Histol, 2007. **38**(2): p. 113-21.
34. Liao, Z. and M.W. Datta, *A simple computer program for calculating PSA recurrence in prostate cancer patients.* BMC Urol, 2004. **4**: p. 8.
35. Ding, H., et al., *Measuring the scattering parameters of tissues from quantitative phase imaging of thin slices.* Optics Letters, 2011. **36**: p. 2281.
36. Henyey, L.G. and J.L. Greenstein, *Diffuse radiation in the Galaxy.* Astrophysical Journal, 1941. **93**: p. 70-83.
37. D'Amico, A.V., et al., *Biochemical outcome after radical prostatectomy, external beam radiation therapy, or interstitial radiation therapy for clinically localized prostate cancer.* JAMA, 1998. **280**(11): p. 969-74.

CHAPTER 05: Post-Prostatectomy Prediction of Prostate Cancer Recurrence – External Validation in a General Population of Patients

5.1 Abstract

Prediction of biochemical recurrence risk of prostate cancer following radical prostatectomy is critical for determining the need of adjuvant treatment options for the patient. Various nomograms exist today for identifying the individuals at higher risk for recurrence; however, an optimistic under-estimation of recurrence risk is a common problem associated with these methods. We previously showed that anisotropy of light scattering measured using quantitative phase imaging, in the stromal layer adjacent to cancerous glands, is predictive of recurrence. That nested-case controlled study consisted of specimens specifically chosen such that the current prognostic methods fail. Here we report on validating the utility of optical anisotropy for predicting prostate cancer recurrence in a general population of 192 patients, with 17% probability of recurrence. Our results show that our method can identify recurrent cases with 73% sensitivity and 72% specificity, which is comparable to that of CAPRA-S, a current state of the art method, in the same population. However, the results show that, while CAPRA-S performs better than our technique at low Gleason scores (5-6), it underperforms our method for patients with Gleason scores 7 – 10. Essentially, this means that CAPRA-S is better at identifying nonrecurring cases, while our scattering anisotropy marker performs better in selecting the recurring cases.

5.2 Motivation

In 2010, 138,000 men in the USA underwent radical prostatectomy for treatment of prostate cancer [1]. Biochemical recurrence or increase in serum prostate specific antigen (PSA) levels after prostatectomy is an early sign of prostate cancer recurrence. 17-33% of patients who undergo radical prostatectomy as primary form of treatment experience a biochemical recurrence of prostate cancer and 29-34% of individuals in that cohort will have metastatic prostate cancer with bone as the most common site of metastasis [2-6]. The 5-year survival rate for metastatic prostate cancer is 25% - 43% [3, 7]. Identification of individuals at high risk for biochemical recurrence will enable early adjuvant treatment for those patients, and thus reduce the risk for metastatic disease and prostate cancer-specific mortality.

Various methods based on pre and post-surgical evaluation of prostate tissue and clinical parameters have been developed for prediction of biochemical recurrence and these techniques have been reviewed elsewhere [8, 9]. The post-prostatectomy biochemical recurrence prediction methods which are most widely reported and validated are the Stephenson nomogram and CAPRA-S which have concordance index values reported between 0.72 - 0.77 [9, 10]. Optimistic prediction of non-recurrence is a problem that has previously been noted in both methods, despite the high discrimination accuracy [9, 11]. Additionally, these methods can lead to erroneous results as they rely on PSA levels and Gleason score reports which are prone to errors from assay sensitivity and inter-observer variability respectively [12].

Recently, biomarker-based approaches have been developed as both stand-alone predictors of prostate cancer recurrence and in combination with nomogram-based approaches [13-19]. The combination of those biomarkers with existing nomograms resulted in improved performance, but they are still subject to the problems associated with nomograms. We previously demonstrated the utility of anisotropy of light scattering in the stromal layer adjacent

to cancerous gland, measured using quantitative phase imaging (QPI) [20], as an independent biomarker for prediction of biochemical recurrence [19]. The study was conducted in a nested case control population where recurrent cases were matched with non-recurrent cases based on age, pTNM stage, primary and secondary Gleason score. We demonstrated that anisotropy had the ability to identify recurrence with 77% sensitivity and 62% specificity, while CAPRA-S showed poor discriminatory ability as multiple CAPRA-S parameters were used as matching criterion.

In this study, we present an external validation of optical anisotropy as a biomarker for prostate cancer recurrence. The patient population in this study had a recurrence probability of 17% which is representative of a general population. The aim of this work was to identify specific conditions where using anisotropy as a recurrence predictor had added value over currently used prognostic tools. We performed this study by first testing the performance of anisotropy as a recurrence predictor, and then comparing the performance of anisotropy with CAPRA-S across the low, intermediate, and high risk CAPRA-S groups and finally, comparing the performance of anisotropy with CAPRA-S across Gleason scores 5-6, 7 (3+4), 7 (4+3), 8-10. Our results showed that anisotropy has added value over CAPRA-S at Gleason score ≥ 7; and at CAPRA-S ≥ 3 which corresponds to the intermediate and high risk groups.

5.3 Anisotropy as a predictor of biochemical recurrence

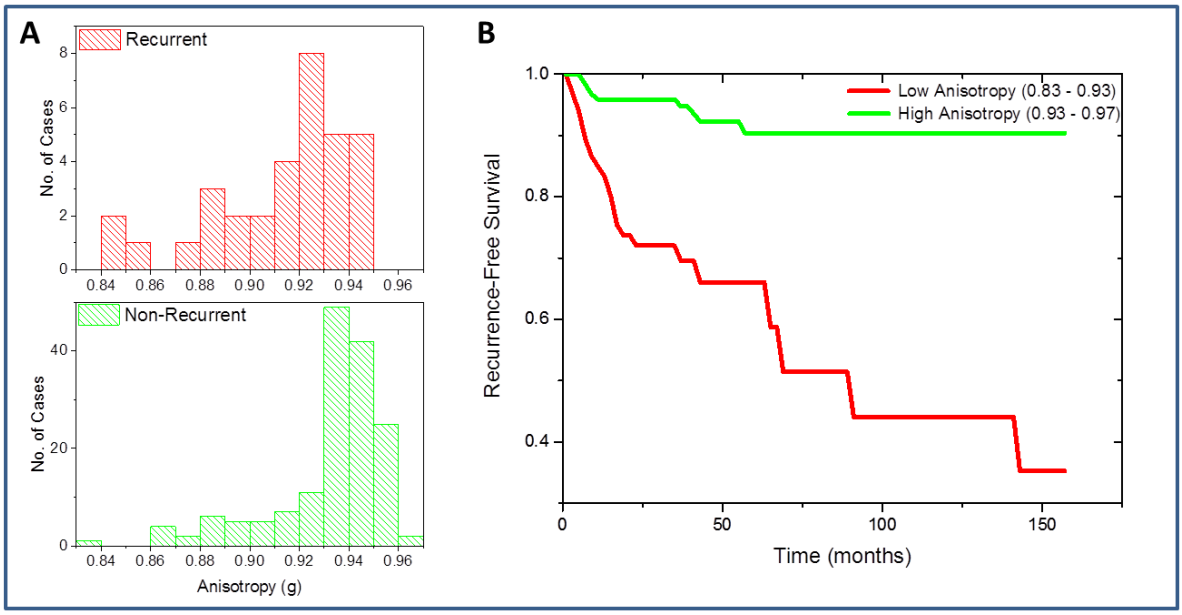

Figure 5.1: Optical anisotropy as a predictor of prostate cancer recurrence. (A) Histograms of the distribution of anisotropy in the single layer of stroma surrounding 6-18 glands from 33 patients with post-prostatectomy biochemical recurrence of prostate cancer and 159 non-recurrent patients. The bin-size on the histogram was set at 0.02. The anisotropy value is lower in the recurrent patients, compared to the non-recurrent patients (One-way ANOVA, $p= 7.05 \times 10^{-5}$) **(B)** Kaplan-Meier survival curve with end-point as disease recurrence for 67 patients with low anisotropy values (0.83 - 0.93) and 125 patients with high anisotropy values (0.93 – 0.97).

Anisotropy (g) of light scattering was measured using the scattering phase theorem in the unstained prostatectomy samples imaged using spatial light interference microscopy (SLIM), a QPI method (see Materials and Methods for details) [21, 22]. Anisotropy was calculated in the single stromal layer adjoining 6-18 glands from each of the 33 patients with post-prostatectomy biochemical recurrence of prostate cancer and 159 patients who did not have recurrence. The calibrated anisotropy value in the recurrent cases (0.913±0.028; median = 0.92) was lower than that in the non-recurrent cases (0.932±0.023; median = 0.938) (See Appendix A for details about calibration). The difference in anisotropy values in the cancer-adjacent stroma from the recurrent and non-recurrent groups was statistically significant (one-way ANOVA, $p = 7.05 \times 10^{-5}$). These results are summarized in Fig 5.1-A. A Kaplan-Meier survival analysis was performed

to test the utility of anisotropy for predicting biochemical recurrence as the end-point. The anisotropy ranges tested were 0.68 - 0.93 (67 patients) and 0.93 – 0.97 (125 patients) and the results, which are summarized in Fig 5.1-B, show that patients with low anisotropy values had a higher likelihood of disease progression. The 3-year and 5-year recurrence-free probability dropped from 95% and 90% respectively for patients with high anisotropy values to 70% and 65% respectively for patients with low anisotropy values.

5.4 Comparison of anisotropy, pre-surgical PSA level, Gleason score and CAPRA-S as recurrence predictors

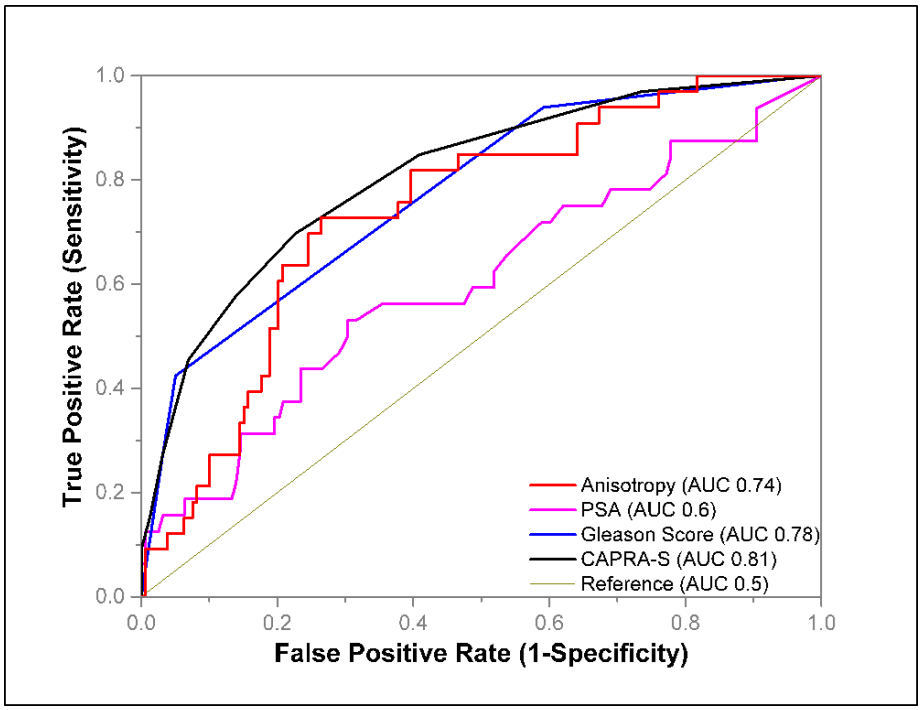

Figure 5.2: Comparison of recurrence prediction metrics. The performance of anisotropy measured on quantitative phase images, pre-surgical prostate-specific antigen (PSA) levels, Gleason score and CAPRA-S as post-prostatectomy biochemical recurrence predictors was studied in 192 prostatectomy cases (33 recurrent, 159 non-recurrent). The best performance was observed with CAPRA-S (AUC 0.81) and Gleason scores (AUC 0.78). The discriminatory ability of anisotropy (AUC 0.74) was lower than that of CAPRA-S and Gleason score. However, at the optimal performance point, anisotropy had a sensitivity of 72.7% and specificity of 73.6% compared to the 69.6% sensitivity and 77.4% specificity. Pre-surgical PSA level (AUC 0.6) was a poor predictor of recurrence.

We compared the ability of anisotropy to distinguish between recurrent and non-recurrent cases using the receiver-operating curve analysis as shown in Fig 5.2. Anisotropy had an area under the curve (AUC) of 0.74 (95% CI 0.64 – 0.84) and at a cut-off value of g = 0.93, recurrence was predicted with a sensitivity of 73% and a specificity of 73%. Pre-surgical PSA, with an AUC of 0.6 (95% CI 0.5 - 0.7) was not a good predictor of post-prostatectomy biochemical recurrence. In this cohort of patients, representative of a general population, both Gleason score and CAPRA-S out-performed anisotropy as a recurrence predictor. Gleason score with an AUC of 0.78 (95% CI 0.69 - 0.86) and CAPRA-S with an AUC of 0.81 (95% CI 0.73 – 0.89) showed comparable predictive ability. At the cut-off value of Gleason score = 6.5, the sensitivity and specificity of recurrence prediction was 93.9% and 41% respectively; and at a cut-off value of Gleason score = 7.5, the sensitivity and specificity of recurrence prediction was 42% and 95% respectively. This steep gradient is reflective of Gleason score 7 being disease with diverse prognosis. For CAPRA-S, the optimal cut-off value for recurrence prediction was CAPRA-S = 2.5, resulting in a sensitivity of 69% and specificity of 77%. The optimal performance of CAPRA-S and anisotropy in identifying recurrence in a general population is comparable, with anisotropy more sensitive and CAPRA-S more specific.

5.5 Anisotropy as predictor of recurrence at various CAPRA-S ranges

CAPRA-S has high specificity in recurrence prediction and anisotropy has higher sensitivity. So we compared the performance of anisotropy as a recurrence predictor at the low, intermediate and high risk CAPRA-S ranges as defined previously [11]. At low CAPRA-S risk range of 0-2 CAPRA-S points, the probability of recurrence was 7.5% in 133 patients in the study. Anisotropy could identify recurrence with 70% sensitivity and 75% specificity (AUC 0.66, Fig 5.3-A). At intermediate CAPRA-S risk range of 3-5 CAPRA-S points, the probability of recurrence was 31.1% in 45 patients. Using anisotropy, recurrent patients could be identified

with 71% sensitivity and 65% specificity (AUC 0.79) (Fig 5.3-B). 14 patients in our study had high risk CAPRA-S scores of 6-11 and the probability of recurrence was 64.3%. Anisotropy could identify recurrence in this group with 78% sensitivity and 80% specificity (AUC 0.71) (Fig 5.3-C).

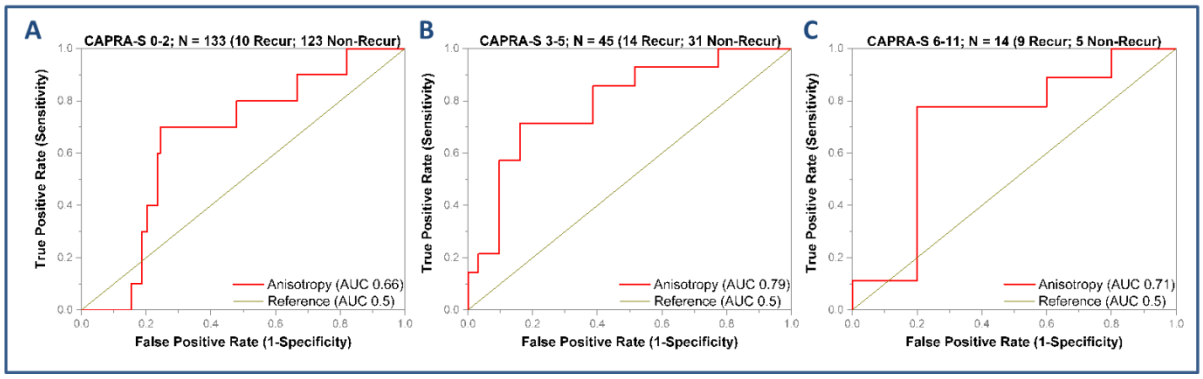

Figure 5.3: Performance of Anisotropy as a recurrence predictor. The performance of anisotropy as a recurrence predictor was compared across the low (0-2), intermediate (3-5) and high (6-11) CAPRA-S ranges. **(A)** At the low CAPRA-S range, the probability of recurrence was 7.5% and anisotropy (AUC 0.66) predicted recurrence with 70% sensitivity and 75% specificity. **(B)** At the intermediate CAPRA-S range, the probability of recurrence was 31.1%. Anisotropy (AUC 0.79) identified recurrence with 71% sensitivity and 65% specificity. **(C)** At the high CAPRA-S range, the probability of recurrence was 64.3% and anisotropy (AUC 0.71) identified recurrence with 78% sensitivity and 80% specificity.

5.6 Effect of Gleason score on anisotropy and CAPRA-S as recurrence predictors

Gleason score is an important component of CAPRA-S, with 0-3 points out of the total possible 0-11 CAPRA-S points coming from the Gleason grades. The observation that the overall performance of CAPRA-S and Gleason score in our cohort was comparable, led us to study the performance of anisotropy and CAPRA-S at various Gleason score ranges to determine added value. These results are summarized in Fig 5.4 and Table 5.1. In Fig 4, we show the results from the AUC analysis comparing CAPRA-S and anisotropy at the Gleason score ranges 5-6; 7 (3+4), 7 (4+3) and 8-10.

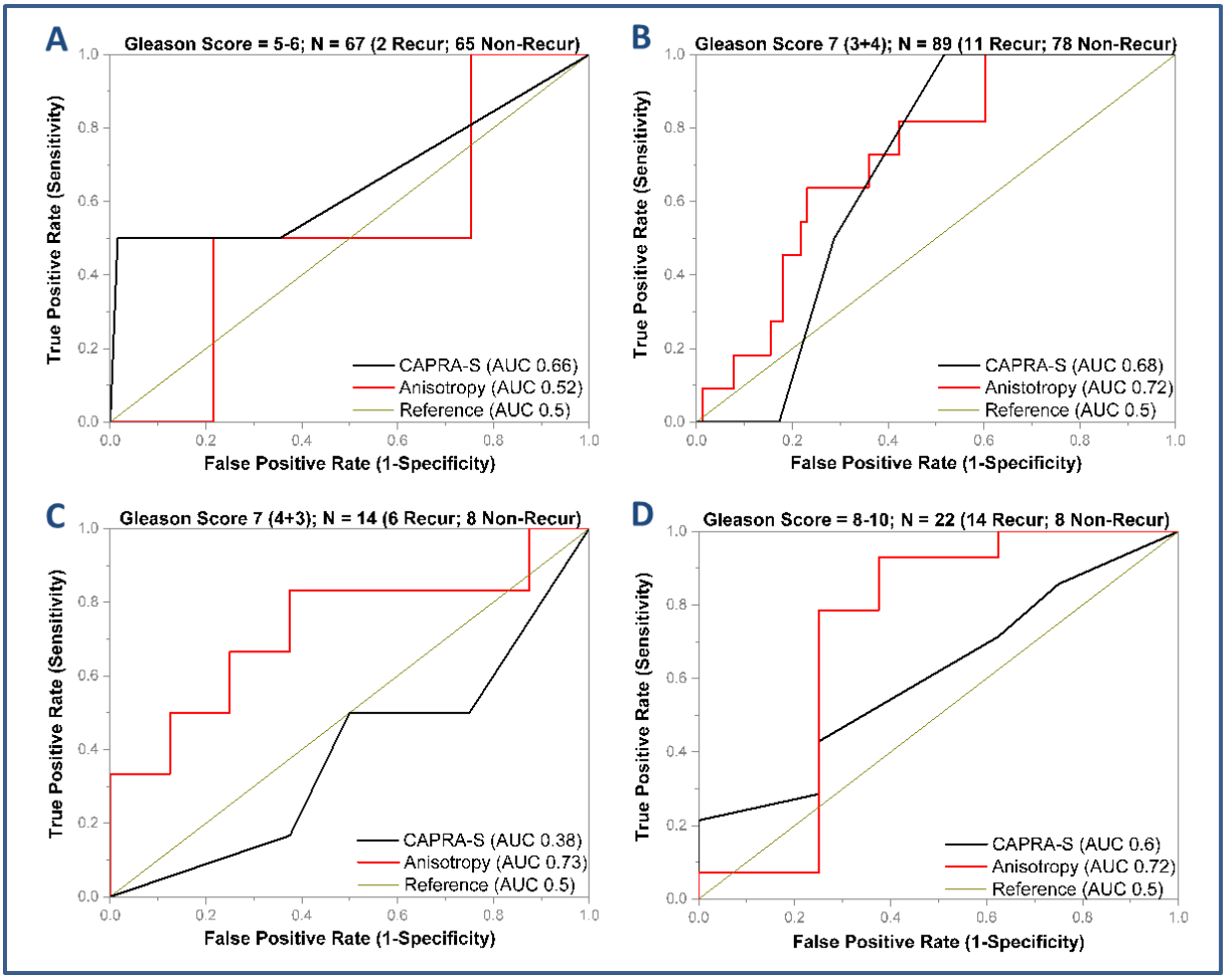

Figure 5.4: Gleason-score adjusted performance of Anisotropy and CAPRA-S. (A) At Gleason scores of 5-6, both anisotropy and CAPRA-S show poor performance at identification of recurrent individuals. However, the probability of recurrence at this stage is 3% and CAPRA-S outperforms anisotropy due to it's ability to identify 100% of the non-recurrent cases. **(B)** At Gleason score of 7 (3+4), anisotropy (AUC 0.72) and CAPRA-S (AUC 0.68) show comparable performance. The probability of recurrence at this stage was 16%. **(C)** At Gleason score of 7 (4+3), the probability of recurrence is 43%. CAPRA-S (AUC 0.38) failed due to overestimation of the recurrence risk. Anisotropy was able to identify recurrence (AUC 0.73). **(D)** At Gleason score of 8-10, the probability of recurrence is 64%. Anisotropy (AUC 0.73) was able to identify the recurrent cases with a higher level of accuracy than CAPRA-S (AUC 0.6).

At Gleason score 5-6, the probability of recurrence was 2.98% among the 67 patients and all cases had CAPRA-S scores in the low and intermediate range (Fig 4A, Table 1). At this Gleason range, anisotropy over-estimated the probability of recurrence. While only 1.5% and 50% of patients with low and intermediate CAPRA-S scores, respectively, had a recurrence,

CAPRA-S did not provide added value over Gleason score. At Gleason score 7 (3+4), anisotropy (AUC 0.72) had better discrimination ability than CAPRA-S (AUC 0.68) (Fig 5.4B). For the 89 patients in our study with Gleason score 7 (3+4), 70.8% patients had low CAPRA-S scores, 27% had intermediate CAPRA-S scores and 2.2% patients had high CAPRA-S scores; 29.2% had low anisotropy values and 70.8% had high anisotropy values (Table 5.1). While both patients with high CAPRA-S scores had a recurrence, 9.5% patients with low CAPRA-S and 12.5% with intermediate CAPRA-S scores also experienced recurrence. The probability of recurrence among patients with low and high anisotropy values was 26.9% and 6.3% respectively. Anisotropy, thus had a 63.6% sensitivity and 76% specificity for identifying recurrence at Gleason score 7 (3+4) and demonstrated added value over both Gleason score and CAPRA-S.

For the 14 patients with Gleason score 7 (4+3), the probability of recurrence was 42.85%. 57.1% patients had low anisotropy values and 42.9% patients had high anisotropy values, whereas, 35.7% patients were classified into the low and intermediate risk categories of CAPRA-S and 28.6% patients were classified into the high risk category of CAPRA-S (Table 5.1). However, the CAPRA-S grouping and recurrence rates showed an inverse relationship, and therefore CAPRA-S showed poor discrimination in Gleason 7 (4+3) patients (AUC 0.38) (Fig 5.4C). 62.5% of patients with low anisotropy values had recurrence and 83.3% of patients with high anisotropy did not have a biochemical recurrence. Anisotropy shows the ability to predict recurrence with 83.3% sensitivity and 62.5% specificity (AUC 0.73) and thus outperforms CAPRA-S in the patients with Gleason score 7 (4+3).

	Recurrence (No. of Cases)	Anisotropy	Recurrence (No. of Cases)	CAPRA-S	Recurrence (No. of Cases)
Gleason Score 5-6	2.98% (67)	Low	5.2% (19)	0-2	1.5% (65)
				3-5	50% (2)
		High	2.1% (48)	6-11	--
Gleason Score 3+4	12.35% (89)	Low	26.9% (26)	0-2	9.5% (63)
				3-5	12.5% (24)
		High	6.3% (63)	6-11	100% (2)
Gleason Score 4+3	42.85% (14)	Low	62.5% (8)	0-2	60% (5)
				3-5	40% (5)
		High	16.7% (6)	6-11	25% (4)
Gleason Score 8-10	63.63% (22)	Low	81.25% (16)	0-2	--
				3-5	57.1% (14)
		High	16.7% (6)	6-11	75% (8)

Table 5.1: Recurrence prediction across Gleason scores. The above table shows the percentage of cases with recurrence and the total number of cases in each sub-category according to stacked Gleason grade and anisotropy or stacked Gleason grade and CAPRA-S score.

Our study had 22 patients with Gleason score 8-10 and the probability of recurrence in this cohort was 63.3%. 72.7% of the patients had low anisotropy values and 27.3% of the patients had high anisotropy values (Table 5.1). There were no patients in the CAPRA-S low risk category since Gleason score 8-10 corresponds to 3 CAPRA-S points [9]. 63.6% and 36.4% patients were in the CAPRA-S intermediate and high risk categories. While the probability of recurrence linearly scales within the CAPRA-S ranges from 57.1% to 75%, the sensitivity of recurrence prediction was low (AUC 0.6, Fig 5.4D). 81.3% of the patients with low anisotropy values had recurrence and 83.3% of the patients with high anisotropy values did not experience a biochemical recurrence. The overall sensitivity and specificity of anisotropy as a recurrence

predictor in this cohort was 92.8% sensitivity and 62.5% specificity (AUC 0.73) and thus shows better discrimination than CAPRA-S in patients with Gleason score 8-10.

5.7 Discussion

Our results show that a lower value of optical anisotropy in the stromal layer immediately adjoining cancerous glands, which is indicative of a more fractionated stromal morphology, is a strong predictor of prostate cancer recurrence, and therefore poor prognosis. Interestingly, these predictive changes in stromal morphology are more pronounced at advanced stages of disease progression, that is, Gleason ≥7, as opposed to Gleason score 5-6. This suggests that stromal disorganization is a critical requirement for disease progression at advanced disease states. The probability of post-prostatectomy disease recurrence is small at Gleason score 5-6. At this Gleason range, very high sensitivity combined with very high specificity is necessary for identifying recurrence. CAPRA-S has high accuracy at predicting non-recurrence at this disease stage, and therefore outperforms anisotropy.

However, at Gleason 7, the probability of recurrence varies based on the primary and secondary pattern. The 5-year recurrence rate for Gleason 3+4 and Gleason 4+3 has been reported to be 14.6 - 29% and 33.3 – 38.9% respectively [23-26]. It is very important to have a prognostic method with high sensitivity at this Gleason range to prevent under-treatment. Anisotropy is a strong recurrence predictor at this Gleason range as evidenced by our previous study and the current validation study. At Gleason score 8-10, the probability of recurrence is 63.6% and current tools have the propensity for over-estimating recurrence and this can lead to over-treatment. For recurrence prediction at Gleason 8 – 10, anisotropy has both high sensitivity and high specificity. CAPRA-S showed poor discrimination for recurrence prediction at the Gleason range ≥7 and this could be due to the low number of patients having Gleason >6 in the CaPSURE database, which was used to construct CAPRA-S, [9, 11].

Based on our results, we conclude that anisotropy has to potential to improve treatment decisions for patients diagnosed with prostate cancer of Gleason grades 7 – 10. Since our technique relies solely on parameters measured in prostate tissue, anisotropy measurements show potential as a prognostic predictor for use in biopsies.

5.8 Materials and Methods

5.8.1 Prostate Tissue Specimen

We obtained the 217 case biochemical recurrence tissue microarray (TMA) set from the Prostate Cancer Biorepository Network (PCBN). The TMA set has prostatectomy tissue and clinical data associated with patients who were treated for prostate cancer with radical prostatectomy at New York University and Johns Hopkins University. The studies have been performed in accordance with the protocols approved by the Institutional Review Board at the University of Illinois at Urbana-Champaign (IRB Protocol Number: 13900).

5.8.2 TMA Cohort

The TMA set had prostatectomy tissue from 217 patients with 23 cases of adjacent normal tissue and 13 cases of benign prostatic hyperplasia (BPH). 38 patients had a biochemical recurrence of prostate cancer and 164 patients did not have a biochemical recurrence. There were 4-5 cores per patient and the cores were arrayed across 5 blocks. 192 cases were analyzed in this study and information regarding the patients' clinical parameters is shown in Table 5.2.

VARIABLE	No. of Cases
No. of Patients	192
Recurrent	33
Non-Recurrent	159
Race	
Caucasian	166
African-American	4
Asian	6
Other	8
Unknown	8
Patient Age at Prostatectomy (yrs)	
Median Age (range)	60.5 (41.8 - 77.2)
Pre-operative PSA (ng/ml)	
Median (range)	5.6 (0.0 - 29.0)
Pathologic Gleason score	
5-6	67
7 (3+4)	89
7 (4+3)	14
8-10	22
Extraprostatic Extension	
Positive	3
Negative	189
Seminal Vesicle Invasion	
Positive	14
Negative	178
Surgical Margins	
Positive	33
Negative	159
Mean Follow-up time (months)	
Follow-up Time (range)	59 (2 – 180)
PSA Follow-up Time (range)	48 (2 – 175)

Table 5.2: Characteristics of TMA Cohort. This table provides information regarding the total number of patients in the TMA set within each clinical category.

TMA tissue sections were cut from each of the 5 blocks at New York University. The sectioning thickness was 4μm, which is standard pathology practice. The tissue was de-paraffinized and the unstained tissue slide was cover-slipped with aqueous mounting medium at the pathology laboratory at the University of Illinois at Chicago. The slides were then imaged at the Quantitative Light Imaging Laboratory in Urbana, Illinois using the spatial light interference microscope (SLIM), which is a QPI technique described below.

5.8.3 Spatial Light Interference Microscopy

The Spatial Light Interference Microscopy (SLIM) system is an add-on module to a phase contrast microscope and is reviewed in detail elsewhere [21]. We used the commercial SLIM system (Cell Visa Q100, Phi Optics, Inc.) combined with imaging software developed in house, which synchronizes SLM switching, stage scanning and image acquisition. The TMA slides were imaged using the 40X/0.75NA objective and the size of each field of view, which can be controlled, was set at 85.16 x 82.6 μm corresponding to 528 x 512 pixels on the camera. We used a 10% overlap setting on all sides of each frame during mosaic acquisition.

5.8.4 Sample Analysis

The Grid and Collection plugin in Fiji was used to stitch the mosaic together. The diameter of each tissue core was approximately 0.7 mm, so the cropped dimensions of the image of each tissue core were set at 5000 x 5000 pixels. Fiji was used to perform analysis of the images. Using a Wacom tablet and the region of interest (ROI) feature on Fiji, a single layer of stroma adjoining 5-6 glands from each core was segmented for analysis (Fig. 5.5). In our study, one core from each patient was arrayed in each of the 3 slides analyzed, and thus we had 6-18 stromal regions for each patient with reduced number of regions in cases were cores were missing. The clear visibility of individual stromal fibers in the SLIM images allows us to accurately segment the stromal fiber immediately adjoining the cancerous glands. The size of each stromal region analyzed varied as a result of variation in glandular size and stromal width. We then measured the phase variance and phase gradient in the stromal region, in order to calculate optical anisotropy (g) using the scattering phase theorem.

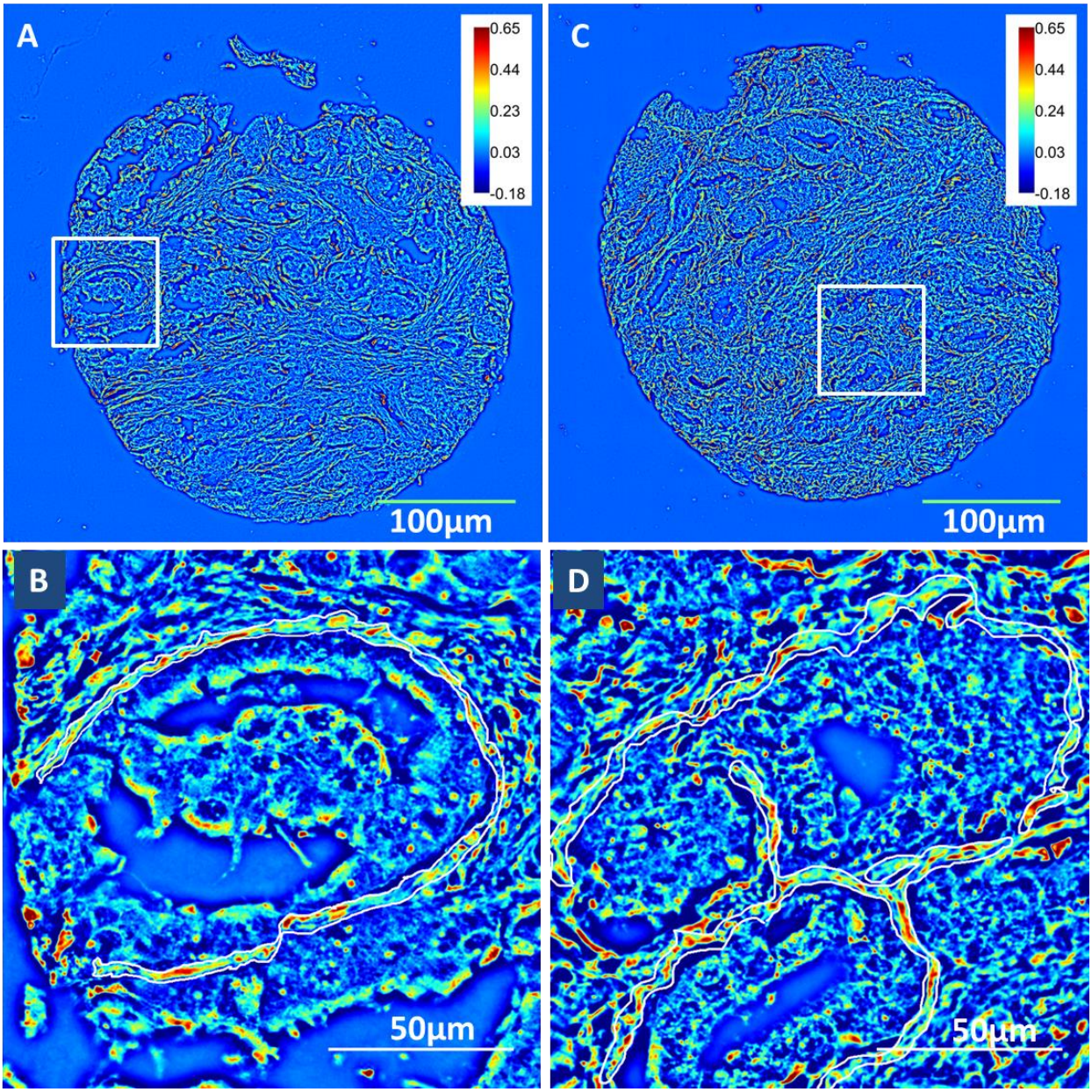

Figure 5.5: Quantitative Phase Images obtained using Spatial Light Interference Microscopy (SLIM). (A) Unstained prostatectomy core from a patient with biochemical recurrence of prostate cancer 3 months after prostatectomy **(B)** Zoomed-in region from the recurrent patient with the single layer of stroma surrounding the Grade 3 cancerous gland marked. Anisotropy in this selected region is computed for recurrence risk calculation. A lower value of anisotropy, or higher degree of fragmentation in the stroma, is observed in the patients at high risk for recurrence **(C)** Unstained prostatectomy core from a patient without biochemical recurrence of prostate cancer for 44 months PSA follow-up time after radical prostatectomy **(D)** Single layer of stroma surrounding a Grade 3 cancerous gland from the non-recurrent patient is marked, and anisotropy was calculated in this selected region. The stromal layer was less fragmented and hence had a higher value of anisotropy.

5.8.5 Optical Anisotropy (g)

Optical anisotropy (g) is defined as the average cosine of the scattering angle associated with a single scattering event. Anisotropy can be calculated from the quantitative phase images using the scattering phase theorem [22]:

$$g = 1 - \frac{1}{2k_0^2} \frac{\langle |\nabla[\varphi(r)]|^2 \rangle_r}{\langle \Delta\varphi^2(r) \rangle_r^2} \quad [1]$$

where $k_0 = 2\pi/\lambda_0$ is the wavenumber. The center wavelength of the white light used in our imaging system, λ_0=552nm. Optical anisotropy is calculated over the stromal region, r, corresponding to the ROI. $\langle \nabla[\varphi(r)] \rangle_r$ is the mean phase gradient intensity, and $\langle \Delta\varphi^2(r) \rangle_r$ is the phase variance.

Anisotropy value measured is not restricted to the tissue slice imaged and is actually a property of bulk tissue. The phase measurement and therefore g, is representative of the entire tissue when out-of-focus light is negligible. Anisotropy measurements are, therefore, thickness independent (See Appendix B for experimental evidence). Precision, and therefore repeatability, is an important requirement for prognostic tools. As in our previous study, we measured the effect of phase noise in a background area (no tissue) and measured its effect on g-values. We repeated this measurement since we used a different imaging configuration in our current study. The error is measured as:

$$\Delta g = \left| \frac{1}{2k_0^2} \frac{f_1 \Delta f_2 - f_2 \Delta f_1}{f_2^2} \right| \quad [2]$$

Where f_1 and f_2 are the square of the average phase gradient intensity and square of the phase variance, respectively, and are measured over the same background region. Δf_1 and Δf_2 are the

standard deviations in f_1 and f_2, respectively, due to phase noise. In the current imaging set-up, $\Delta g = 1.52 \times 10^{-3}$. The low error value is attributed to white light imaging, which eliminates speckles, and therefore increases precision.

5.9 References

1. in *CDC/NCHS National Hospital Discharge Survey*.
2. Han, M., et al., *Long-term biochemical disease-free and cancer-specific survival following anatomic radical retropubic prostatectomy. The 15-year Johns Hopkins experience.* Urol Clin North Am, 2001. **28**(3): p. 555-65.
3. Pound, C.R., et al., *Natural history of progression after PSA elevation following radical prostatectomy.* JAMA, 1999. **281**(17): p. 1591-7.
4. Ward, J.F., et al., *The long-term clinical impact of biochemical recurrence of prostate cancer 5 or more years after radical prostatectomy.* J Urol, 2003. **170**(5): p. 1872-6.
5. Roehl, K.A., et al., *Cancer progression and survival rates following anatomical radical retropubic prostatectomy in 3,478 consecutive patients: long-term results.* J Urol, 2004. **172**(3): p. 910-4.
6. Bubendorf, L., et al., *Metastatic patterns of prostate cancer: an autopsy study of 1,589 patients.* Hum Pathol, 2000. **31**(5): p. 578-83.
7. Eisenberger, M.A., et al., *Bilateral Orchiectomy with or without Flutamide for Metastatic Prostate Cancer.* New England Journal of Medicine, 1998. **339**(15): p. 1036-1042.
8. Shariat, S.F., et al., *An updated catalog of prostate cancer predictive tools.* Cancer, 2008. **113**(11): p. 3075-99.
9. Cooperberg, M.R., J.F. Hilton, and P.R. Carroll, *The CAPRA-S score: A straightforward tool for improved prediction of outcomes after radical prostatectomy.* Cancer, 2011. **117**(22): p. 5039-46.
10. Stephenson, A.J., et al., *Postoperative nomogram predicting the 10-year probability of prostate cancer recurrence after radical prostatectomy.* Journal of clinical oncology : official journal of the American Society of Clinical Oncology, 2005. **23**(28): p. 7005-12.
11. Punnen, S., et al., *Multi-institutional validation of the CAPRA-S score to predict disease recurrence and mortality after radical prostatectomy.* Eur Urol, 2014. **65**(6): p. 1171-7.
12. Oon, S.F., et al., *Biomarker research in prostate cancer--towards utility, not futility.* Nat Rev Urol, 2011. **8**(3): p. 131-8.
13. Sridharan, S., Macias, V., Tangella, K., Kajdacsy-Balla, A., Popescu, G. , *Prediction of Prostate Cancer Recurrence Using Quantitative Phase Imaging.* Sci Rep, 2015.
14. Kwak, J.T., et al., *Improving prediction of prostate cancer recurrence using chemical imaging.* Sci Rep, 2015. **5**: p. 8758.
15. Erho, N., et al., *Discovery and validation of a prostate cancer genomic classifier that predicts early metastasis following radical prostatectomy.* PLoS One, 2013. **8**(6): p. e66855.
16. Kattan, M.W., et al., *The addition of interleukin-6 soluble receptor and transforming growth factor beta1 improves a preoperative nomogram for predicting biochemical progression in patients with clinically localized prostate cancer.* J Clin Oncol, 2003. **21**(19): p. 3573-9.
17. Shariat, S.F., et al., *Plasminogen activation inhibitor-1 improves the predictive accuracy of prostate cancer nomograms.* J Urol, 2007. **178**(4 Pt 1): p. 1229-36; discussion 1236-7.

18. Svatek, R.S., et al., *Pre-treatment biomarker levels improve the accuracy of post-prostatectomy nomogram for prediction of biochemical recurrence.* Prostate, 2009. **69**(8): p. 886-94.
19. Sridharan, S., et al., *Prediction of Prostate Cancer Recurrence Using Quantitative Phase Imaging.* Sci. Rep., 2015. **5**.
20. Popescu, G., *Quantitative phase imaging of cells and tissues*. McGraw-Hill biophotonics. 2011, New York: McGraw-Hill. 385.
21. Wang, Z., et al., *Spatial light interference microscopy (SLIM).* Optics Express, 2011. **19**(2): p. 1016.
22. Wang, Z., H. Ding, and G. Popescu, *Scattering-phase theorem.* Optics Letters, 2011. **36**: p. 1215.
23. Ro, Y.K., et al., *Biochemical Recurrence in Gleason Score 7 Prostate Cancer in Korean Men: Significance of the Primary Gleason Grade.* Korean Journal of Urology, 2012. **53**(12): p. 826-829.
24. Rasiah, K.K., et al., *Prognostic significance of Gleason pattern in patients with Gleason score 7 prostate carcinoma.* Cancer, 2003. **98**(12): p. 2560-5.
25. Alenda, O., et al., *Impact of the primary Gleason pattern on biochemical recurrence-free survival after radical prostatectomy: a single-center cohort of 1,248 patients with Gleason 7 tumors.* World J Urol, 2011. **29**(5): p. 671-6.
26. Khoddami, S.M., et al., *Predictive value of primary Gleason pattern 4 in patients with Gleason score 7 tumours treated with radical prostatectomy.* BJU Int, 2004. **94**(1): p. 42-6.

CHAPTER 06: Colorectal Tissue Screening with Quantitative Phase Imaging

6.1 Abstract

Colorectal cancer is the second-leading cause of cancer related deaths in the United States. Screening for colorectal cancer using colonoscopy can lead to diagnosis of the disease in the pre-cancerous, or dysplastic stage and thus improve outcomes and reduce disease-specific mortality. The colonic tissue excised during screening is assessed by the pathologist in order to make a final diagnosis. However, dysplasia is typically present in 25% of colonoscopy tissue. Quantitative phase imaging (QPI) can flag specific areas of tissue with dysplasia or cancer, which require surgical intervention, with 96.3% sensitivity and 96.9% specificity. Thus QPI has the potential to help in the implementation of wide-spread screening programs.

6.2 Motivation

Colorectal cancer develops from benign adenomatous polyps that advance to carcinoma through a series of genetic mutations over the course of 5-10 years. The overall 5-year survival rate for colorectal cancer is 64.7%. When the data is further categorized based on the disease stage at diagnosis, 39.6% of the cancers are diagnosed at the local stage and has 89.8% 5-year survival rate [1]. But 36% of colorectal cancers diagnosed at regional stage have 70.5% 5-year survival rate and the 20% cases with distant metastasis have 12.9% 5-year survival rates [1]. Early diagnosis of colorectal cancer is thus strongly correlated with reduced disease-specific mortality. The United States Preventive Services Task Force (USPSTF) recommends colorectal cancer screening among individuals of the age group 50-75 years through either annual high-sensitivity fecal occult blood test (FOBT), colonoscopy every 10 years or sigmoidoscopy every 5 years combined with high-sensitivity FOBT every 3 years [2]. Colonoscopy has the highest sensitivity among all screening tools for identification of polyps and also allows for early removal of polyps, which has been linked to reduced colorectal cancer incidence and colorectal cancer-related deaths by interruption of disease progression [3-5]. In the USA, colonoscopy is the preferred form of colorectal cancer screening and the percentage of individuals in the age group of 50-75 years who underwent colorectal cancer screening increased from 54% to 65% from 2002 to 2010 [6].

The prevalence of an adenoma among all individuals undergoing colonoscopy is 25 - 27%, and the prevalence of high grade dysplasia and colorectal cancer is even lower, 1 - 3.3% [3, 7]. However, a biopsy or polyp removal is performed in 50% of all colonoscopies as current screening methods cannot distinguish adenoma from a benign polyp with high accuracy [8]. A

pathologist examines all the polyps that have been excised to determine if the tissue was benign or dysplastic or cancerous, and if further treatment is necessary.

The Patient Protection and Affordable Care Act in the United States now requires all insurances to cover cancer-screening strategies recommended by the USPSTF. This would mean that the number of colon cancer screening cases examined by pathologists will show a large increase. Considering the small proportion of cases with advanced neoplasms in the midst of a large volume of tissue excised during screening, a quantitative tool that can flag dysplastic or cancerous tissue with a high level of accuracy will help with the implementation of colonoscopy as a widespread screening tool for early colorectal cancer detection. Also, this could greatly impact screening strategies world-wide, as recent studies that have shown the critical need for implementation of colorectal cancer screening in Asia in light of an alarming increase in colorectal cancer incidence [9-11].

Semi-automated computational screening of pathology cases has had a huge impact in cervical cancer screening using the Papanicolou test, also known as the Pap smear. The FDA-approved BD Focal Point Slide Profiler, a cytologic screening tool, automatically classifies 25% cases as normal without any further analysis necessary by the pathologist, and flags 75% of the cases for further pathology analysis with a risk grouping, thus reducing the number of cases requiring examination by the pathologist [12].

Here, we show how Spatial Light Interference Microscopy (SLIM), a quantitative phase imaging method, can be used to identify dysplastic and colon cancer cases with 96.3% sensitivity and 96.9% specificity and therefore serve as a supporting diagnostic tool for pathologists and gastroenterologists and thus assist with the implementation of new colon cancer screening programs.

6.3 Quantitative Classification of Tissue Microarray Cores

In order to quantitatively classify tissue into the categories of high index of suspicion (dysplasia, intra-mucosal carcinoma and carcinoma) and low index of suspicion (normal, hyperplasia), a support vector machine (SVM) classifier was built using glandular solidity and glandular phase median as the support vectors (See Materials and Methods for details). The SVM classifier was first tested on three slides of the tissue microarray set from UIC, consisting of 816 glands from 100 cores designated as normal, 168 glands from 27 cores designated as hyperplastic, 219 glands from 34 cores designated as dysplastic and 704 glands from 102 cores designated as cancerous. 86% of the glands from normal cores and 85% of the glands from hyperplastic cores were classified into the low index of suspicion group (Fig. 6.1). 68% of the glands from dysplastic cores and 80% of the glands from cancerous cores were classified into the high index of suspicion group. It should be noted that in order for a core to be diagnosed as normal or hyperplastic, all glands in that core show normal or hyperplastic morphology on the H&E images. However, for a core to be diagnosed with dysplasia, intra-mucosal carcinoma or carcinoma, a minimum of one gland has to display said morphology on the H&E image, and other glands could have normal or hyperplastic morphology. This explains the higher discrimination accuracy seen in glandular classification from cases in the low index of suspicion group, in comparison to cases in the high index of suspicion group. This distribution in apparent mis-classifications are also visible in Fig xx that shows the number of glands classified as high-index of suspicion and low-index of suspicion in each core belonging to the normal, hyperplasia, dysplasia and carcinoma categories.

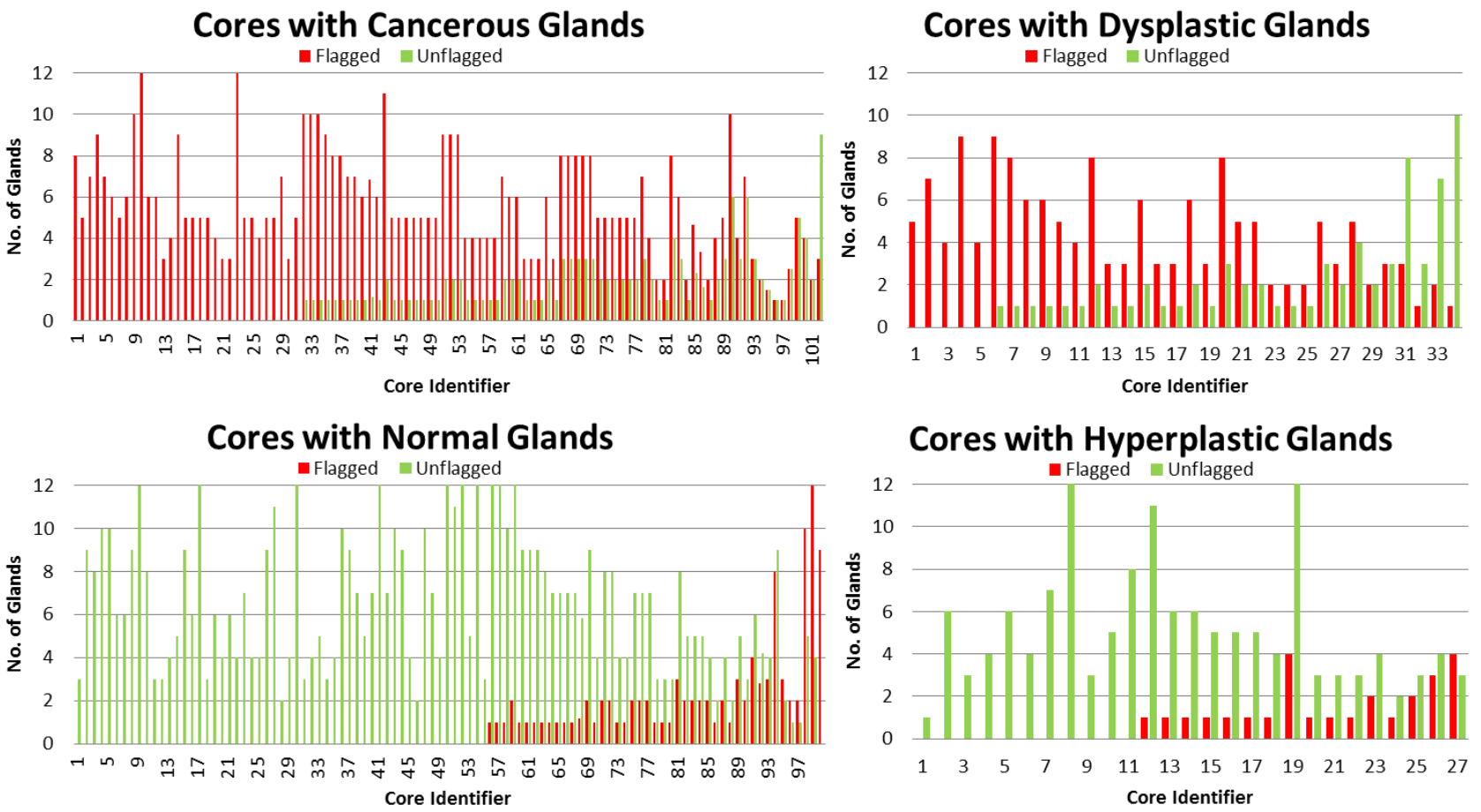

Figure 6.1: Tissue classification using Support Vector Machine (SVM). All glands from the cores were segmented and using the SVM classifier, were either flagged as high index of suspicion of un-flagged due to low index of suspicion for cancer. **(A)** Individual glands from 101 cores with one or more cancerous glands were classified using SVM. **(B)** Individual glands from 34 cores with one or more dysplastic glands were classified using the SVM classifier. **(C)** SVM classification results for glands from 99 cores with all glands showing normal morphology. **(D)** SVM classification results for glands from 27 cores with atleast one gland displaying hyperplastic morphology and all glands displaying either normal or hyperplastic morphology.

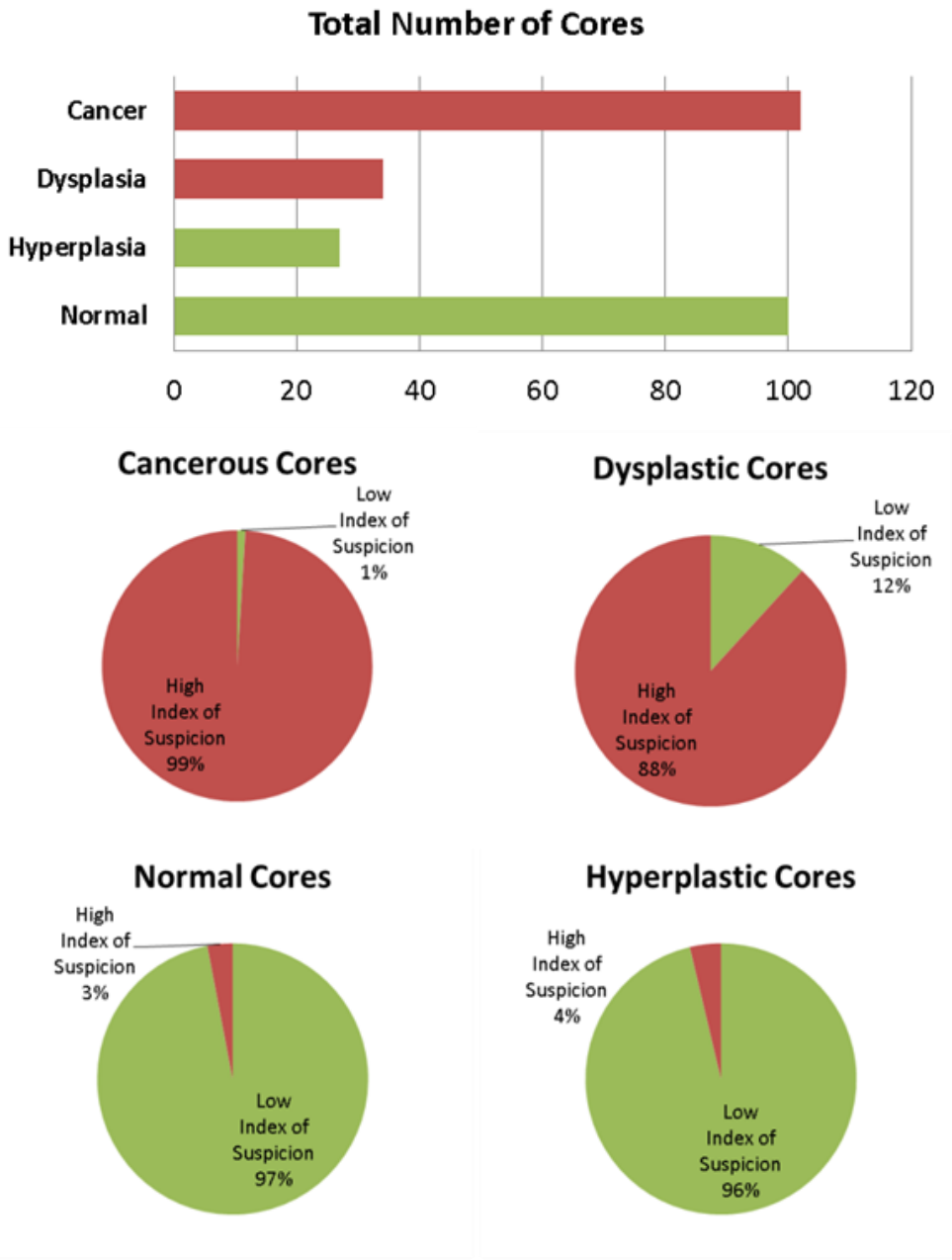

Figure 6.2: The Accuracy of Classification of Colorectal Tissue. The accuracy of classification of cancerous, dysplastic, normal and hyperplastic cores into the "high index of suspicion" and "low index of suspicion" groups is shown in the above figure. The high index of suspicion (dysplasia, cancer) cases are flagged with 96.3% sensitivity and 95.3% specificity.

Our end goal was to flag cores with suspected cancer or dysplasia for further examination by pathologists. To this end, the risk stratification of multiple glands from each core was pooled

together and a threshold was set, such that, if 50% or more glands from a single core were classified as "high index of suspicion," the core was flagged. This resulted in 135 cores being flagged for further analysis by the pathologist. A closer examination of the flagged cores showed that 88% of all cores with dysplasia and 99% of all cores with cancer were flagged (Fig. 6.2). Additionally, 5% of all normal cores and 4% of all hyperplastic cores were incorrectly flagged as high index of suspicion. The overall sensitivity and specificity for identification of high index of suspicion cases was 96.3% and 96.9% respectively.

6.4 Pathologists' Analysis of Flagged TMA Cores

The 135 cores which were flagged as high index of suspicion were then presented to two different pathologists for diagnosis on both SLIM and H&E. Neither pathologist was involved in the gold standard diagnosis that was used for building the SVM classifier for quantitative diagnosis. Additionally, they were not provided with any details regarding the accuracy of the quantitative risk stratification, to prevent classification bias. In order to train the pathologists for identification of relevant morphological features on SLIM images, they examined SLIM and H&E images of cores that were used to build the SVM classifier side-by-side. After completion of training, they were first asked to examine all flagged cases using SLIM only, and then diagnose the cores as either "normal", "hyperplasia", "dysplasia", "intra-mucosal carcinoma" or "carcinoma". Once all cases were diagnosed on SLIM, the consecutive H&E section was presented to the pathologists for diagnosis under the same categories. The main aims of this exercise were to determine if pathologists could identify the incorrectly flagged cases on SLIM alone, and to test the consensus between the SLIM and H&E diagnoses made by the pathologists.

If pathologists are able to make accurate qualitative diagnoses on SLIM images, the case-loads in pathology laboratories for tissue staining, in a colon cancer setting, could be reduced.

The agreement between the SLIM and H&E diagnosis made by the same pathologist, as well as the agreement between the SLIM and H&E diagnosis made by the two pathologists was computed using Cohen's kappa estimate [13]. The weighted Cohen's kappa estimate was used since the level of disagreement between the diagnosis of cancer as dysplasia is lower than the level of disagreement in a diagnosis of cancer as normal [14]. Our analysis showed that the weighted kappa for agreement between SLIM and H&E diagnosis of all cases by the same pathologist, or intra-observer agreement according imaging modalities, was 0.69 and 0.86 for the two pathologists (Table 6.1).

	Weighted kappa	95% Lower CI	95% Upper CI
Pathologist # 1	0.69	0.55	0.83
Pathologist # 2	0.86	0.78	0.94

Table 6.1: Intra-observer agreement among pathologists. The weighted kappa score for the agreement between the pathologist's diagnosis on SLIM and the same pathologist's diagnosis of the same case on H&E was computed for all 138 cases flagged as high-suspicion by the automated classifier. The weighted kappa score for each pathologist is in the substantial agreement range. It should be noted that all the flagging errors were identified by each pathologist on the SLIM images itself.

The kappa agreement between the H&E diagnosis of all cases compared across both pathologists was computed as 0.73, and the kappa for the SLIM diagnosis agreement by both pathologists was 0.67 (Table 6.2). Since kappa score is a conservative estimate of agreement, the kappa scores obtained in our study is considered to be in the substantial agreement range [15]. It should be noted that both pathologists were able to correctly identify all the incorrectly flagged

cases (normal, hyperplasia) on SLIM alone, and it showed consensus with their diagnoses on the H&E images of the same cases.

	Weighted kappa	95% Lower CI	95% Upper CI
H&E	0.73	0.61	0.85
SLIM	0.67	0.54	0.79

Table 6.2: Inter-observer agreement among pathologists. The weighted kappa score for the agreement between the Pathologist # 1 diagnoses on H&E and Pathologist # 2 diagnoses on H&E was computed for all 138 cases flagged as high-suspicion by the automated classifier. Their agreement on H&E is within the good agreement range. The weighted kappa score was also computed for the diagnoses by both pathologists on the SLIM images. Their agreement on SLIM is within the substantial agreement range.

6.5 Quantitative Classification of Biopsy Slides

A surgically resected colon sample was imaged using the fast tissue scanner (see Materials and Methods for details). The large tissue image was cropped to 10000x10000 pixel regions over which the glands were segmented for extracting the phase median and glandular solidity values. The SVM classifier then flagged the glands as either high or low index of suspicion and an adjacent H&E section with pathologist's diagnosis was used for comparison of diagnostic result. As shown in Fig. 6.3, the quantitative classifier flagged all the regions with cancerous or dysplastic regions as high index of suspicion and all benign regions were identified as low index of suspicion.

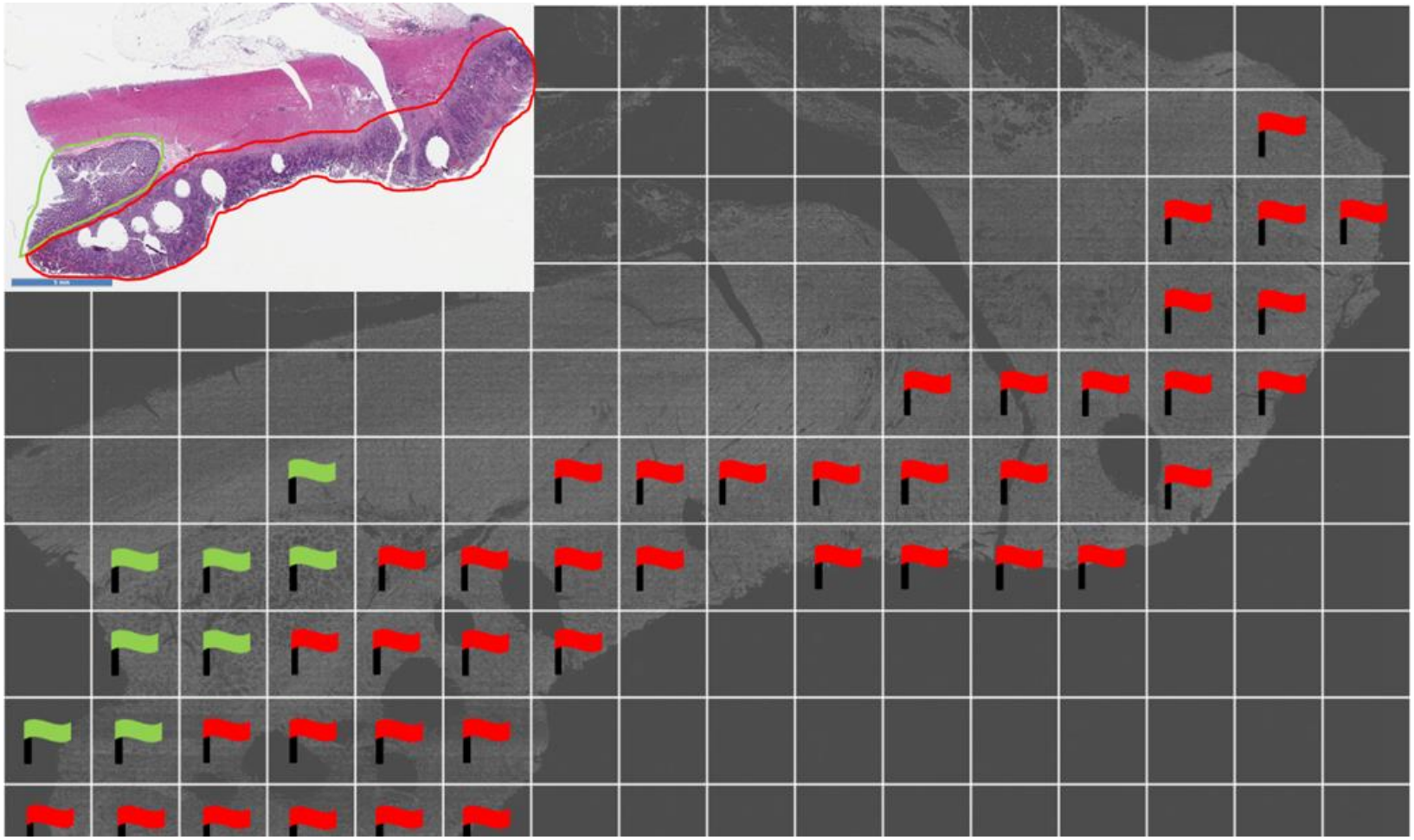

Figure 6.3: Quantitative diagnosis on large tissue areas. A surgically resected colon tissue was imaged using the fast tissue scanner and using the SVM classifier, the glands in 1587 x 1587μm regions were classified as either high index of suspicion or low index of suspicion. After thresholding, such that 50% or more glands classified in one class resulted in that class being the final diagnosis, each 1587 x 1587μm was flagged red (high index of suspicion for cancer or dysplasia) or green (low index of suspicion of disease). The inset shows the H&E diagnosis provided by the pathologist. There is a high degree of agreement between the quantitative diagnosis and pathology diagnosis.

6.6 Discussion

10% of all adenomatous polyps are cancerous [16] and endoscopic methods currently used in clinic cannot distinguish adenomas from carcinomas. Many optical methods have been developed for conjunction with endoscopy methods for colorectal cancer screening and have been reviewed elsewhere [17, 18]. Confocal endomicroscopy has shown potential for in-vivo distinction between hyperplastic and dysplastic tissue but it involves the use of contrast agents such as fluorescin and acriflavine hydrochloride and is time-consuming [19-21]. In-vivo spectroscopy-based methods such as low coherence enhanced backscattering spectroscopy and inverse spectroscopic optical coherence tomography have been used to identify normal-appearing tissue that is adjacent to dysplastic and cancerous tissue, also known as the field effect, to guide effective diagnoses and improve miss-rates of colonoscopy [22, 23]. Optical coherence tomography methods also have the resolution to differentiate between gastrointestinal mucosa and the muscular layers, thus showing potential for in-vivo diagnosis [24-27]. Elastic scattering spectroscopy uses a point scanning method and has 84% sensitivity and specificity for distinguishing hyperplasia from adenomas, which may not be optimal [28]. Raman spectroscopy and fluorescence spectroscopy based measurements have shown higher sensitivity and specificity rates for distinguishing adenoma from hyperplasia, but they still do not approach the accuracy of histopathology and are less practical due to issues related to power of the optical signals [29, 30].

Histopathology, following colonoscopy tissue resection, continues to remain the gold-standard for diagnosis of colorectal cancer and dysplasia. SLIM has a high sensitivity and high specificity for flagging cases requiring pathological examination, and also flags specific regions on large tissue samples, such as biopsies, requiring the attention of pathologists. Since pathologists are able to identify the incorrectly flagged cases on SLIM alone, the number of

cases that will have to be stained is reduced, thus reducing case-loads for tissue processing in pathology labs. Thus SLIM can help optimize diagnostic time-lines in colorectal screening programs.

6.7 Materials and Methods

6.7.1 Study Design

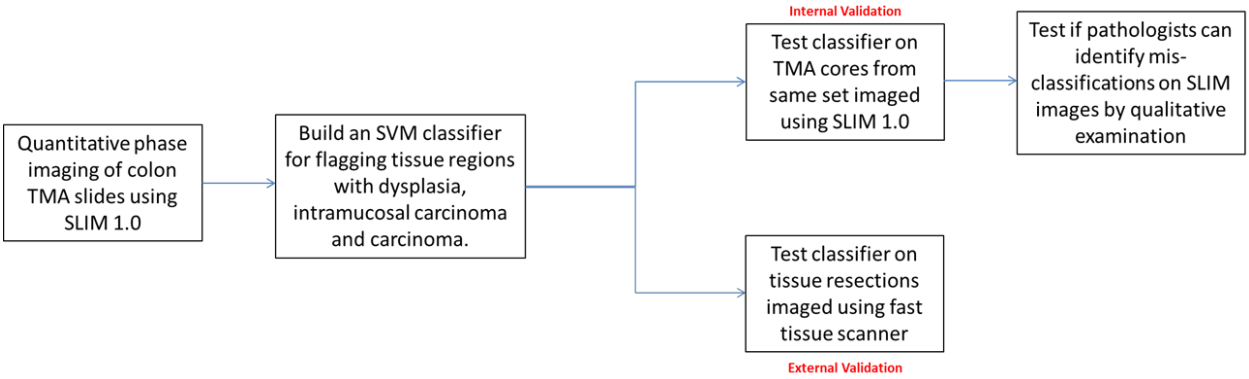

Figure 6.4: Schematic for quantitative diagnosis. Quantitative parameters extracted from SLIM images of multiple glands from 131 patients in a tissue microarray set. The parameters from 25% of the patients were used to build a support vector machine (SVM) classifier on MATLAB. In the internal validation of the classifier, it was tested on the remaining 75% of the patients and additionally, pathologists were asked to make a diagnosis on SLIM images, to check if false positives could be identified on SLIM itself. In the external validation, a large surgically resected colon tissue slide was imaged using the fast tissue scanner and the classifier was tested on this image.

A schematic for the design of this study is shown in Fig 6.4. A tissue microarray (TMA) set containing tissue with colon carcinoma, intramucosal carcinoma, dysplasia, hyperplasia and normal colonic mucosa was imaged using the QPI technique, spatial light interference microscopy, SLIM 1.0 scanner. Quantitative features were extracted from the image to construct a support-vector machine (SVM) classifier on MATLAB to flag cases with dysplasia, intramucosal carcinoma and carcinoma as high index of suspicion using 25% of the cases in the TMA set. The classifier was then tested on the remaining 75% cases in the TMA set as an internal validation. Subsequently, collaborating pathologists were asked to make a diagnosis on

the SLIM images of flagged cases to determine utility for reducing tissue processing case-loads in pathology laboratory. Finally, colon tissue surgical resection and biopsy slides were obtained from two different sites and imaged using the fast tissue scanner. The SVM classifier was then tested on the tissue as an external validation.

6.7.2 TMA Cohort

A tissue microarray (TMA) was prepared with archival pathological material collected from 131patients who underwent colon resection for treatment of colon cancer at the University of Illinois at Chicago (1993 to1999). For each case, 0.6 mm in diameter colon core duplicates of tumor, normal, dysplastic, and hyperplastic mucosa were retrieved based on donor block availability. Tissue cores were transferred using a MTA-1 manual arrayer (Beecher Instruments, Inc.) into a high density array composed by four blocks with primary colon cancer (n=127patients) and mucosa of normal (n=131 patients), dysplastic (n=33 patients), and hyperplastic colon (n=86 patients). The tissue collection was performed in accordance with the procedures approved by the Institutional Review Board at the University of Illinois at Chicago (IRB Protocol Number: 2004-0317).

Two 4μm sections were cut from each of the four blocks at the University of Illinois at Chicago. The first section was de-paraffinized and stained with hematoxylin and eosin (H&E) and imaged using the Nanozoomer. One of the pathologists on our team made a diagnosis for all tissue cores in the TMA set and this was provided to us as the "ground truth" for analysis. A second adjacent section was cut at 4μm thickness and was de-paraffinized and cover-slipped without staining using the aqueous mounting medium. This slide was then sent to the Quantitative Light Imaging Laboratory at Urbana, Illinois for further analysis. These studies followed the protocols outlined

in the procedures approved by the Institutional Review Board at the University of Illinois at Urbana-Champaign (IRB Protocol Number: 13900).

6.7.3 Quantitative Phase Imaging of TMA Slides

An unstained set of TMA slides with colorectal tissue samples from patients with cancer, dysplasia, and hyperplasia; and normal controls was imaged using spatial light interference microscopy, SLIM 1.0, the imaging system is described in detail elsewhere [31]. Briefly, SLIM is an add-on module to the commercial phase contrast microscope that introduces 3 additional phase shifts to the phase contrast image using a spatial light modulator (SLM) and records them as intensity images. The quantitative phase is then computed mathematically from the four intensity images (where scattered an un-scattered light are phase shifted by $\pi/2$, π, $3\pi/2$ and 2π) using MATLAB.

The TMA slides were imaged using the 40X/0.75NA objective of the SLIM 1.0 imaging system. The spatial resolution of the resulting image was 0.4μm, which is the resolution of the objective. The optical path length sensitivity of this imaging system is 0.3nm. The SLIM 1.0 system has the ability to mosaic large fields of view necessary for tissue scanning, but the speed is limited by the refresh rate of the SLM, capture rate of the camera and the computational ability of the computer. A single field of view was 1388 x 1040 pixels on the CCD camera, and this corresponded to a physical size of 99 x 74μm of the object, in this case, the tissue sample. Each colorectal tissue core was approximately 0.8mm in diameter, and therefore, this corresponded to a mosaic with 80 imaging fields of view. Every 5 fields of view were manually focused, thus setting up multiple smaller focal planes and ensuring that all tissue regions were in-focus. The images were captured at 0% overlap in all directions, and this setting was adjusted using the

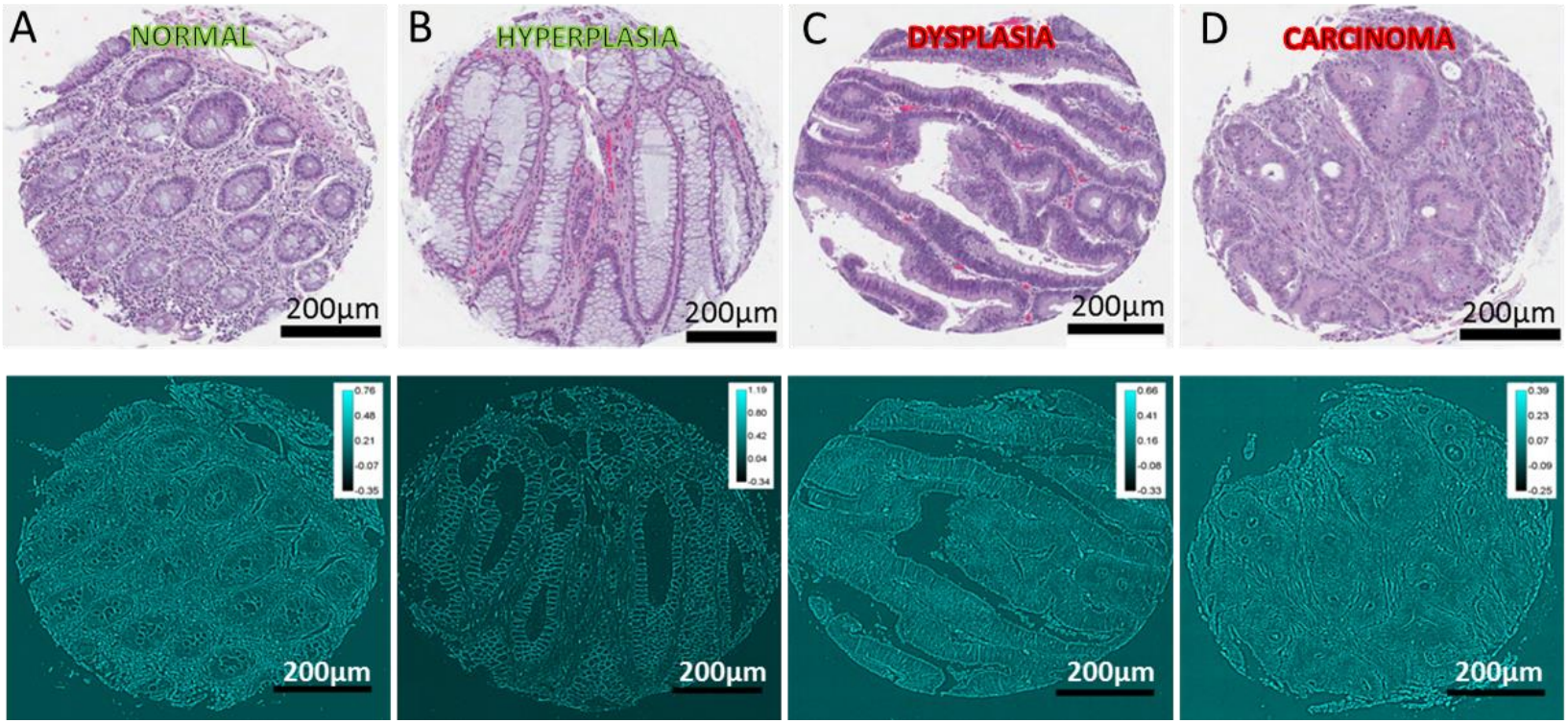

Figure 6.5: Quantitative phase images of colon disease progression. The qualitative tissue features seen in H&E-stained images are recovered in the quantitative phase images obtained using SLIM. **(A)** In normal colon tissue, the glands are small and the cells are well differentiated. **(B)** In hyperplastic colon tissue, the glands are bigger due to hyper-proliferation of the differentiated cells. **(C)** In dysplastic colon tissue, there is an increase in glandular density, the cells show altered morphology, but the glands do not invade the smooth muscle layer. **(D)** In colon adenocarcinoma, the undifferentiated cells from the crypts are a dominant cell-type in the glands and the glands show evidence of invasion.

microscope capture software, AxioVision. The images were stitched using an ImageJ plugin that was built in our lab and each core was cropped to an image size of 12000 x 12000 pixels (Fig 6.5).

6.7.4 Support Vector Machine (SVM) Training

Complete glands present on all cores were manually segmented on SLIM images using a Wacom tablet and the region of interest (ROI) feature on ImageJ. Solidity, which is the ratio of the area of the gland to the area of the convex hull fitted around the gland, and median phase value in each gland was measured.

25% of the cases in the TMA set were used to build an automated classifier for diagnosis. Solidity and phase median measurements were extracted from 454 glands from cores diagnosed as normal and 194 glands from cores diagnosed with cancer. These measurements were used to create a classifier with the support vector machine (SVM) algorithm on MATLAB (Fig. 6.6). A linear kernel was used to build the classifier and sequential minimal optimization was used to calculate the hyper-plane for separation of the different classes of data. The classes designated were low index of suspicion which would contain normal and hyperplastic tissue, and high index of suspicion, which would contain dysplastic and cancerous tissue.

6.7.5 Internal Validation

The TMA cores from the three slides, which were not used for building the classifier, were used for internal validation of the classifier. The solidity and phase median values were extracted from 816, 168, 219 and 704 glands from 100, 27, 34 and 102 cores diagnosed as normal, hyperplasia, dysplasia and cancer respectively. Using the SVM classifier, each gland was then stratified as low or high index of suspicion.

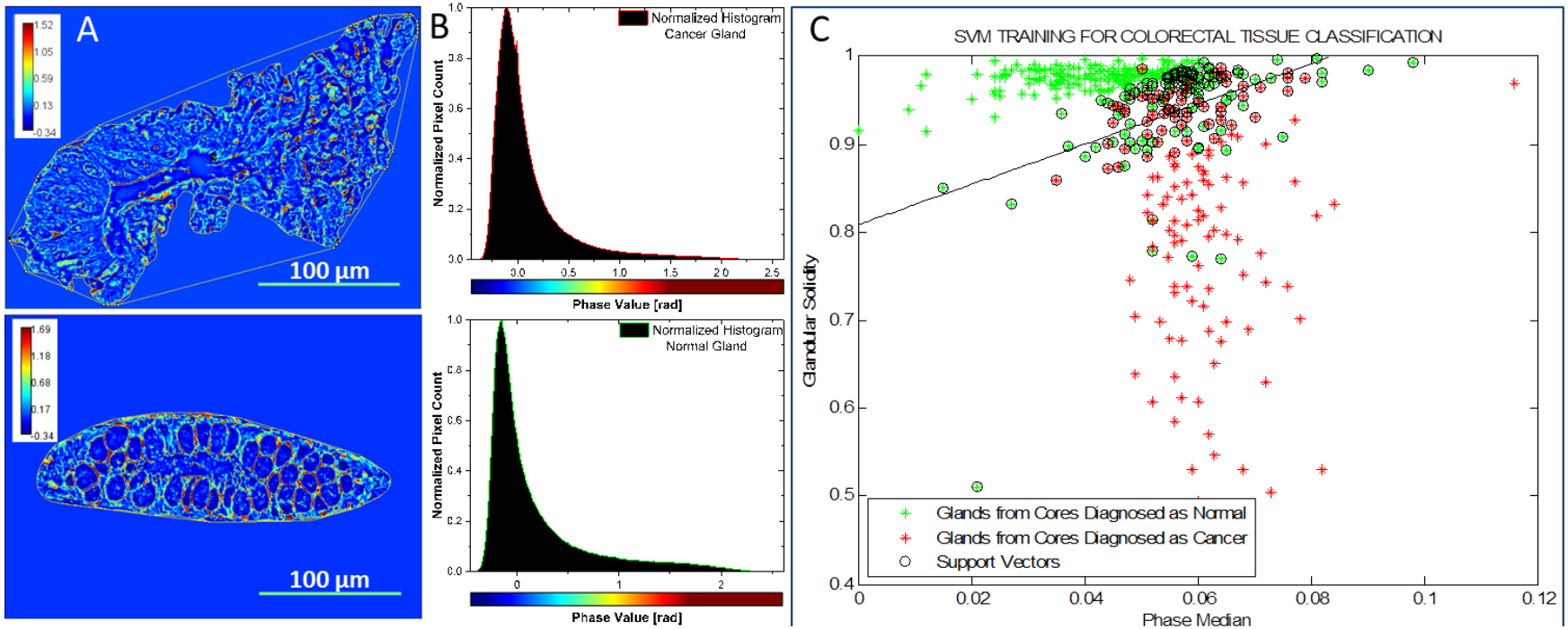

Figure 6.6: Quantitative parameters for classification. **(A)** Glandular solidity is the ratio of the area of the gland, to the area of a convex hull fitted around the gland. Glands with dysplasia and carcinoma have lower solidity values than benign glands due to invasive edges. **(B)** The phase distribution in a cancerous gland is over a wider range of phase values than normal glands. Cancerous glands have a higher phase median value than normal glands. **(C)** Glandular solidity and phase median were combined using a support-vector machine classifier in MATLAB, to build a linear kernel classifier to separate normal and cancerous glands. 454 glands from 49 normal cores and 194 glands from 32 cancerous cores were used to build the classifier.

6.7.6 External Validation

A paraffin-embedded surgically resected colon sample was obtained from the University of Illinois at Chicago. It was sectioned at 4μm thickness, de-paraffinized and later coverslipped with aqueous mounting medium. The slide was imaged using the commercial SLIM system (Cell Vista, Q100) that has a tissue scanning component. The slide was imaged with the 40X/0.75NA objective, and had a spatial resolution of 0.4μm. The size of each field of view was 221 x 165μm, corresponding to 1392 x 1040 pixels on the CCD camera. 15,589 fields of view were mosaicked together, with 10% overlap on all sides, to image the surgically resected tissue. The images were stitched together using software developed in the QLI laboratory and then cropped into 176 images of 10000 x 10000 pixels, corresponding to 1587.3 x 1587.3μm . Manual segmentation of glands was performed on these cropped images, using ImageJ, to measure the solidity and median phase value of the glands. The SVM classifier was used to classify the glands as low or high index of suspicion. The individual glandular diagnoses were then thresholded at 50% to obtain a single flagging measure for each 10000x10000 pixel tissue region. Thus multiple diagnoses can be made in order to flag specific regions for pathology assessment.

6.8 References

1. Howlader N, N.A., Krapcho M, Garshell J, Miller D, Altekruse SF, Kosary CL, Yu M, Ruhl J, Tatalovich Z,Mariotto A, Lewis DR, Chen HS, Feuer EJ, Cronin KA. *SEER Cancer Statistics Review, 1975-2011*. 2014 2012 [cited 2014 September, 10].
2. Force, U.S.P.S.T. *Final Recommendation Statement: Colorectal Cancer: Screening*. 2014 October 2014 [cited 2015 January]; Available from: http://www.uspreventiveservicestaskforce.org/Page/Document/RecommendationStatementFinal/colorectal-cancer-screening.
3. Winawer, S.J., *Natural history of colorectal cancer.* The American Journal of Medicine, 1999. **106**(1, Supplement 1): p. 3-6.
4. Winawer, S.J., et al., *Prevention of Colorectal Cancer by Colonoscopic Polypectomy.* New England Journal of Medicine, 1993. **329**(27): p. 1977-1981.
5. Zauber, A.G., et al., *Colonoscopic Polypectomy and Long-Term Prevention of Colorectal-Cancer Deaths.* New England Journal of Medicine, 2012. **366**(8): p. 687-696.
6. *Vital signs: colorectal cancer screening test use--United States, 2012.* MMWR Morb Mortal Wkly Rep, 2013. **62**(44): p. 881-8.
7. Giacosa, A., F. Frascio, and F. Munizzi, *Epidemiology of colorectal polyps.* Tech Coloproctol, 2004. **8 Suppl 2**: p. s243-7.
8. Pollitz, K., Lucia, K., Keith, K., Smith, R., Doroshenk, M., Wolf, H., Weber, T.K.,, *Coverage of Colonoscopies Under the Affordable Care Act's Prevention Benefit*, 2012, The Kaiser Family Foundation, American Cancer Society, National Colorectal Cancer Roundtable.
9. Sung, J.J.Y., et al., *Increasing incidence of colorectal cancer in Asia: implications for screening.* The Lancet Oncology, 2005. **6**(11): p. 871-876.
10. Leung, W.K., et al., *Colorectal neoplasia in Asia: a multicenter colonoscopy survey in symptomatic patients.* Gastrointestinal Endoscopy, 2006. **64**(5): p. 751-759.e1.
11. Konishi, T., et al., *Difference in incidence of colorectal cancer between men and women in Asia.* The Lancet Oncology, 2006. **7**(2): p. 104-105.
12. Pantanowitz, L., *Automated Pap Tests*, in *Practical Informatics for Cytopathology*, L. Pantanowitz and A.V. Parwani, Editors. 2014, Springer New York. p. 147-155.
13. Cohen, J., *A Coefficient of Agreement for Nominal Scales.* Educational and Psychological Measurement, 1960. **20**(1): p. 37-46.
14. Cohen, J., *Weighted Kappa - Nominal Scale Agreement with Provision for Degrees of Disagreement.* American Psychologist, 1967. **22**(7): p. 544-&.
15. Viera, A.J. and J.M. Garrett, *Understanding interobserver agreement: the kappa statistic.* Fam Med, 2005. **37**(5): p. 360-3.
16. Kinzler, K.W. and B. Vogelstein, *Lessons from hereditary colorectal cancer.* Cell, 1996. **87**(2): p. 159-70.
17. Goetz, M., A. Watson, and R. Kiesslich, *Confocal laser endomicroscopy in gastrointestinal diseases.* Journal of Biophotonics, 2011. **4**(7-8): p. 498-508.
18. Roy, H.K. and V. Backman, *Spectroscopic applications in gastrointestinal endoscopy.* Clin Gastroenterol Hepatol, 2012. **10**(12): p. 1335-41.
19. Sanduleanu, S., et al., *In vivo diagnosis and classification of colorectal neoplasia by chromoendoscopy-guided confocal laser endomicroscopy.* Clin Gastroenterol Hepatol, 2010. **8**(4): p. 371-8.

20. Polglase, A.L., et al., *A fluorescence confocal endomicroscope for in vivo microscopy of the upper- and the lower-GI tract.* Gastrointest Endosc, 2005. **62**(5): p. 686-95.
21. Kiesslich, R., et al., *Confocal laser endoscopy for diagnosing intraepithelial neoplasias and colorectal cancer in vivo.* Gastroenterology, 2004. **127**(3): p. 706-13.
22. Radosevich, A.J., et al., *Ultrastructural alterations in field carcinogenesis measured by enhanced backscattering spectroscopy.* J Biomed Opt, 2013. **18**(9): p. 097002.
23. Yi, J., et al., *Spatially resolved optical and ultrastructural properties of colorectal and pancreatic field carcinogenesis observed by inverse spectroscopic optical coherence tomography.* J Biomed Opt, 2014. **19**(3): p. 36013.
24. Pfau, P.R., et al., *Criteria for the diagnosis of dysplasia by endoscopic optical coherence tomography.* Gastrointestinal Endoscopy, 2003. **58**(2): p. 196-202.
25. Sivak Jr, M.V., et al., *High-resolution endoscopic imaging of the GI tract using optical coherence tomography.* Gastrointestinal Endoscopy, 2000. **51**(4): p. 474-479.
26. Kobayashi, K., et al., *High-resolution cross-sectional imaging of the gastrointestinal tract using optical coherence tomography: preliminary results.* Gastrointestinal Endoscopy, 1998. **47**(6): p. 515-523.
27. Tearney, G.J., et al., *In Vivo Endoscopic Optical Biopsy with Optical Coherence Tomography.* Science, 1997. **276**(5321): p. 2037-2039.
28. Dhar, A., et al., *Elastic scattering spectroscopy for the diagnosis of colonic lesions: initial results of a novel optical biopsy technique.* Gastrointestinal Endoscopy, 2006. **63**(2): p. 257-261.
29. Molckovsky, A., et al., *Diagnostic potential of near-infrared Raman spectroscopy in the colon: Differentiating adenomatous from hyperplastic polyps.* Gastrointestinal Endoscopy, 2003. **57**(3): p. 396-402.
30. Mycek, M.A., K.T. Schomacker, and N.S. Nishioka, *Colonic polyp differentiation using time-resolved autofluorescence spectroscopy.* Gastrointestinal Endoscopy, 1998. **48**(4): p. 390-394.
31. Wang, Z., et al., *Spatial light interference microscopy (SLIM).* Optics Express, 2011. **19**(2): p. 1016.

CHAPTER 07: Summary & Future Work

In my thesis, I have shown how quantitative phase imaging has the potential to be a great asset in the pathology toolbox. The quantitative nature of this method eliminates intra- and inter-observer differences. The utility of this method with FFPE tissue makes it fit in well with current pathology practices, without the need for changes in tissue processing pipelines. Additionally, the morphological information in H&E images is retrieved qualitatively in phase images, thus allowing pathologists to perform image segmentation, when necessary, without extensive additional training for identification of tissue compartments, as observed in the qualitative diagnosis of colorectal images by our pathology collaborators. Since QPI maps are self-calibrating with respect to illumination, machine learning implementation for automated classification will be easier to implement. The fast scanning ability of SLIM systems will also help in situations where high throughput is necessitated, as in screening settings.

In the case of prostate cancer, quantitative Gleason grading using QPI has higher classification accuracy than currently reported clinical consensus studies [1, 2]. This will help improve treatment outcomes. Machine learning algorithms used in conjunction with QPI can eliminate sources of bias in quantitation, such as region of interest selection, and further improve reliability of Gleason grades.

Anisotropy measured in QPI images is a powerful prognosticator of prostate cancer recurrence. The prognosis ability works particularly well for patients with Gleason score 7+ prostate cancers where current prognostic methods such as CAPRA-S and Kattan nomogram based methods have poor predictive ability. Anisotropy can thus enable early adjuvant treatment for patients undergoing prostatectomy, and thus reduce the risk of recurrence, especially in patients with intermediate Gleason grades. Among patients with high Gleason grades, 8-10, anisotropy has

added specificity over clinical methods to reduce over-treatment. It is important to note that in our studies, the end point was biochemical recurrence which serves as a surrogate end-point for metastatic recurrence. 29 - 34% of biochemical recurrence progresses to metastatic recurrence, which has poor survival rates [3, 4]. It is important to study if anisotropy, in conjunction with other clinical methods, can improve prediction of metastasis and risk of prostate cancer specific mortality, further reducing over-treatment of patients with intermediate and high Gleason grades. A tool that can make such predictions at the pre-surgical stage will be of great comfort for patients trying to make a decision between watchful waiting, active surveillance and surgery [5, 6]. So it is important study if QPI can help with decisions regarding treatment options with more value than Gleason grading itself, and methods that combine Gleason grading with other patient characteristics, such as D'Amico risk stratification and Epstein criteria [7-9].

Finally, with the fast tissue scanner, SLIM now has the ability to help in large volume settings such as colorectal cancer screening. Important problems in colon pathology include being able to differentiate between benign conditions such as irritable bowel disease and Crohn's colitis, which often results in repeat biopsies for diagnosis [10]. Additionally, the ability to predict which patients with dysplasia are likely to progress to invasive carcinoma can help guide surgical decisions, especially for patients with high grade dysplasia or intra-mucosal carcinoma. Studies have shown than colonoscopies can miss upto 24% of adenomas due to flat dysplastic presentation in an endoscopy, as opposed to polyps [11]. It would therefore be worthwhile to study if QPI has the ability to detect the so-called field effect in an adjacent polyp resected during colonoscopy and use that information to predict the presence of adjacent dysplasia, and help with decisions about frequency of colonoscopy for such patients.

7.1 References

1. Allsbrook, W.C., Jr., et al., *Interobserver reproducibility of Gleason grading of prostatic carcinoma: urologic pathologists.* Human pathology, 2001. **32**(1): p. 74-80.
2. Allsbrook, W.C., Jr., et al., *Interobserver reproducibility of Gleason grading of prostatic carcinoma: general pathologist.* Human pathology, 2001. **32**(1): p. 81-8.
3. Porter, M.P., J.L. Stanford, and P.H. Lange, *The distribution of serum prostate-specific antigen levels among American men: Implications for prostate cancer prevalence and screening.* Prostate, 2006. **66**(10): p. 1044-1051.
4. D'Amico, A.V., et al., *Biochemical outcome after radical prostatectomy, external beam radiation therapy, or interstitial radiation therapy for clinically localized prostate cancer.* Jama-Journal of the American Medical Association, 1998. **280**(11): p. 969-974.
5. Bill-Axelson, A., et al., *Radical Prostatectomy or Watchful Waiting in Early Prostate Cancer.* New England Journal of Medicine, 2014. **370**(10): p. 932-942.
6. Wilt, T.J., et al., *Radical Prostatectomy versus Observation for Localized Prostate Cancer.* New England Journal of Medicine, 2012. **367**(3): p. 203-213.
7. Rodrigues, G., et al., *Pre-treatment risk stratification of prostate cancer patients: A critical review.* Can Urol Assoc J, 2012. **6**(2): p. 121-7.
8. Kryvenko, O.N., et al., *Biopsy criteria for determining appropriateness for active surveillance in the modern era.* Urology, 2014. **83**(4): p. 869-74.
9. Albertsen, P.C., et al., *Prostate cancer and the Will Rogers phenomenon.* J Natl Cancer Inst, 2005. **97**(17): p. 1248-53.
10. Dignass, A., et al., *Second European evidence-based consensus on the diagnosis and management of ulcerative colitis Part 1: Definitions and diagnosis.* Journal of Crohn's and Colitis, 2012. **6**(10): p. 965-990.
11. Rex, D.K., et al., *Colonoscopic miss rates of adenomas determined by back-to-back colonoscopies.* Gastroenterology, 1997. **112**(1): p. 24-8.

APPENDIX A: System Calibration for Anisotropy Measurements

Optical anisotropy, as measured with the scattering phase theorem, is a function of phase gradient and phase variance. However, measurement of phase gradient and variance are sensitive to differences in measurement conditions, such as the number of pixels corresponding to each micron, or physical dimensions, of the CCD camera and the angles measured by an optical system. In our previous study, we used Spatial Light Interference Microscopy (SLIM 1.0) for measurement of quantitative phase images (QPI), and it had a different optical configuration from Cell Vista Q100, which was used for QPI in this study. Additionally, while we used the same magnification objective, 40X/0.75NA on both systems, the physical dimensions of the camera were different on the two systems, with 14pixels per micron on SLIM 1.0 and 6.3 pixels per micron on Cell Vista Q100.

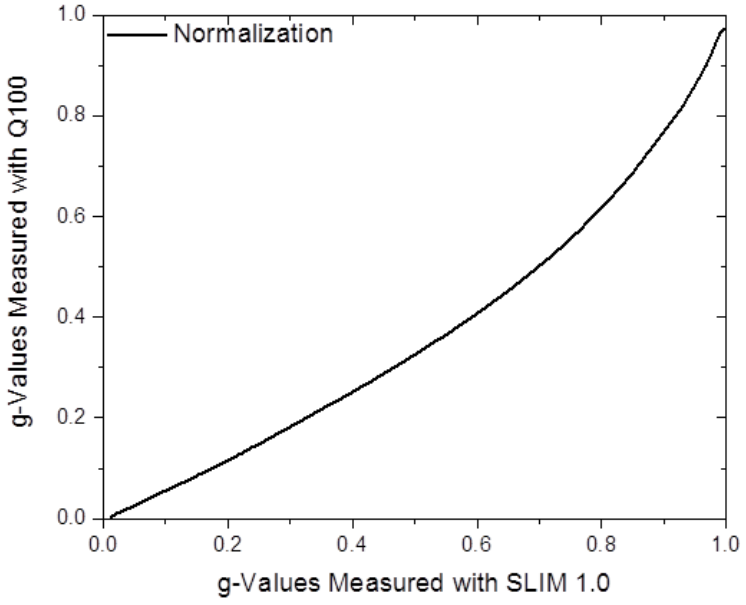

Figure A.1: Calibration Curve for Anisotropy. The calibration curve normalizes anisotropy measurements from the Q100 SLIM system to the anisotropy measurements obtained using SLIM 1.0. Anisotropy values measured using SLIM 1.0 are higher than that from the Q100 imaging system.

In order to normalize the measurement of anisotropy across the two imaging systems, we used a cumulative distribution function based transformation approach. A prostatectomy tissue core from the OCTMA5 data-set (Cooperative Prostate Cancer Tissue Resource, Chicago), which was used in our previous study, was re-imaged using the Q100 imaging system. Anisotropy was calculated in the entire tissue core using a 4.42 micron averaging window, corresponding to the average width of individual stromal fibers surrounding cancerous glands. Histograms of anisotropy over a range of 0 to 1 was calculate with 512 bin width on the SLIM 1.0 images and 1024 bin width on the Q100 SLIM system. The histograms were converted to cumulative distribution functions and a 1-to-1 anisotropy mapping was performed by matching the height of the histogram corresponding to each g-range. The calibration curve obtained through this method is shown in Fig A.1. The anisotropy values measured using Q100 are lower than the measurements from SLIM 1.0. The Q100 system is more sensitive to finer features and therefore the anisotropy measurements are lower.

Tissue preparation is another possible source of variation in anisotropy measurements. In order to determine if systemic calibration is the only source of variation in g-values, we performed a 2-step validation:

1. We measured the anisotropy cut-off value for optimal prediction of biochemical recurrence using the prostatectomy samples from the Prostate Cancer Biorepository Network (PCBN) that was used in this study. The PCBN samples were sectioned at New York University and were de-paraffinized and cover-slipped using aqueous mounting medium at the University of Illinois at Chicago.

The un-calibrated cut-off value for recurrence prediction was $g = 0.82$, which after calibration corresponds to $g = 0.93$.

2. We imaged prostatectomy samples obtained from CPCTR using both the Q100 system and the SLIM 1.0 system. The CPCTR samples were sectioned at the University of Illinois at Chicago, de-paraffinized and cover-slipped using aqueous mounting medium at Presence Covenant Medical Center, Urbana, Illinois.

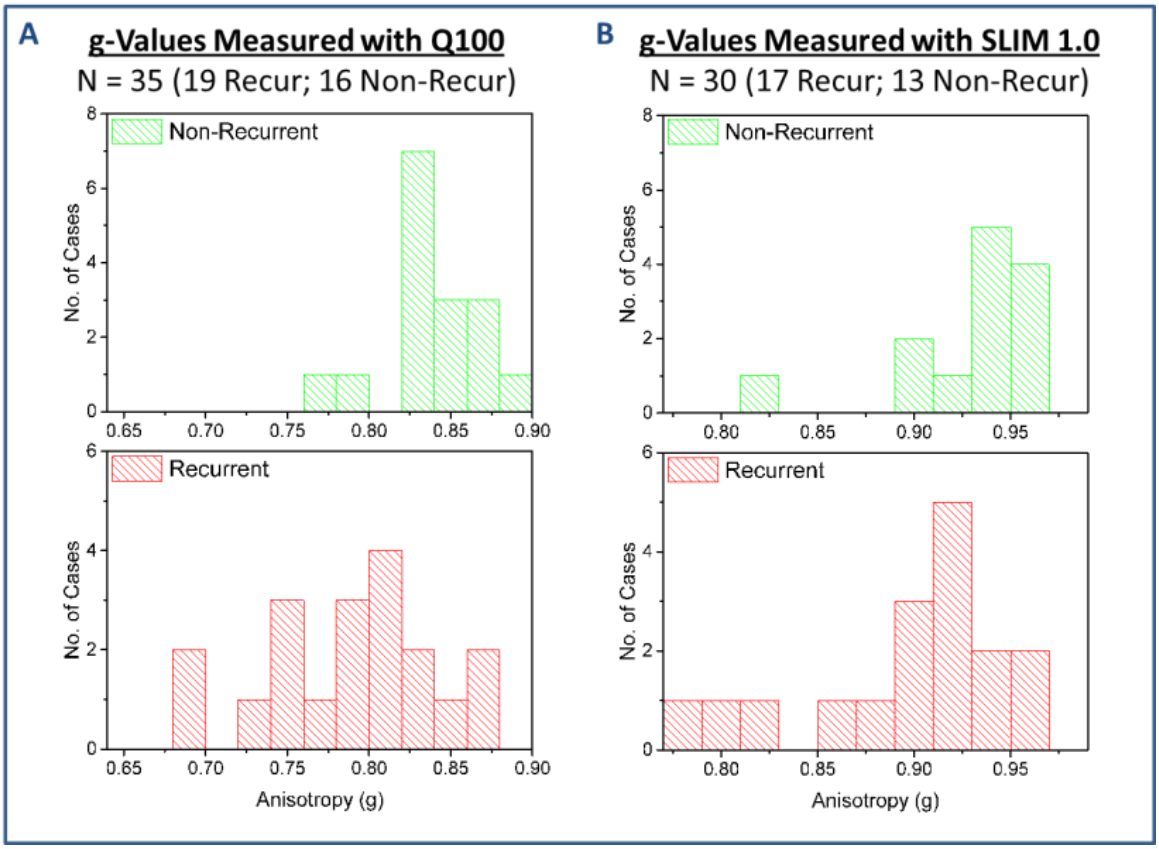

Figure A.2: Precision of Anisotropy Measurements. A) In order to measure the precision of the calibration curve, anisotropy was measured on 70 cores from 35 patients in the CPCTR TMA set using Q100 imaging system. The optimal cut-off value for recurrence prediction was determined to be g=0.82, corresponding to the un-calibrated g cut-off value measured for the PCBN TMA set. The calibrated value is g= 0.93. **B)** Anisotropy was measured on 120 cores from 30 patients in the CPCTR TMA set using the SLIM 1.0 imaging system. The optimal cut-off value for recurrence prediction was g=0.93 corresponding to the calibrated value from the Q100 system.

Prostatectomy tissue from 35 patients (19 with recurrence and 16 without recurrence), with 2 cores per patient, were imaged using the Q100 system. Anisotropy measurements were performed on a single layer of stroma surrounding 6-12 cores per patient. The un-calibrated

optimal cut-off value for recurrence prediction was g = 0.82 and after calibration, this corresponded to g = 0.93 (Fig A.2-A). This corresponded to the cut-off value obtained for the PCBN TMA imaged using the Q100 system.

Prostatectomy tissue from 30 patients, that was imaged using Q100, was also imaged using the SLIM 1.0 imaging system. Anisotropy measurements were performed on a single layer of stroma surrounding 6-16 glands per patient. The optimal cut-off value for recurrence prediction in that cohort was g = 0.93 (Fig A.2-B). This value corresponds to the post-calibration cut-off value from Q100.

APPENDIX B: Sectioning Effects on Anisotropy Measurements

Anisotropy measurements are independent of thickness, when the light transmitted through tissue is in focus. Here, we show results from an experiment measuring the uniformity of pathology tissue sections in small regions of tissue, corresponding to a tissue core and also study the effect of tissue sections of varying thickness on anisotropy measurements.

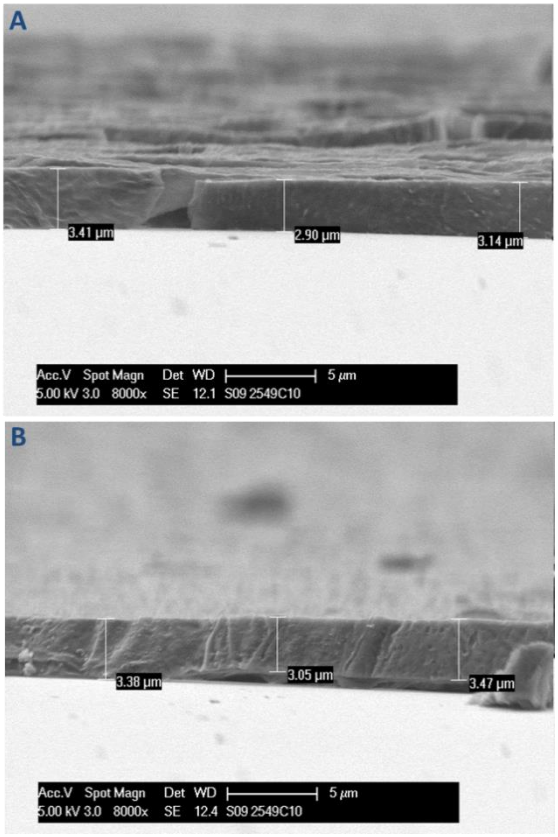

Figure B.1: Determination of Tissue Thickness. A) Paraffinized thyroid tissue of 3.5µm sectioning thickness was coated with a standard gold/palladium target and imaged using a scanning electron microscope. The thickness of the tissue shows a small decrease, followed by an increase, indicating changes in tissue morphology. **B)** The same trend is seen in a different tissue region on the same slide.

Paraffin-embedded thyroid tissue was sectioned at 3.5µm thickness and placed on a glass slide. The sample was coated with a standard gold/palladium target using a sputter coater (Denton Vacuum, Desk-1 TSC). A cross-section of the metal-coated tissue slide was then imaged using a

scanning electron microscope (FEI Company, Phillips XL30 ESEM-FEG), and the images are shown in Fig B.1-A, B. A sectioning artifact would manifest itself as a uniform reduction in thickness in a given direction. The reduction in thickness followed by an increase, as seen in two different tissue regions, indicate that the thickness non-uniformities are a result of variations in tissue morphology.

If the changes in tissue thickness are solely the result of morphology changes, the anisotropy measurement would not vary from one section to the next, in serial sections. To this end, we obtained a tissue microarray slides from the University of Illinois at Chicago, consisting of normal prostate and prostate cancer cores serially sectioned at differing thicknesses over the range of 2μm - 6μm (Fig B.2-A). A 4μm section was cut adjacent to each of the 2, 3, 5 and 6 micron sections as an internal control. Anisotropy was measured in a 32x32μm stromal region adjacent to the same gland in the serial sections of a normal and cancerous core from the microarray. The size of the stromal region corresponded to the stromal regions used in anisotropy analysis for recurrence prediction. Our results show that small variations in thickness (±1μm) do not affect anisotropy values (Fig B.2-B). Additionally, the repeatability of anisotropy measurements in the serial sections shows that thickness non-uniformities over small tissue regions are a property of tissue.

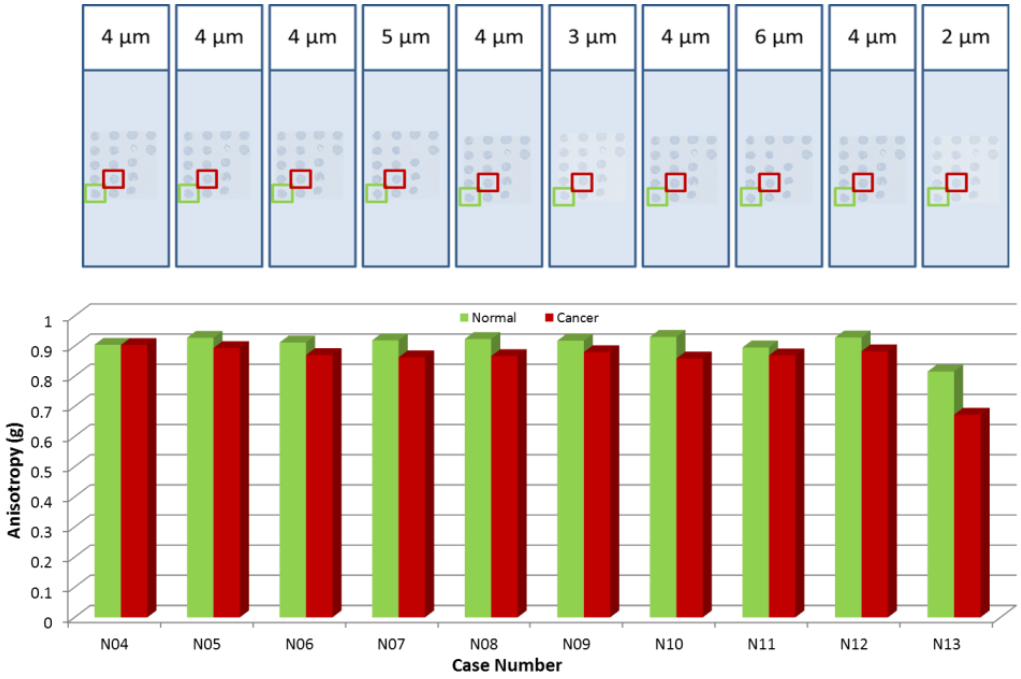

Figure B.2: Effect of Section Thickness on Anisotropy. Anisotropy was measured in a 32x32µm stromal region adjoining the same gland from a normal and cancerous core across sections of thicknesses from 2µm – 6µm. The anisotropy measurements are comparable across the different thicknesses, indicating that a local change in tissue thickness is a function of morphology.